RECLAMATION

Managing Water in the West

Report DSO-07-02

Perfectly Matched Layers for Acoustic and Elastic Waves

Dam Safety Technology Development Program

U.S. Department of the Interior
Bureau of Reclamation
Technical Service Center
Denver, Colorado

October 2008

PERFECTLY MATCHED LAYERS FOR ACOUSTIC AND ELASTIC WAVES

by

Ushnish Basu

A research report for the
Dam Safety Research Program
U.S. Department of the Interior
Bureau of Reclamation

Livermore Software Technology Corp.
Livermore, California

EXECUTIVE SUMMARY

The modelling of linear wave propagation on unbounded domains is of interest in various fields of both science and engineering. It is especially of interest in the earthquake analysis of dams because the foundation rock and impounded water may be modelled as unbounded domains undergoing wave motion generated by the motion of the dam.

One approach to the numerical solution of a wave equation on an unbounded domain uses a bounded domain surrounded by an absorbing boundary or layer that absorbs waves propagating outward from the bounded domain. A perfectly matched layer (PML) is an absorbing layer model that absorbs, almost perfectly, all waves incident upon it. This report develops the concept of a PML for elastic and acoustic waves using some of the insights obtained in the context of electromagnetics and presents PMLs for (1) a rod on elastic foundation, (2) acoustic waves in two and three dimensions, and (3) elastic waves in two and three dimensions. Furthermore, this report develops displacement-based finite-element implementations for the PMLs, both in the frequency-domain and the time-domain. In particular, an efficient finite-element implementation suitable for explicit integration is presented for the three-dimensional elastic PML, thus allowing the solution of realistic three-dimensional problems without the overhead of solving a large system of equations at each time step.

Numerical results are presented for the classical problem of an acoustic waveguide, which is representative of the reservoir behind the dam, and for the classical soil-structure interaction problems of a footing on a (i) half-space, (ii) layer on a half-space, and (iii) layer on a rigid base. These results demonstrate that PML models provide highly accurate results for a wide range of problems at a low computational cost, and thus provide a suitable way of modelling the unbounded foundation rock and impounded water in earthquake analysis of dams.

ACKNOWLEDGEMENTS

This research investigation has been funded by the U.S. Army Corps of Engineers and the U.S. Bureau of Reclamation. In particular, the doctoral research work of Dr. Ushnish Basu of developing the two-dimensional PML was funded by the Waterways Experiment Station, U.S. Army Corps of Engineers, under Contract DACW39-98-K-0038 to Prof. Anil K. Chopra at the University of California, Berkeley, and the post-doctoral research of Dr. Basu on the initial development of the three-dimensional PML was funded jointly by the U.S. Bureau of Reclamation and the U.S. Army Corps of Engineers, under Award No. W912HZ-05-P-0128 to Prof. Chopra, with project liaisons Larry Nuss at USBR and Robert Hall at the Army Corps. This financial support is gratefully acknowledged. The research on the three-dimensional PML was supported in part by the National Science Foundation through the San Diego Supercomputer Center under the Academic Associates Program and utilized the p690 nodes on the Datastar system. A major portion of the research presented in this report has been published in the following papers and reports:

1. U. Basu and A. K. Chopra. Perfectly matched layers for time-harmonic elastodynamics of unbounded domains: theory and finite-element implementation. *Computer Methods in Applied Mechanics and Engineering*, 192(11–12):1337-1375, March 2003.

2. U. Basu and A. K. Chopra. Perfectly matched layers for transient elastodynamics of unbounded domains. *International Journal for Numerical Methods in Engineering*, 59(8): 1039–1074, February 2004. Erratum: Ibid. 61(1):156–157, September 2004.

3. U. Basu. Perfectly matched layers for acoustic and elastic waves: theory, finite-element implementation and application to earthquake analysis of dam-water-foundation rock systems. Ph.D. Dissertation. University of California, Berkeley, December 2004.

4. U. Basu and A. K. Chopra. Finite-element PML for three-dimensional acoustic waves. Report No. UCB/SEMM-2005/03, University of California, Berkeley, March 2005.

5. U. Basu. Explicit finite element perfectly matched layer for transient three-dimensional elastic waves. To appear in *International Journal for Numerical Methods in Engineering*, 2008.

The author would like to thank the following people for their helpful advice and comments during the course of this work: Prof. Anil K. Chopra, Prof. Robert L. Taylor, Prof. Sanjay Govindjee, John Hallquist, Prashanth K. Vijalapura, Jerome Solberg, David Bindel, Tsuyoshi Koyama, Grant Cook, Brian Wainscott, Antar Bandyopadhyay and Prof. Fernando L. Teixeira.

TABLE OF CONTENTS

1 INTRODUCTION

The modelling of linear wave propagation on unbounded domains is of interest in various fields of both science and engineering [1, 2], ranging from simulation of earthquake ground motion [3, 4] and soil-structure interaction [5, 6], to electromagnetic waves [7], MEMS devices [8] and quantum mechanics [9]. Such modelling is especially of interest in the design of earthquake-resistant dams and in the evaluation of earthquake safety of existing dams, because the unbounded foundation rock and impounded water lead to radiation damping, which is known to be significant in the earthquake response of dams [10].

Solution of a wave equation in an unbounded domain requires the imposition of a radiation condition in any unbounded direction: waves should radiate outwards from a source — a vibrating structure, for example — toward an unbounded direction, without any spurious wave motion in the reverse direction. Irregularities in the geometry of the domain or in the physical material often compel a numerical solution of the problem, thus requiring the use of a bounded domain, along with an artificial boundary that absorbs outgoing waves, for the modelling of the unbounded domain. Accurate yet efficient absorbing boundaries are crucial for the solution of both time-harmonic and transient problems: time-harmonic problems are governed by elliptic partial differential equations, where any spurious boundedness affects the entire domain instantly, whereas absorbing boundaries for transient analysis facilitate incorporation of non-linearity within the bounded domain.

Typical absorbing boundaries belong to one of two broad categories: 1) rigorous, non-local boundaries [11–14], typically formulated for time-harmonic analysis or 2) approximate, local boundaries [15–17], typically formulated for transient analysis. The various existing absorbing boundaries, local or not, are not without drawbacks.

The rigorous boundaries, such as boundary elements [11] and DtN maps [12, 13] are highly accurate and thus may be used with a small bounded domain. However, the low computational cost due to the small size of the domain may be negated by the expense due to not only the non-local nature of such boundaries but also the computation of the boundary terms. Moreover, rigorous boundaries are typically based on time-harmonic semi-analytical solutions, and therefore are often restricted to linear systems with homogeneous, isotropic material and simple geometries; corresponding time-domain formulations [18–20] may be computationally expensive and are also subjected to the same restrictions on material and geometry.

Classical approximate absorbing boundaries [15–17, 21], although local and cheaply computed, may require large bounded domains for satisfactory accuracy, since typically they absorb incident waves well only over a small range of angles-of-incidence. Moreover, high-order approximate boundaries require the use of special finite elements [22–27] for proper implementation. Various absorbing layer models [28–30] have also been proposed as alternatives to absorbing boundaries;

however, obtaining satisfactory performance from such models may require careful formulation and implementation, since the change in material properties from the elastic medium to the absorbing layer causes reflection of incident waves [31]. The superposition boundary [32] is cumbersome and expensive to implement, and infinite elements [33,34] typically require problem-dependent assumptions on the wave motion.

The difficulty in obtaining a sufficiently accurate, yet not-too-expensive model of the unbounded domain directly in the time domain has led to the development of transient analysis methods that use frequency-domain analysis as an intermediate step. One such method uses hybrid frequency–time-domain analysis [6,35], iterating between the frequency and time domains in order to account for nonlinearity in the bounded domain; this computationally demanding method requires careful implementation to ensure stability. Another approach replaces the nonlinear system by an equivalent linear system [36] whose stiffness and damping values are compatible with the effective strain amplitudes in the system. A third approach [37–39] approximates the frequency-domain DtN map of a system by a rational function and uses this approximation to obtain a time-domain system that is temporally local. Although this approach is conceptually attractive, computation of an accurate rational-function approximation may be expensive.

A perfectly matched layer (PML) is an absorbing layer model for linear wave equations that absorbs, almost perfectly, propagating waves of all non-tangential angles-of-incidence and of all non-zero frequencies. The concept of a PML was first introduced by Bérenger [40] in the context of electromagnetic waves. More significantly, Chew and Weedon [41] showed — almost immediately — that the Bérenger PML equations arise from a complex-valued coordinate stretching in the electromagnetic wave equations. Since the introduction of these seminal ideas, extensive research has been conducted on various aspects of PMLs for electromagnetic waves; this is mentioned without references: a review of electromagnetics PMLs is beyond the scope of this work. PMLs have been formulated for other linear wave equations too: the scalar wave equation or the Helmholtz equation [42–44], the linearised Euler equations [45], the wave equation for poroelastic media [46], and, as discussed below, to the elastodynamic wave equation.

To the author's knowledge, the idea that PMLs could be formulated for the elastodynamic wave equation was first introduced by Chew and Liu [47]: they used complex-valued coordinate stretching to obtain the equations governing the PML and presented a proof of the absorptive property of the PML. Furthermore, they presented a finite-difference-time-domain (FDTD) formulation obtained through field splitting or an nonphysical additive decomposition of the velocity and stress fields. Contemporaneously, Hastings et al. [48] applied Bérenger's original split-field formulation of the electromagnetics PML directly to the P- and S-wave potentials and obtained a two-dimensional FDTD scheme for implementing the resultant formulation. Liu [49] later applied the coordinate stretching idea to the velocity-stress formulation of the elastodynamic equation to obtain split-field PMLs for time-dependent elastic waves in cylindrical and spherical coordinates. Zhang and Ballmann [50] and Collino and Tsogka [51] have also obtained split-field, time-domain PMLs for the velocity-stress formulation and presented FDTD implementations. The latter have also implemented the PML using a two-dimensional mixed finite-element scheme [52] in which the degrees-of-freedom of each element are the velocity, the shear stress, and split-field components of

the axial stresses. More recently, Festa and Nielsen [53] have extended the FDTD implementation of Collino and Tsogka to three-dimensional problems and numerically analysed the Rayleigh-wave absorption capacity of PMLs, Komatitsch and Tromp [54] have presented a PML formulation using field-splitting of the displacements, and implemented it using spectral elements, Marcinkovich and Olsen [55] have presented an implementation in a three-dimensional fourth-order velocity-stress finite-difference scheme, and Ma and Liu [56] have explored the use of PML with single-point integration and hourglass control, among others [57–62].

A PML must be formulated with certain practical considerations in mind if it is to be widely adopted and used outside of in-house research software. Because of its intrinsic ability to model arbitrary and complex geometries and materials with relative ease, the finite-element method [63–65] has become the method of choice for modelling solid mechanics and elasticity problems, and existing software for finite-element modelling, analysis and visualisation are predominantly geared toward the displacement-based finite-element method. It is therefore pragmatic to formulate the PML in terms of displacement-based finite elements, because the object of interest in the analysis is not the PML itself, but what it bounds, which may be a domain with non-linear material and complex geometry [3, 6]; the PML merely serves to model the rest of the world [1]. Furthermore, it is imperative that the PML allow explicit time-integration, because it is impractical to solve large systems of equations — from e.g., three-dimensional problems — at each time-step. Most existing formulations of PMLs for transient elastic waves [47–59, 61, 62] use explicit time-integration, but either with a finite-difference scheme, or with a finite-difference-motivated split-field formulation in a finite-element setting, with the split fields visible outside of the element.

The objective of this report is to develop the concept of PML for elastodynamics in a way that ultimately allows development of displacement-based finite-element PML with explicit integration for three-dimensional elastic waves — thus allowing a transient finite-element model of the unbounded foundation rock beneath a dam — and a similar PML for acoustic waves, thus allowing a model for the unbounded reservoir behind it. To this end, the concept of a PML is developed for elastodynamics using some of the insights obtained in the context of electromagnetics [66–68]. The PML concept is first illustrated through the one-dimensional example of a rod on elastic foundation in Chapter 2, and then extended to acoustic waves in Chapters 3 and 4 for both two- and three-dimensional problems, and to elastic waves in Chapters 5 and 6. The PML formulations are numerically validated by modelling relevant classical problems. The acoustic PML models are validated for an acoustic waveguide, an idealisation of the impounded water in the reservoir, and the elastic PML models are validated for the classical soil-structure interaction problems of a footing on a (i) half-space, (ii) layer on a half-space, and (iii) layer on a rigid base.

2 A ONE-DIMENSIONAL SYSTEM

2.1 Introduction

The ideas central to the concept of a perfectly matched layer are introduced and explored in this chapter. These ideas are explicated in the context of the one-dimensional system of a semi-infinite rod on elastic foundation, chosen because it allows both propagating and evanescent waves. In addition to presenting an analytical exploration of a perfectly matched layer, this chapter also demonstrates the finite-element implementation of the PML equations, for both time-harmonic and transient analysis.

2.2 Semi-infinite rod on elastic foundation

Consider a semi-infinite rod on elastic foundation (Fig. 2.1), not subjected to any body forces, but subjected to an imposed displacement $u_0(t)$ at the left end ($x = 0$), and a radiation condition for $x \to \infty$. This excitation causes displacements $u(x,t)$, which are governed by the following equations:

$$\frac{\mathrm{d}\sigma}{\mathrm{d}x} - \frac{k_g}{A}u = \rho\ddot{u} \tag{2.1a}$$

$$\sigma = E\,\varepsilon \tag{2.1b}$$

$$\varepsilon = \frac{\mathrm{d}u}{\mathrm{d}x} \tag{2.1c}$$

where σ and ε are the axial stress and infinitesimal strain in the rod, E is the Young's modulus of the rod, A its cross-sectional area, ρ its mass density, and k_g the static stiffness per unit length of the foundation.

If the imposed displacement is time-harmonic of the form $u_0(t) = \bar{u}_0 \exp(\mathrm{i}\omega t)$, with ω the frequency of excitation, then the displacements u are also time-harmonic of the form $u(x,t) = \bar{u}(x)\exp(\mathrm{i}\omega t)$, with $\bar{u}(x)$ governed by the following equations:

$$\frac{\mathrm{d}\bar{\sigma}}{\mathrm{d}x} - \frac{k_g}{A}\bar{u} = -\omega^2\rho\bar{u} \tag{2.2a}$$

$$\bar{\sigma} = E\,\bar{\varepsilon} \tag{2.2b}$$

$$\bar{\varepsilon} = \frac{\mathrm{d}\bar{u}}{\mathrm{d}x} \tag{2.2c}$$

where $\bar{\sigma}$ and $\bar{\varepsilon}$ are the harmonic amplitudes of σ and ε, respectively.

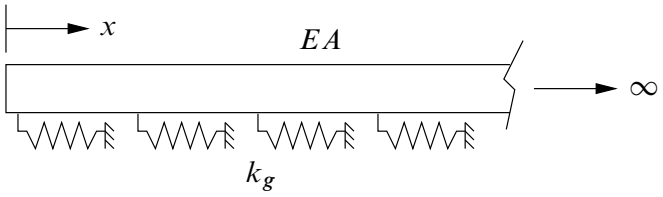

Figure 2.1. Homogeneous (visco-)elastic semi-infinite rod on elastic foundation.

The frequency-response of this system can be expressed in terms of a dimensionless frequency $a_0 = \omega r_0/c_l$, where $r_0 = \sqrt{EA/k_g}$ is a characteristic length quantity and $c_l = \sqrt{E/\rho}$ is the wave velocity in the rod. For $a_0 < 1$, Eq. (2.2) admits rightward- and leftward-evanescent-wave solutions of the form

$$\bar{u}(x) = \exp\left[-\sqrt{1-a_0^2}\frac{x}{r_0}\right] \quad \text{and} \quad \bar{u}(x) = \exp\left[+\sqrt{1-a_0^2}\frac{x}{r_0}\right] \tag{2.3}$$

and admits rightward- and leftward-propagating-wave solutions of the form

$$\bar{u}(x) = \exp\left[-\mathrm{i}\sqrt{a_0^2-1}\frac{x}{r_0}\right] \quad \text{and} \quad \bar{u}(x) = \exp\left[+\mathrm{i}\sqrt{a_0^2-1}\frac{x}{r_0}\right] \tag{2.4}$$

for $a_0 > 1$, with $a_0 = 1$ the cut-off frequency of the system; the radiation condition allows only the rightward modes in the system. The dynamic stiffness at $x = 0$, which is the axial force $-\bar{\sigma}A$ required in the positive x-direction at $x = 0$ to maintain $\bar{u}_0 = 1$, can be obtained using Eqs. (2.2b), (2.2c) and Eqs. (2.3a), (2.4a) as

$$S^{\infty}(a_0) = \sqrt{1-a_0^2} \tag{2.5}$$

normalised with respect to $K^{\infty} = \sqrt{EAk_g}$, the static stiffness coefficient of the system.

The motion of a visco-elastic system, where material damping is introduced through the correspondence principle [69], is also described by the above equations, but with complex-valued material moduli $E^* = E(1+2\mathrm{i}\zeta)$ and $k_g^* = k_g(1+2\mathrm{i}\zeta)$ in place of the real moduli E and k_g, ζ being the hysteretic damping ratio. The introduction of complex moduli results in a complex-valued wave speed $c_l^* = c_l\sqrt{1+2\mathrm{i}\zeta}$ and complex-valued dimensionless frequency $a_0^* = a_0/\sqrt{1+2\mathrm{i}\zeta}$.

The solutions for the displacement and dynamic stiffness of the semi-infinite rod are obtained by analytically solving Eq. (2.2) on the unbounded domain $[0,\infty)$ using appropriate boundary conditions. Numerical solution of this unbounded domain problem requires the solution of Eq. (2.2) on a bounded domain augmented by an artificial absorbing boundary or layer; a PML is an absorbing layer model that can be used towards this purpose.

2.3 Perfectly matched medium

Consider a system of equations of the same form as Eq. (2.2), but with x replaced by a stretched coordinate $\tilde{x}$, defined as [66]

$$\tilde{x} := \int_0^x \lambda(s)\,\mathrm{d}s \tag{2.6}$$

where λ is a nowhere-zero, continuous, complex-valued coordinate *stretching function.* By the continuity of λ,

$$\frac{\mathrm{d}\tilde{x}}{\mathrm{d}x} = \lambda(x) \tag{2.7}$$

which formally implies

$$\frac{\mathrm{d}}{\mathrm{d}\tilde{x}} = \frac{1}{\lambda(x)}\frac{\mathrm{d}}{\mathrm{d}x} \tag{2.8}$$

Thus this aforementioned system of equations can be defined as

$$\frac{1}{\lambda(x)}\frac{\mathrm{d}\bar{\sigma}}{\mathrm{d}x} - \frac{k_g}{A}\bar{u} = -\omega^2\rho\bar{u} \tag{2.9a}$$

$$\bar{\sigma} = E\,\bar{\varepsilon} \tag{2.9b}$$

$$\bar{\varepsilon} = \frac{1}{\lambda(x)}\frac{\mathrm{d}\bar{u}}{\mathrm{d}x} \tag{2.9c}$$

as a modification of Eq. (2.2), where the constitutive relation, Eq. (2.9b), remains the same as for the elastic medium. A perfectly matched medium (PMM) for a rod on elastic foundation is defined to be a medium where the field variable $\bar{u}$ is governed by Eq. (2.9). The (visco-)elastic medium is a special PMM, where $\lambda(x) \equiv 1$.

Equation (2.9) is only motivated by, but defined independently of Eq. (2.8); using the latter to derive the PMM equations from Eq. (2.2) would involve issues of complex differentiability, all of which are neatly avoided by the independent definition of the PMM. The assumption of continuity on λ could presumably be dropped, by considering one-sided derivatives, or possibly even weak derivatives, in Eq. (2.7); such technical issues are avoided by this convenient assumption. Note that the assumption of a continuous λ is not restrictive in the least: the stretching function is specified *a priori*, and is not a physical quantity that is intrinsically discontinuous.

As is to be expected from the coordinate-stretching motivation, Eq. (2.9) admits solutions similar in form to those in Eqs. (2.3) and (2.4) admitted by the elastic medium, but with x replaced by $\tilde{x}$. Evanescent-wave-type solutions are of the form

$$\bar{u}(x) = \exp\left[-\sqrt{1-a_0^2}\frac{\tilde{x}}{r_0}\right] \quad \text{and} \quad \bar{u}(x) = \exp\left[+\sqrt{1-a_0^2}\frac{\tilde{x}}{r_0}\right] \tag{2.10}$$

for $a_0 < 1$, and propagating-wave-type solutions are of the form

$$\bar{u}(x) = \exp\left[-\mathrm{i}\sqrt{a_0^2-1}\frac{\tilde{x}}{r_0}\right] \quad \text{and} \quad \bar{u}(x) = \exp\left[+\mathrm{i}\sqrt{a_0^2-1}\frac{\tilde{x}}{r_0}\right] \tag{2.11}$$

for $a_0 > 1$; that these are solutions of Eq. (2.9) can be shown by utilising the continuity of λ through Eq. (2.7).

A special property of these PMMs is that if two PMMs with different λ are placed adjacent to each other, with the functions λ such that they match at the interface of the two media, then a wave-type motion will pass through the interface without generating any reflected wave; this is the *perfect matching* property of the PMM. Without loss of generality, consider two PMMs: one is defined on $(-\infty, 0)$ with $\lambda(x) := \lambda^{\mathrm{lt}}(x)$, and the other on $[0, \infty)$ with $\lambda(x) := \lambda^{\mathrm{rt}}(x)$, with the stretching functions such that $\lambda^{\mathrm{lt}}(0) = \lambda^{\mathrm{rt}}(0)$. These two PMMs can be considered as only one PMM but with a continuous λ defined piecewise on $(-\infty, 0)$ and $[0, \infty)$; thus, there is no interface, precluding the possibility of the generation of any reflected wave. The perfect matching property holds for both solutions in Eq. (2.11) as well as for those in Eq. (2.10), i.e., it is independent of the type of wave, of the direction of propagation, and of the frequency a_0.

Another special property of the PMMs is that for suitable choices of λ, the solutions in the PMM take the form of the corresponding elastic-medium solution but with an imposed spatial attenuation. Consider, for $a_0 > 1$, λ defined in terms of a real-valued, continuous function f as

$$\lambda(x) := 1 - \mathrm{i}\frac{f(x/r_0)}{\sqrt{a_0^2 - 1}} \tag{2.12}$$

Then

$$\frac{\tilde{x}}{r_0} = \frac{x}{r_0} - \mathrm{i}\frac{F(x/r_0)}{\sqrt{a_0^2 - 1}} \tag{2.13}$$

where

$$F(x/r_0) := \int_0^{x/r_0} f(\xi)\,\mathrm{d}\xi \tag{2.14}$$

On substituting for $\tilde{x}$ from Eq. (2.13) into Eq. (2.11a), the solution is obtained as

$$\bar{u}(x) = \exp\left[-F(x/r_0)\right] \exp\left[-\mathrm{i}\sqrt{a_0^2 - 1}\frac{x}{r_0}\right] \tag{2.15}$$

Thus, if $F(x/r_0) > 0$, then $\bar{u}(x)$ is a rightward propagating wave that is attenuated in that direction, with the attenuation independent of the frequency due to the choice of $\lambda(x)$; the function f is termed the *attenuation function.* Furthermore, for $a_0 < 1$, consider λ defined as

$$\lambda(x) := 1 + \frac{f(x/r_0)}{\sqrt{1 - a_0^2}} \tag{2.16}$$

then Eq. (2.10a) is transformed to

$$\bar{u}(x) = \exp\left[-F(x/r_0)\right] \exp\left[-\sqrt{1 - a_0^2}\frac{x}{r_0}\right] \tag{2.17}$$

i.e., an evanescent wave with additional attenuation.

The above choices for the stretching function are merely illustrative choices that exploit prior knowledge of the solution. A more realistic choice for λ would be in terms of two non-negative attenuation functions f^{e} and f^{p}, as

$$\lambda(x) := \left[1 + \frac{f^{\mathrm{e}}(x/r_0)}{a_0}\right] - \mathrm{i}\frac{f^{\mathrm{p}}(x/r_0)}{a_0} \tag{2.18}$$

This function does not assume knowledge of the frequency equation of the system, nor does *a priori* distinguish between evanescent and propagating waves. This choice for λ imposes a frequency-dependent attenuation and a phase change on the rightward propagating wave: Eq. (2.11a) is transformed into

$$\bar{u}(x) = \exp\left[-F^{\mathrm{p}}(x/r_0)\sqrt{1-\frac{1}{a_0^2}}\right]\exp\left[-\mathrm{i}\sqrt{a_0^2-1}\left(\frac{x}{r_0}+\frac{F^{\mathrm{e}}(x/r_0)}{a_0}\right)\right] \tag{2.19}$$

where F^{e} and F^{p} are appropriately-defined integrals of f^{e} and f^{p}, respectively. Using Eq. (2.18) imposes an attenuation and a harmonic mode on evanescent waves: Eq. (2.10a) transforms to

$$\bar{u}(x) = \exp\left[-F^{\mathrm{e}}(x/r_0)\sqrt{\frac{1}{a_0^2}-1}\right]\exp\left[\mathrm{i}F^{\mathrm{p}}(x/r_0)\sqrt{\frac{1}{a_0^2}-1}\right]\exp\left[-\sqrt{1-a_0^2}\frac{x}{r_0}\right] \tag{2.20}$$

Thus, f^{e} imposes an attenuation on evanescent waves and f^{p} on propagating waves.

2.4 Perfectly matched layer

These special properties of the PMM can be used to define an absorbing layer adjacent to a bounded domain such that the layer and the domain together model the unbounded domain.

Consider the system shown in Fig. 2.2a: Ω_{BD} ($:= [0, L]$) is the bounded domain governed by Eq. (2.2), and $\Omega^{\infty}_{\mathrm{PM}}$ ($:= (L, \infty)$) is the unbounded PMM, governed by Eq. (2.9). The stretch λ is taken to be of the form in Eq. (2.12) for $a_0 > 1$ and Eq. (2.16) for $a_0 < 1$, with f chosen such that $f(L/r_0) = 0$. Alternatively, λ can be chosen as in Eq. (2.18) for all a_0, with the attenuation functions such that $f^{\mathrm{e}}(L/r_0) = f^{\mathrm{p}}(L/r_0) = 0$. Since the medium in Ω_{BD} is a special PMM, with $\lambda(x) \equiv 1$, and since the admissible choices of attenuation functions impose that the functions λ for the two domains are matched at the interface, all waves propagating outwards from Ω_{BD} are completely absorbed into and then attenuated in $\Omega^{\infty}_{\mathrm{PM}}$. Thus, the displacements of this system in Ω_{BD} are exactly the same as the displacements of the semi-infinite rod in Ω_{BD}.

If the waves are attenuated enough in a finite distance, $\Omega^{\infty}_{\mathrm{PM}}$ can be terminated with a fixed boundary condition at that distance without any significant reflection of the waves. Shown in Fig. 2.2b, this bounded PMM Ω_{PM} ($:= (L, L + L_P]$) is termed the perfectly matched layer (PML). If the wave reflection from the fixed boundary is not significant, the displacements of the entire bounded system Ω ($:= \Omega_{\mathrm{BD}} \cup \Omega_{\mathrm{PM}}$) in Ω_{BD} should be almost the same as the displacements of the semi-infinite rod in Ω_{BD}.

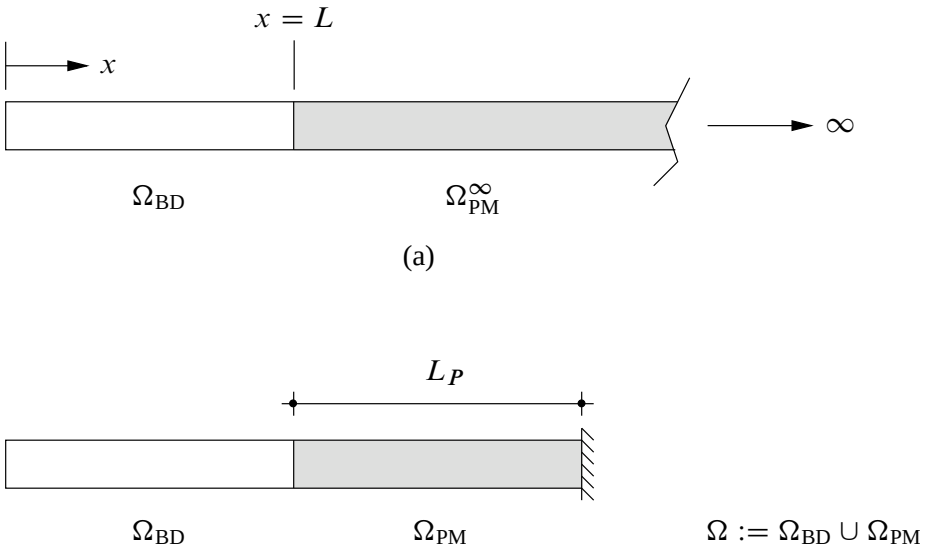

Figure 2.2. (a) Perfectly matched medium; (b) perfectly matched layer, adjacent to the bounded domain for the semi-infinite rod on elastic foundation.

2.5 Effect of fixed-end termination of the PML

The effect of domain termination in the PMM is studied analytically, first by calculating the amplitude of waves reflected back from the fixed boundary and then by investigating the effects of L, L_P and f on the (normalised) dynamic stiffness $S(a_0)$ of Ω at $x = 0$.

The reflected-wave amplitude is calculated by considering a PMM defined on $[0, L_P]$ with an imposed displacement $\bar{u}(L_P) = 0$. The stretch is chosen as in Eq. (2.12) for $a_0 > 1$ and as in Eq. (2.16) for $a_0 < 1$. A rightward propagating wave ($a_0 > 1$) with an unit amplitude as it enters the PML, along with a wave reflected back from the fixed boundary, can be represented as

$$\bar{u}(x) = \exp\left[-\mathrm{i}\sqrt{a_0^2 - 1}\frac{\tilde{x}}{r_0}\right] + R\exp\left[+\mathrm{i}\sqrt{a_0^2 - 1}\frac{\tilde{x}}{r_0}\right] \tag{2.21}$$

Imposing $\bar{u}(L_P) = 0$ gives

$$|R| = \exp\left[-2F(L_P/r_0)\right] \tag{2.22}$$

which is the amplitude of the reflected wave as it exits the PML. A similar calculation for evanescent waves using Eq. (2.16) shows that $|R|$ in Eq. (2.22) is the additional attenuation imposed by the PML on the reflected evanescent wave. This reflection coefficient $|R|$ due to the PML is controlled by the choice of the parameters f and L_P/r_0, independently of the size of the bounded domain to which the PML is adjacent. This suggests that if displacement and stress quantities near $x = 0$ for the semi-infinite elastic medium are the quantities of interest in the analysis, the bounded domain may be restricted to the region of interest, thus lowering the computational cost, if the parameters of the PML are chosen appropriately.

A choice of λ as in Eq. (2.18) leads to

$$|R| = \exp\left[-2F^{\mathrm{p}}(L_P/r_0)\sqrt{1-\frac{1}{a_0^2}}\right] \tag{2.23}$$

for $a_0 > 1$, and

$$|R| = \exp\left[-2F^{\mathrm{e}}(L_P/r_0)\sqrt{\frac{1}{a_0^2}-1}\right]\exp\left[-2\sqrt{1-a_0^2}\frac{L_P}{r_0}\right] \tag{2.24}$$

for $a_0 < 1$; an additional attenuation is imposed upon evanescent waves.

The dynamic stiffness of Ω at $x = 0$ is calculated as follows: (1) assume a solution of the form

$$\bar{u}(x) = B_1 \exp\left[-\sqrt{1-a_0^2}\frac{\tilde{x}}{r_0}\right] + B_2 \exp\left[+\sqrt{1-a_0^2}\frac{\tilde{x}}{r_0}\right] \tag{2.25}$$

in terms of constants B_1 and B_2, with imaginary square roots for $a_0 > 1$, and λ in $\tilde{x}$ defined as

$$\lambda(x) \equiv 1 \qquad \text{for } x \in [0, L] \tag{2.26a}$$

and, following Eqs. (2.16) and (2.12), in terms of a non-negative attenuation function f as

$$\lambda(x) = \begin{cases} 1 + f((x-L)/r_0)/\sqrt{1-a_0^2} & \text{if } a_0 < 1 \\ 1 - \mathrm{i}\, f((x-L)/r_0)/\sqrt{a_0^2-1} & \text{if } a_0 > 1 \end{cases} \qquad \text{for } x \in (L, L+L_P] \tag{2.26b}$$

(2) impose boundary conditions $\bar{u}(0) = 1$ and $\bar{u}(L + L_P) = 0$ to calculate B_1 and B_2, and (3) compute the dynamic stiffness as $-(\bar{\sigma}A)|_{x=0}$ using Eqs. (2.9b) and (2.9c). The dimensionless dynamic stiffness of Ω is thus obtained as

$$S(a_0) = S^{\infty}(a_0)\,\frac{1 + |R|\exp\left[-2\sqrt{1-a_0^2}(L+L_P)/r_0\right]}{1 - |R|\exp\left[-2\sqrt{1-a_0^2}(L+L_P)/r_0\right]} \tag{2.27}$$

with $S^{\infty}(a_0)$ given by Eq. (2.5), $|R|$ given by Eq. (2.22). Here $S(a_0) \to S^{\infty}(a_0)$ as $|R| \to 0$, i.e., the dynamic stiffness of the entire bounded domain is a good approximation to that of the unbounded domain if the reflection coefficient is suitably small.

If λ is chosen as

$$\lambda(x) = \left[1 + \frac{f^{\mathrm{e}}((x-L)/r_0)}{a_0}\right] - \mathrm{i}\frac{f^{\mathrm{p}}((x-L)/r_0)}{a_0} \tag{2.28}$$

in $(L, L+L_p]$, following Eq. (2.18), then the dynamic stiffness for all a_0 is still given by Eq. (2.27), but with

$$|R| = \exp\left[-2F^{\mathrm{e}}(L_P/r_0)\sqrt{\frac{1}{a_0^2}-1}\right]\exp\left[2\mathrm{i}F^{\mathrm{p}}(L_P/r_0)\sqrt{\frac{1}{a_0^2}-1}\right]$$

Thus, the accuracy of the bounded-domain approximation is controllable through f^{e} for evanescent waves and through f^{p} for propagating waves.

2.6 Effect of PML parameters on accuracy of results

Equation (2.27), with $|R|$ given by Eq. (2.22), is used to investigate the effect of the PML parameters L_P/r_0 and f on the dynamic stiffness $S(a_0)$, represented in terms of frequency-dependent stiffness, $k(a_0)$, and damping, $c(a_0)$, coefficients given by the relation

$$S(a_0) = k(a_0) + \mathrm{i}a_0 c(a_0) \tag{2.29}$$

This approximation to the stiffness of the unbounded medium is compared against the exact stiffness $S^{\infty}(a_0)$, also decomposed into stiffness and damping coefficients.

To facilitate a meaningful discussion of the effects of these parameters, the attenuation function is chosen to be of the form

$$f(x/r_0) := f_0 \left(\frac{x/r_0}{L_P/r_0} \right)^m \tag{2.30}$$

which gives

$$F(L_P/r_0) = \frac{f_0(L_P/r_0)}{m+1} \tag{2.31}$$

Thus the reflection coefficient $|R|$ in Eq. (2.22) depends on the maximum value of the attenuation function, f_0 [$= f(L_P/r_0)$], the depth of the PML, L_P/r_0, and the degree of the polynomial attenuation function, m. Equation (2.31) suggests that the accuracy will be related directly to f_0 and to L_P/r_0, but inversely to m.

It is demonstrated that it is the depth L_P/r_0 of the PML that is significant, rather than the size L/r_0 of the bounded domain. Figure 2.3a shows that if L_P/r_0 is not large enough, then increasing L/r_0 does not improve the accuracy of the results. However, as shown in Fig. 2.3b, for a sufficiently large PML ($L_P/r_0 = 1$), the size of the bounded domain does not affect the results: in the "eye-norm", there is no difference between either approximate result and the exact one.

Figure 2.4 shows the effect of the choice of the attenuation function on the accuracy of results. As was predicted from Eq. (2.31), increasing f_0 increases the accuracy of results, but increasing m leads to less accurate results. This suggests that the attenuation function should be chosen as a linear polynomial and that the accuracy should be controlled through f_0. An adequate value of f_0 can be established through a rudimentary trial-and-error procedure; it is not appropriate to choose a value of f_0 by choosing an adequate value of $|R|$ in e.g., Eq. (2.22), because adequacy of the value of $|R|$ is equivalent to adequacy of the value of f_0.

If the dynamic stiffness of the bounded domain is calculated for λ in the PML given by Eq. (2.28) with $f^{\mathrm{e}} = f^{\mathrm{p}} = f$, then the effects of L/r_0, L_P/r_0, f_0 and m on the dynamic stiffness is qualitatively similar to their effects for λ in the PML given by Eq. (2.26b), shown in Figs. 2.3 and 2.4; therefore, these results are not presented here. In fact, a highly accurate dynamic stiffness is still obtained by choosing the parameter values $L/r_0 = 1/2$, $L_P/r_0 = 1$, $f_0 = 10$ and $m = 1$.

Although not presented here, accurate results are also obtainable for a visco-elastic rod, for either of the choices of λ given above.

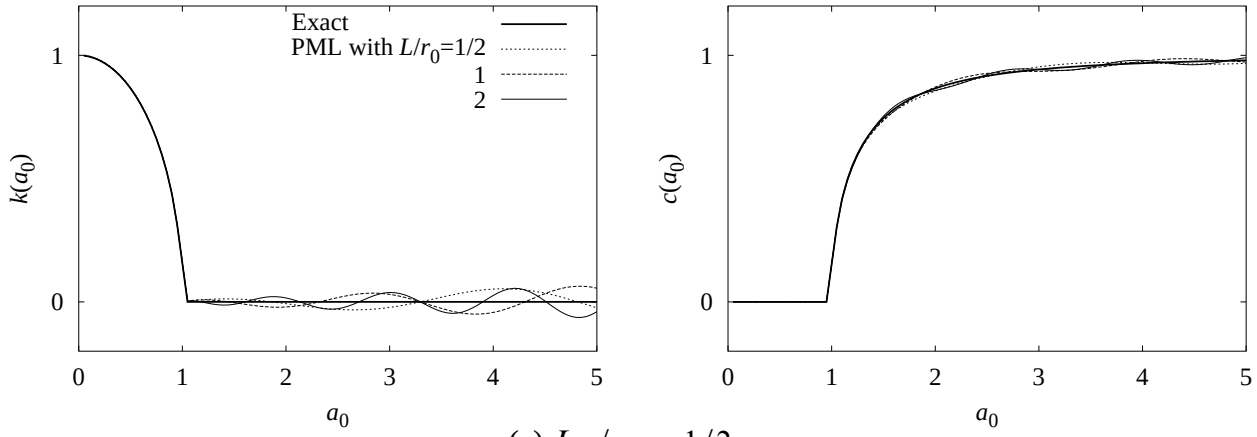

(a) $L_P/r_0 = 1/2$

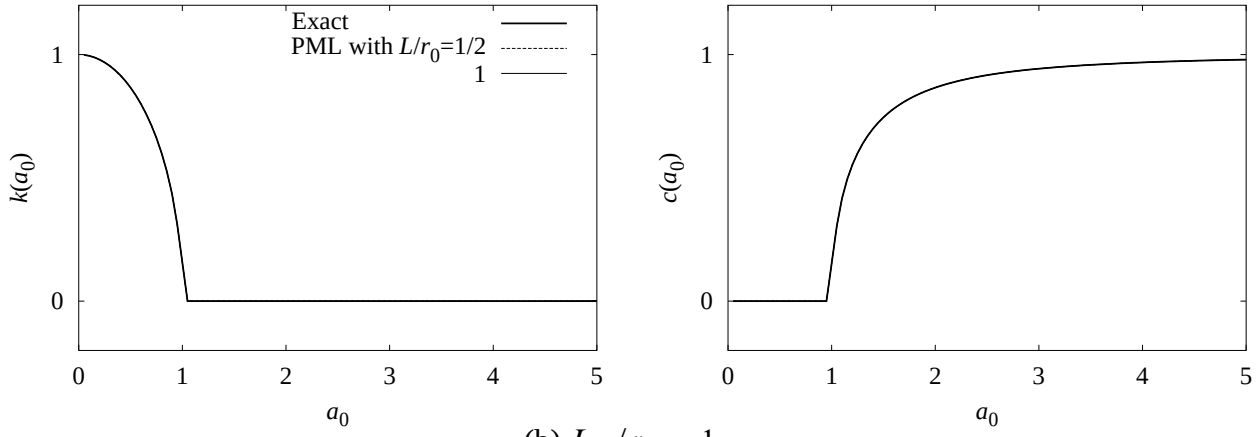

(b) $L_P/r_0 = 1$

Figure 2.3. Effect of size of bounded domain on the accuracy of dynamic stiffness of the elastic rod for two different depths of the PML; $f_0 = 10, m = 1$.

2.7 Time-harmonic finite-element implementation

The PMM is equivalently interpreted as an inhomogeneous visco-elastic medium, which is then implemented using standard displacement-based finite elements [65]. Because the displacement formulation is well known, only the salient steps of the implementation are presented.

Equation (2.9) is rewritten as follows: Equation (2.9a) is multiplied by $\lambda(x)$, and $\bar{\varepsilon}$ in Eq. (2.9c) is redefined as $\bar{\varepsilon} \leftarrow \lambda(x)\bar{\varepsilon}$ to obtain an equivalent system of equations

$$\frac{\mathrm{d}\bar{\sigma}}{\mathrm{d}x} - \frac{k_g}{A}\lambda(x)\bar{u} = -\omega^2\rho\lambda(x)\bar{u} \tag{2.32a}$$

$$\bar{\sigma} = E\frac{1}{\lambda(x)}\,\bar{\varepsilon} \tag{2.32b}$$

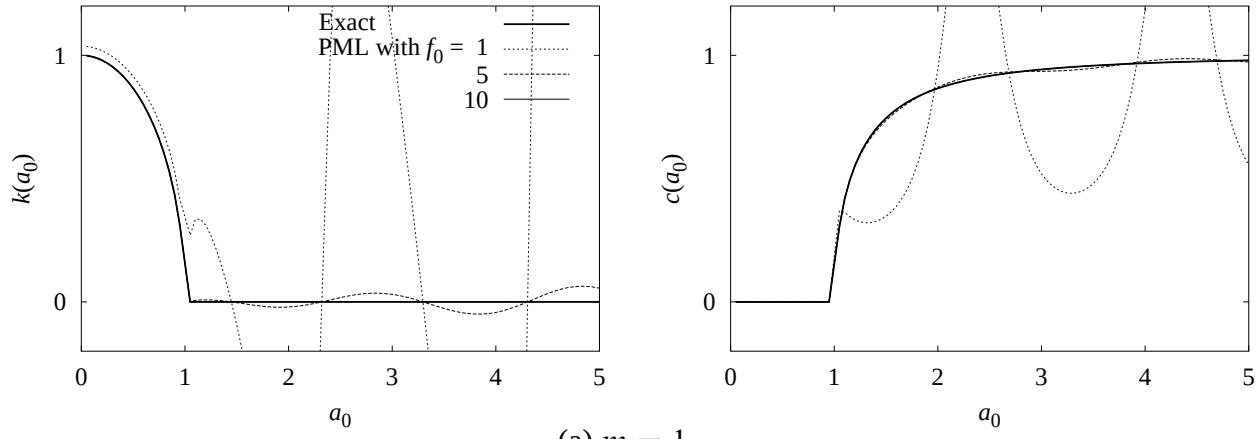

(a) $m = 1$

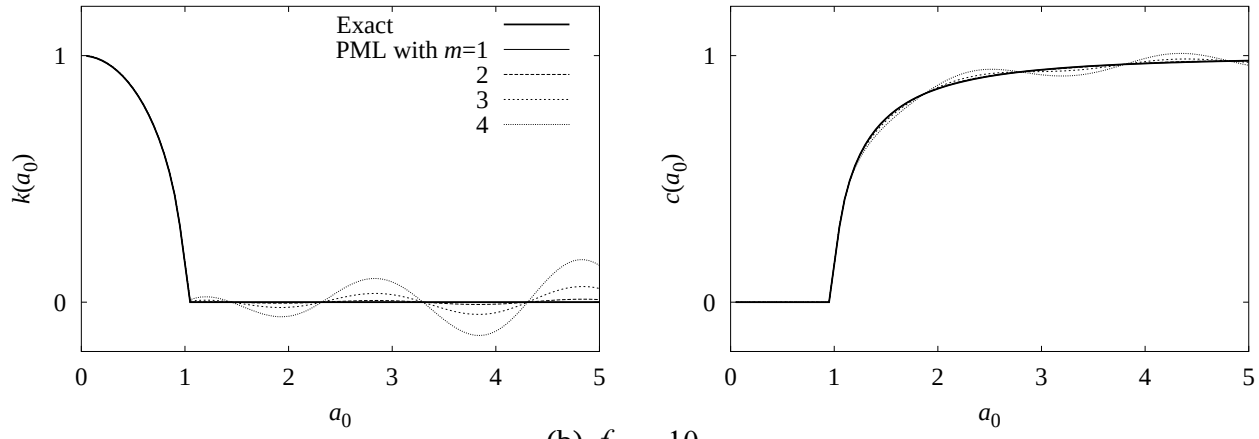

(b) $f_0 = 10$

Figure 2.4. Effect of attenuation function on the accuracy of dynamic stiffness of the elastic rod; $L/r_0 = 1/2$, $L_P/r_0 = 1$.

$$\bar{\varepsilon} = \frac{\mathrm{d}\bar{u}}{\mathrm{d}x} \tag{2.32c}$$

Here, the coordinate stretch has been transformed into a change in the material parameters; this PMM can thus be interpreted to be an inhomogeneous visco-elastic medium.

The weak form of Eq. (2.32a) is derived as follows: the equation is first multiplied by an arbitrary weighting function, w, residing in an appropriate admissible space, and then integrated over Ω using integration-by-parts to get

$$\int_\Omega \frac{\mathrm{d}w}{\mathrm{d}x}\bar{\sigma}\,\mathrm{d}\Omega + \int_\Omega \frac{k_g}{A}\lambda(x)w\bar{u}\,\mathrm{d}\Omega - \omega^2\int_\Omega \rho\lambda(x)w\bar{u}\,\mathrm{d}\Omega = (\bar{w}\bar{\sigma})|_{\partial\Omega} \tag{2.33}$$

The functions $\bar{u}$ and w are interpolated element-wise in terms of nodal quantities using $\boldsymbol{N}$, a vector of nodal shape functions, and Eqs. (2.32b) and (2.32c) are substituted into the integrals on the left

hand side of Eq. (2.33). Restricting the integrals to Ω^e, the element domain, gives the stiffness and mass matrices for a PML element:

$$\mathbf{k}_{IJ}^e = \int_{\Omega^e} \frac{\mathrm{d}N_I}{\mathrm{d}x} E \frac{1}{\lambda(x)} \frac{\mathrm{d}N_J}{\mathrm{d}x} \,\mathrm{d}\Omega + \int_{\Omega^e} \frac{k_g}{A} \lambda(x) N_I N_J \,\mathrm{d}\Omega \tag{2.34a}$$

$$\mathbf{m}_{IJ}^e = \int_{\Omega^e} \rho \lambda(x) N_I N_J \,\mathrm{d}\Omega \tag{2.34b}$$

$\mathbf{k}_{IJ}^e$ and $\mathbf{m}_{IJ}^e$ are the nodal submatrices of the entire element matrices $\mathbf{k}^e$ and $\mathbf{m}^e$, with I and J the node numbers and N_I the shape function corresponding to node I. In Eq. (2.34), λ is defined globally on the computational domain, not element-wise.

The element stiffness and mass matrices obtained above are symmetric, but are intrinsically complex-valued and frequency-dependent because of the choice for λ (Eq. (2.12) or (2.18)). Hence, the system matrices for Ω will be complex, symmetric, and sparse, the PML contributions to which will have to recomputed for each frequency.

2.8 PML for transient analysis and finite-element implementation

An alternate form of the time-harmonic PMM equations (2.9) is used to obtain the corresponding transient formulation: Eq. (2.9a) is multiplied by $\lambda(x)$ and Eq. (2.9c) by $\mathrm{i}\omega\lambda(x)$ to get

$$\frac{\mathrm{d}\bar{\sigma}}{\mathrm{d}x} - \frac{k_g}{A} \lambda(x) \bar{u} = -\omega^2 \rho \lambda(x) \bar{u} \tag{2.35a}$$

$$\bar{\sigma} = E\,\bar{\varepsilon} \tag{2.35b}$$

$$\mathrm{i}\omega\lambda(x)\,\bar{\varepsilon} = \mathrm{i}\omega\,\frac{\mathrm{d}\bar{u}}{\mathrm{d}x} \tag{2.35c}$$

Because multiplication or division by the factor $\mathrm{i}\omega$ in the frequency domain corresponds to a derivative or an integral, respectively, in the time domain, time-harmonic equations are easily transformed into corresponding equations for transient motion if the frequency-dependence of the former is only a simple dependence on this factor. Therefore, the stretching functions are chosen to be of the form

$$\lambda(x) := [1 + f^{\mathrm{e}}(x/r_0)] - \mathrm{i}\frac{f^{\mathrm{p}}(x/r_0)}{a_0} \tag{2.36}$$

Substituting this stretching function into Eq. (2.35) and applying the inverse Fourier transform to the resultant gives the time-domain equations for the PML:

$$\frac{\mathrm{d}\sigma}{\mathrm{d}x} - \frac{k_g}{A} f_{\mathrm{m}}\, u - f_{\mathrm{c}} \frac{c_l}{r_0} \frac{k_g}{A}\, U = \rho f_{\mathrm{m}}\, \ddot{u} + \rho f_{\mathrm{c}} \frac{c_l}{r_0} \dot{u} \tag{2.37a}$$

$$\sigma = E\varepsilon \tag{2.37b}$$

$$f_{\mathrm{m}} \dot{\varepsilon} + f_{\mathrm{c}} \frac{c_l}{r_0}\, \varepsilon = \frac{\mathrm{d}\dot{u}}{\mathrm{d}x} \tag{2.37c}$$

where

$$U = \int_0^t u \, \mathrm{d}\tau \tag{2.38}$$

and

$$f_{\mathrm{m}} := [1 + f^{\mathrm{e}}(x/r_0)], \qquad f_{\mathrm{c}} := f^{\mathrm{p}}(x/r_0) \tag{2.39}$$

The application of the inverse Fourier transform to obtain U assumes that $\bar{u}(\omega = 0) = 0$. The presence of the time-integral of u in the governing equations, although unconventional from the point-of-view of continuum mechanics, is not unnatural in a time-domain implementation of a PML obtained without field-splitting [70].

Equation (2.37) is implemented using a standard displacement-based finite-element approach [71]. The weak form of Eq. (2.37a) is derived by multiplying it with an arbitrary weighting function w residing in an appropriate admissible space, and then integrating over the entire computational domain Ω using integration-by-parts to obtain

$$\int_\Omega \rho f_{\mathrm{m}} w \ddot{u} \, \mathrm{d}\Omega + \int_\Omega \rho f_{\mathrm{c}} \frac{c_l}{r_0} w \dot{u} \, \mathrm{d}\Omega + \int_\Omega \frac{\mathrm{d}w}{\mathrm{d}x} \sigma \, \mathrm{d}\Omega + \int_\Omega \frac{k_g}{A} f_{\mathrm{m}} w u \, \mathrm{d}\Omega + \int_\Omega f_{\mathrm{c}} \frac{c_l}{r_0} \frac{k_g}{A} w U \, \mathrm{d}\Omega = (w\sigma)|_{\partial\Omega} \tag{2.40}$$

The weak form is first spatially discretised by interpolating u and w element-wise in terms of nodal quantities using appropriate nodal shape functions. This leads to the system of equations

$$\mathbf{m}\ddot{\boldsymbol{d}} + \mathbf{c}\dot{\boldsymbol{d}} + \mathbf{k}\boldsymbol{d} + \mathbf{K}\mathcal{D} + \boldsymbol{f}_{\mathrm{int}} = \boldsymbol{f}_{\mathrm{ext}} \tag{2.41}$$

where $\mathbf{m}$, $\mathbf{c}$, $\mathbf{k}$ and $\mathbf{K}$ are system matrices, $\boldsymbol{d}$ is a vector of nodal displacements, $\mathcal{D}$ is the time-integral of $\boldsymbol{d}$, $\boldsymbol{f}_{\mathrm{int}}$ is a vector of internal force terms, and $\boldsymbol{f}_{\mathrm{ext}}$ is a vector of external forces. These matrices and vectors are assembled from corresponding element-level matrices and vectors. In particular, the element-level constituent matrices of $\mathbf{m}$, $\mathbf{c}$, $\mathbf{k}$ and $\mathbf{K}$ are, respectively,

$$\begin{aligned} \mathbf{m}^e &= \int_{\Omega^e} \rho f_{\mathrm{m}} \boldsymbol{N}^T \boldsymbol{N} \, \mathrm{d}\Omega, \quad \mathbf{c}^e = \int_{\Omega^e} \rho f_{\mathrm{c}} \frac{c_l}{r_0} \boldsymbol{N}^T \boldsymbol{N} \, \mathrm{d}\Omega \\ \mathbf{k}^e &= \int_{\Omega^e} \frac{k_g}{A} f_{\mathrm{m}} \boldsymbol{N}^T \boldsymbol{N} \, \mathrm{d}\Omega, \quad \mathbf{K}^e = \int_{\Omega^e} f_{\mathrm{c}} \frac{c_l}{r_0} \frac{k_g}{A} \boldsymbol{N}^T \boldsymbol{N} \, \mathrm{d}\Omega \end{aligned} \tag{2.42a}$$

and the element-level internal force term is

$$\boldsymbol{f}^e = \int_{\Omega^e} \frac{\mathrm{d}\boldsymbol{N}^T}{\mathrm{d}x} \sigma \, \mathrm{d}\Omega \tag{2.42b}$$

where $\boldsymbol{N}$ is a row vector of element-level nodal shape functions The functions f^{e} and f^{p} are defined globally on the computational domain, not element-wise.

Equation (2.41) can be solved using a time-stepping algorithm such as the Newmark method [72, 73], along with Newton-Raphson iteration at each time step to enforce equilibrium. If Eq. (2.41) is

solved, say, at time station t_{n+1}, given the solution at t_n, the Newton-Raphson iteration at this time step will require a) calculation of σ_{n+1}, for calculating $\boldsymbol{f}^e_{n+1}$ [$\approx \boldsymbol{f}^e(t_{n+1})$], and b) a consistent linearisation [71, vol. 2] of $\boldsymbol{f}^e_{n+1}$ at $\boldsymbol{d}_{n+1}$ [$\approx \boldsymbol{d}^e(t_{n+1})$], where $\boldsymbol{d}^e$ is a vector of element-level nodal displacements. Therefore, Eq. (2.37c) is discretised using a backward Euler scheme on ε to obtain

$$\varepsilon_{n+1} = \left[\frac{f_{\mathrm{m}}}{\Delta t} + f_{\mathrm{c}}\frac{c_l}{r_0}\right]^{-1}\left[\frac{\mathrm{d}\boldsymbol{N}}{\mathrm{d}x}\boldsymbol{v}_{n+1} + \frac{f_{\mathrm{m}}}{\Delta t}\,\varepsilon_n\right] \tag{2.43}$$

where $\boldsymbol{v}_{n+1} \approx \dot{\boldsymbol{d}}^e(t_{n+1})$, and Δt is the time-step size. The time-discrete form of Eq. (2.37b) is

$$\sigma_{n+1} = E\varepsilon_{n+1} \tag{2.44}$$

which gives the internal force term

$$\boldsymbol{f}^e_{n+1} = \int_{\Omega^e} \frac{\mathrm{d}\boldsymbol{N}}{\mathrm{d}x}^T \sigma_{n+1}\,\mathrm{d}\Omega \tag{2.45}$$

Linearisation of Eq. (2.45) gives

$$\Delta\boldsymbol{f}^e_{n+1} = \left[\int_{\Omega^e} \frac{\mathrm{d}\boldsymbol{N}}{\mathrm{d}x}^T D\,\frac{\mathrm{d}\boldsymbol{N}}{\mathrm{d}x}\,\mathrm{d}\Omega\right]\Delta\boldsymbol{v}_{n+1} \tag{2.46}$$

where Δ is the differential operator, and

$$D = E\left[\frac{f_{\mathrm{m}}}{\Delta t} + f_{\mathrm{c}}\frac{c_l}{r_0}\right]^{-1} \tag{2.47}$$

i.e., this linearisation gives a tangent matrix

$$\check{\mathbf{c}}^e := \int_{\Omega^e} \frac{\mathrm{d}\boldsymbol{N}}{\mathrm{d}x}^T D\,\frac{\mathrm{d}\boldsymbol{N}}{\mathrm{d}x}\,\mathrm{d}\Omega \tag{2.48}$$

which may be incorporated into the effective tangent stiffness used in the time-stepping algorithm.

Furthermore, the time-integral of $\boldsymbol{d}$ is approximated as

$$\mathcal{D}_{n+1} = \mathcal{D}_n + \boldsymbol{d}_{n+1}\Delta t \tag{2.49}$$

Thus the term involving $\mathcal{D}$ in Eq. (2.41) may be linearised as

$$\Delta\left(\mathbf{K}\mathcal{D}_{n+1}\right) = \left(\mathbf{K}\Delta t\right)\Delta\boldsymbol{d}_{n+1} \tag{2.50}$$

A skeleton of the algorithm for computing the element-level effective internal force and tangent stiffness is given in Box 2.1. The system matrices $\mathbf{m}$, $\mathbf{c}$, $\mathbf{k}$ and $\mathbf{K}$ are clearly symmetric. Moreover, because all these matrices are of the same form as the system matrices for an elastic medium, the effective tangent stiffness (say, as found in the Newmark scheme) of the entire computational domain will be positive definite if f^{e} and f^{p} are positive. Furthermore, since all the system matrices, $\mathbf{m}$, $\mathbf{c}$, $\check{\mathbf{c}}$, $\mathbf{k}$ and $\mathbf{K}$ that constitute the tangent stiffness are independent of $\boldsymbol{d}$, this is effectively a linear model.

Box 2.1. Computing effective force and stiffness for rod-on-foundation PML element.

1. Compute system matrices $\mathbf{m}^e$, $\mathbf{c}^e$, $\mathbf{k}^e$ and $\mathbf{K}^e$ [Eq. (2.42a)].
2. Compute internal force $\boldsymbol{f}^e_{n+1}$ [Eq. (2.45)].
   Use ε_{n+1} [Eq. (2.43)] and σ_{n+1} [Eq. (2.44)].
3. Compute tangent matrix $\check{\mathbf{c}}^e$ [Eq. (2.48)] using D [Eq. (2.47)].
4. Compute effective internal force $\tilde{\boldsymbol{f}}^e_{n+1}$ and tangent stiffness $\tilde{\mathbf{k}}^e$:

$$\tilde{\boldsymbol{f}}^e_{n+1} = \mathbf{m}^e \boldsymbol{a}_{n+1} + \mathbf{c}^e \boldsymbol{v}_{n+1} + \mathbf{k}^e \boldsymbol{d}_{n+1} + \mathbf{K}^e \mathcal{D}_{n+1} + \boldsymbol{f}^e_{n+1}$$
$$\tilde{\mathbf{k}}^e = \alpha_{\mathrm{k}} (\mathbf{k}^e + \mathbf{K}^e \Delta t) + \alpha_{\mathrm{c}} (\mathbf{c}^e + \check{\mathbf{c}}^e) + \alpha_{\mathrm{m}} \mathbf{m}^e$$

   where $\boldsymbol{a}_{n+1} \approx \ddot{\boldsymbol{d}}^e(t_{n+1})$, and, for example,

$$\alpha_{\mathrm{k}} = 1, \quad \alpha_{\mathrm{c}} = \frac{\gamma}{\beta \Delta t}, \quad \alpha_{\mathrm{m}} = \frac{1}{\beta \Delta t^2}$$

   for the Newmark method.

Note: The tangent stiffness $\tilde{\mathbf{k}}^e$ is independent of the solution, and thus has to be computed only once. However, the internal force $\boldsymbol{f}^e_{n+1}$ has to be re-computed at each time-step because it is dependent on the solution at past times.

2.9 Numerical results

2.9.1 Time-harmonic analysis

The dynamic stiffness, $S(a_0)$, of Ω at $x = 0$, with λ as defined in Eq. (2.26), is computed using a finite-element model consisting of two-noded linear isoparametric elements. The mesh is chosen to have n_b elements in a length of r_0 in the bounded domain and n_p elements per r_0 length in the PML; n_b and n_p are parameters in the analysis.

For a sufficiently dense mesh ($n_b = n_p = 30$), the results from the finite-element model for either choice of λ in the PML (Eq. (2.26b) or Eq. (2.28)) match the corresponding analytical results for the dynamic stiffness of the bounded domain, e.g., the results presented in Figs. 2.3 and 2.4; therefore, the numerical results are not presented separately.

The effect of mesh density on the accuracy of the computed dynamic stiffness is investigated. Because the mesh should adequately capture significant spatial variations in the displacements, the mesh density in the PML should be governed by both the wavelength and the sharpness of the spatial attenuation. If the spatial attenuation is independent of the frequency, in the case of low frequencies the density should be governed by the sharpness of the attenuation and by the wavelength for high frequencies. The qualifiers “high” and “low” are characterised by the relation of the wavelength to the sharpness of the attenuation. Thus, it should suffice to choose the mesh density in the entire bounded domain to be adequate for a high enough frequency, with the density

in the PML similar to that in the bounded domain.

Figure 2.5 shows the effect of mesh density in the PML on the accuracy of the dynamic stiffness for two values of n_b. The stiffness coefficient computed with $n_p = n_b = 10$ shows a slight oscillation about the exact solution, with its amplitude increasing with frequency. Increasing n_p gives accurate results for $a_0 \lessapprox 4$; the error found in the higher frequencies is because $n_b = 10$ is not adequate in that range. The slight deterioration in accuracy of results for $n_p = 4n_b$ over those for $n_p = 2n_b$ may be due to the contrast between the densities in Ω_{BD} and Ω_{PM}. For a larger n_b ($= 20$), both $n_p = n_b$ and $n_p = 2n_b$ give highly accurate results. This demonstrates that if the mesh density in the entire bounded domain is adequate for the range of frequencies considered, the accuracy may not be significantly sensitive to the choice of n_p, provided $n_p \geqslant n_b$. In other words, this suggests that the mesh density in the PML should be chosen to be similar to that in the bounded domain, echoing conclusions reached by an earlier dispersion analysis [44].

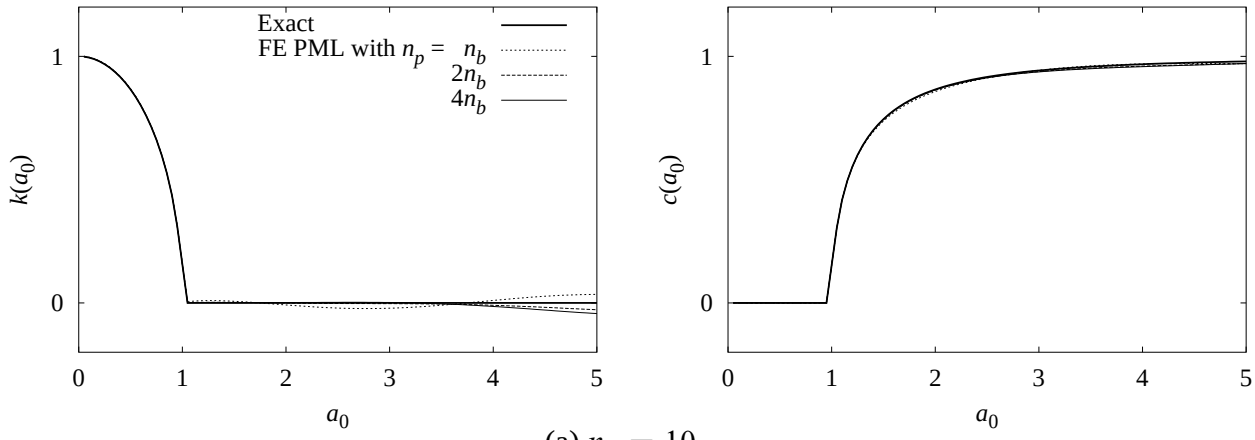

(a) $n_b = 10$

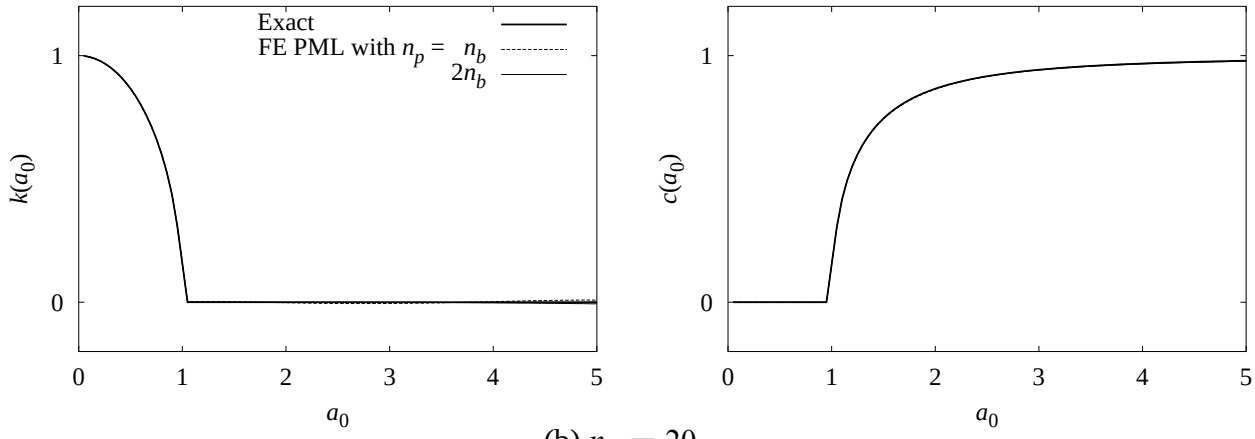

(b) $n_b = 20$

Figure 2.5. Effect of mesh density in the PML on accuracy of dynamic stiffness of elastic rod for two different mesh densities in the elastic domain; $L/r_0 = 1/2$, $L_P/r_0 = 1$, $f_0 = 10$, $m = 1$.

It is computationally advantageous to choose λ in the PML so that the attenuation does not increase too strongly with frequency, especially for higher frequencies, as is indeed the case for functions λ in both Eq. (2.26b) and Eq. (2.28). An alternate choice of

$$\lambda(x) = 1 + f^{\mathrm{e}}((x-L)/r_0) - \mathrm{i} f^{\mathrm{p}}((x-L)/r_0) \tag{2.51}$$

in the PML results in sharper attenuation for higher frequencies, thus requiring higher densities over-and-above the usual high density requirements for high frequencies. As shown in Fig. 2.6, the FE solution obtained using Eq. (2.28) is close to the exact result. The error in $c(a_0)$ for very low frequencies is due to the division of Im $\bar{S}(a_0)$ by small values of a_0. In contrast, the FE solution for Eq. (2.51) does show a slight error in $k(a_0)$ for $a_0 > 3$ which is due to inadequate mesh density in the PML. Although not presented here, this error is not found in either the corresponding analytical solution or the FE solution for a denser PML mesh ($n_b = 30$, $n_p = 60$).

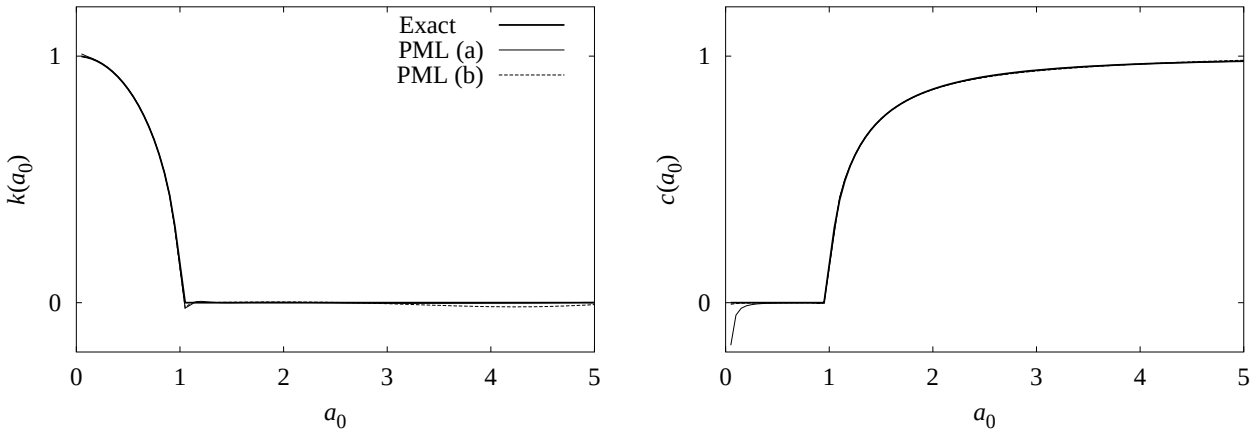

Figure 2.6. Effect of frequency dependence of stretching function on the accuracy of the finite-element solution, with λ in the PML as defined in (a) Eq. (2.28), and (b) Eq. (2.51); $n_b = n_p = 30$; $L/r_0 = 1/2$, $L_P/r_0 = 1$, $f_0 = 10$, $m = 1$.

2.9.2 Transient analysis

The effectiveness of the formulation presented in Sec. 2.8 is demonstrated by computing the response of the rod on elastic foundation to a transient excitation. The mesh chosen for the bounded-domain-PML model (Fig. 2.2b) is of the same form as chosen for time-harmonic analysis, with a sufficient mesh density ($n_b = n_p = 30$). The system is subjected to a specified displacement $u_0(t)$ at $x = 0$ in the form of a time-limited cosine wave, bookended by cosine half-cycles so that the initial displacement and velocity as well as the final displacement and velocity are zero. This imposed displacement is characterised by two parameters: the duration t_d and the dominant forcing frequency ω_f; a typical waveform and its Fourier transform are shown in Fig. 2.7, and a detailed description of the waveform is given in Appendix A. Figure 2.8 presents the reaction of the rod at $x = 0$ computed using the PML model against exact reactions computed using a convolution integral [6, pg. 344]; the PML results are virtually indistinguishable from the exact results.

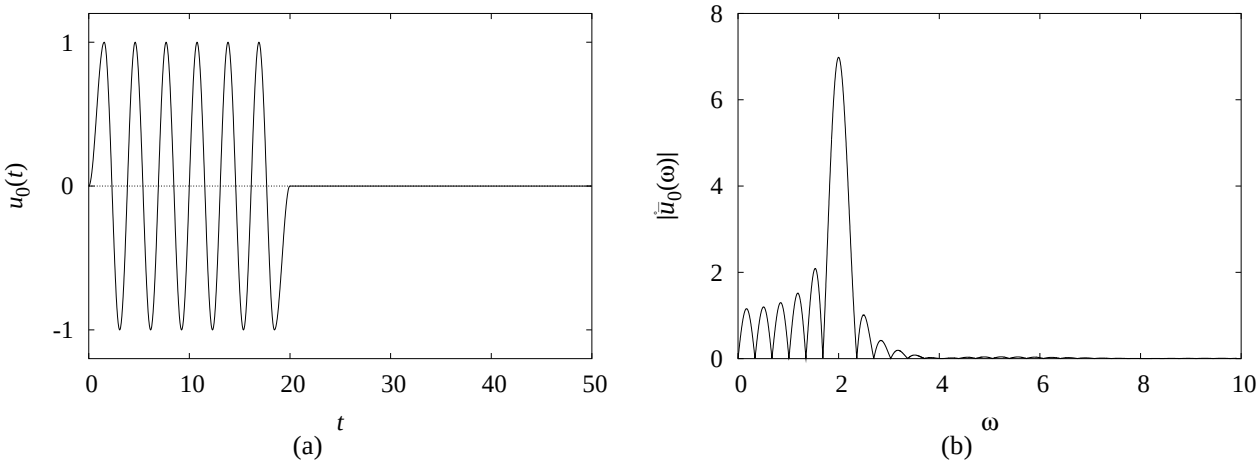

Figure 2.7. Plot of typical (a) input displacement with $t_d = 20$ and (b) amplitude of its Fourier transform, with $\omega_f = 2$.

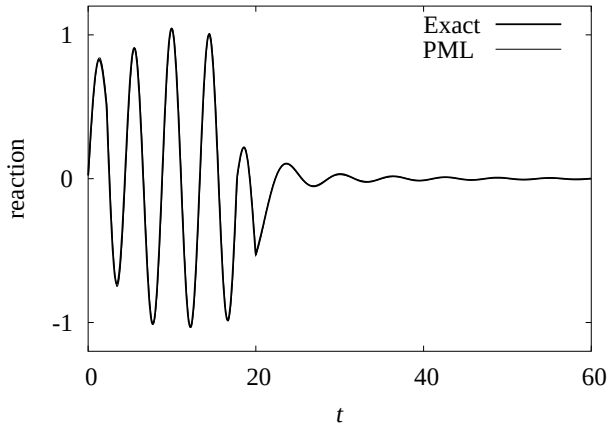

Figure 2.8. Nodal reaction of rod on elastic foundation, due to imposed nodal displacement; $L/r_0 = 1/2$, $L_P/r_0 = 1$, $f_0 = 10$, $m = 1$; $t_d = 20$, $\omega_f = 1.5$.

3 TIME-HARMONIC ACOUSTIC WAVES: THE HELMHOLTZ EQUATION

3.1 Introduction

The ideas developed for the one-dimensional problem in Chapter 2 are used analogously to develop a PML for time-harmonic acoustic waves, governed by the Helmholtz equation. It is shown that the perfect matching and attenuative properties of the PML carry over directly to higher dimensions. The PML model is implemented using finite elements by first expressing the PML equations in tensorial form.

3.2 Acoustic medium

Consider a linear, ideal, inviscid and compressible fluid, moving with zero mean velocity in the absence of body forces. The dynamic pressure p in the fluid (in excess of static pressure) is governed by the scalar wave equation, presented here in a slightly-unconventional form that will facilitate formulation of the PML equations:

$$\sum_i \frac{\partial \varphi_i}{\partial x_i} = \rho \ddot{p} \tag{3.1a}$$

$$\varphi_i = \kappa \gamma_i \tag{3.1b}$$

$$\gamma_i = \frac{\partial p}{\partial x_i} \tag{3.1c}$$

where κ is the bulk modulus of the medium and ρ its mass density, and the index i ranges over the spatial dimensions of the problem; φ_i and γ_i are merely internal variables introduced to allow the wave equation to be written as above.

If the medium is subjected to a time-harmonic excitation (through boundary conditions) then the pressure p is also time-harmonic of the form $p(\boldsymbol{x}, t) = \bar{p}(\boldsymbol{x}) \exp(\mathrm{i}\omega t)$, where ω is the frequency of excitation, with $\bar{p}(\boldsymbol{x})$ governed by the Helmholtz equation:

$$\sum_i \frac{\partial \bar{\varphi}_i}{\partial x_i} = -\omega^2 \rho \bar{p} \tag{3.2a}$$

$$\bar{\varphi}_i = \kappa \bar{\gamma}_i \tag{3.2b}$$

$$\bar{\gamma}_i = \frac{\partial \bar{p}}{\partial x_i} \tag{3.2c}$$

On an unbounded domain, Eq. (3.2) admits wave solutions of the form

$$\bar{p}(\boldsymbol{x}) = \exp\left[-\mathrm{i}k\,\boldsymbol{x}\cdot\boldsymbol{r}\right] \tag{3.3}$$

where $k = \omega/C$ is the wavenumber, with wave speed $C = \sqrt{\kappa/\rho}$, and $\boldsymbol{r}$ is a unit vector denoting the propagation direction.

3.3 Perfectly matched medium

The summation convention is abandoned in this section.

Consider a system of equations of the same form as Eq. (3.2), but with x_i replaced by stretched coordinates $\tilde{x}_i$, defined as [66]

$$\tilde{x}_i := \int_0^{x_i} \lambda_i(s)\,\mathrm{d}s \tag{3.4}$$

where λ_i are nowhere-zero, continuous, complex-valued coordinate stretching functions. This coordinate stretching formally implies

$$\frac{\partial}{\partial\tilde{x}_i} = \frac{1}{\lambda_i(x_i)}\frac{\partial}{\partial x_i} \tag{3.5}$$

thus, this system of equations can be defined as

$$\sum_i \frac{1}{\lambda_i(x_i)}\frac{\partial\bar{\varphi}_i}{\partial x_i} = -\omega^2\rho\bar{p} \tag{3.6a}$$

$$\bar{\varphi}_i = \kappa\bar{\gamma}_i \tag{3.6b}$$

$$\bar{\gamma}_i = \frac{1}{\lambda_i(x_i)}\frac{\partial\bar{p}}{\partial x_i} \tag{3.6c}$$

A PMM for time-harmonic acoustic waves is defined to be one governed by Eq. (3.6); an acoustic medium corresponds to $\lambda_i(x_i) \equiv 1$. Equation (3.6) is defined independently of, but motivated by, the definition of $\tilde{x}_i$; this is comparable to the definition of Eq. (2.9) for the one-dimensional PMM.

Given the continuity of λ_i, solutions admitted in the PMM are similar in form to that in Eq. (3.3) admitted in the acoustic medium, but with x_i replaced by $\tilde{x}_i$. Thus, Eq. (3.6) admits wave-type solutions of the form

$$\bar{p}(\boldsymbol{x}) = \exp\left[-\mathrm{i}k\,\tilde{\boldsymbol{x}}\cdot\boldsymbol{r}\right] \tag{3.7}$$

on an unbounded domain.

The perfect matching property of these PMMs is that if two PMMs with different λ_i are placed adjacent to each other, with the functions λ_i for the two media such that they match at the interface

of the media, then a propagating wave will pass through the interface without generating any reflected wave. This property is shown as follows. It is implicitly assumed in the definition of the PMM that λ_i is a function of x_i only, i.e., the coordinate stretches are uncoupled [66]. For the sake of illustration, consider the two-dimensional problem of the x_1-x_2 plane, with two PMMs defined on it: one on the left half plane ($:= \{(x_1, x_2)|x_1 < 0\}$) with $\lambda_i(x_i) := \lambda_i^{\text{lt}}(x_i)$, and another on the right half plane ($:= \{(x_1, x_2)|x_1 \geqslant 0\}$) with $\lambda_i(x_i) := \lambda_i^{\text{rt}}(x_i)$. If $\lambda_2^{\text{lt}} = \lambda_2^{\text{rt}}$, and if $\lambda_1^{\text{lt}}(0) = \lambda_1^{\text{rt}}(0)$, then the two PMMs can be considered as one PMM, wherein a continuous λ_1 is defined piecewise on the two half planes, and each λ_i is a function of x_i only; thus there is no interface to generate any reflected wave. A similar argument for three-dimensional problems leads to identical conclusions. This perfect matching property holds for any wave solution admitted by the PMM. In particular, for a wave-type solution as in Eq. (3.7), the matching is independent of the direction of propagation $\boldsymbol{r}$ and of the wavenumber k (or frequency ω).

A suitable choice of λ_i imposes an attenuation on the wave solutions to Eq. (3.6). Consider the wave-type solution in Eq. (3.7). If the functions λ_i are defined in terms of real-valued, continuous attenuation functions f_i as

$$\lambda_i(x_i) := 1 - \mathrm{i}\frac{f_i(x_i)}{k} \tag{3.8}$$

then

$$\tilde{x}_i = x_i - \mathrm{i}\frac{F_i(x_i)}{k} \tag{3.9}$$

where

$$F_i(x_i) := \int_0^{x_i} f_i(\xi)\,\mathrm{d}\xi \tag{3.10}$$

Substituting Eq. (3.9) into Eq. (3.7) gives

$$\bar{p}(\boldsymbol{x}) = \exp\left[-\sum_i F_i(x_i) r_i\right] \exp\left[-\mathrm{i}k\,\boldsymbol{x}\cdot\boldsymbol{r}\right] \tag{3.11}$$

Thus, if $F_i(x_i) > 0$ and $r_i > 0$, then $\bar{p}(\boldsymbol{x})$ is attenuated as $\exp[-F_i(x_i)r_i]$ in the x_i-direction, and the attenuation is independent of the frequency if r_i is.

3.4 Perfectly matched layer

Consider a wave of the form in Eq. (3.3) propagating in an unbounded acoustic domain, the x_1-x_2 plane, governed by Eq. (3.1). The objective of defining a PML is to simulate this wave propagation by using a corresponding bounded domain. Consider the replacement of the unbounded domain by $\Omega_{\text{BD}} \cup \Omega_{\text{PM}}^{\infty}$ as shown in Fig. 3.1a, where Ω_{BD} is a "bounded" (truncated) domain, governed by Eq. (3.1), and $\Omega_{\text{PM}}^{\infty}$ is the unbounded PMM, governed by Eq. (3.6), with λ_1 of the form in Eq. (3.8), satisfying $f_1(0) = 0$, and $\lambda_2 \equiv 1$. Because a) the medium in Ω_{BD} is a special PMM [$\lambda_i(x_i) \equiv 1$, no summation], and b) the functions λ_i for the two media are chosen to be matched at the interface, all waves of the form in Eq. (3.3) propagating outwards from Ω_{BD} (waves with

$r_1 > 0$) are completely absorbed into and then attenuated in the x_1-direction in $\Omega_{\text{PM}}^{\infty}$. Thus the pressures in Ω_{BD} due to an outward propagating wave are exactly the same as the pressures of the original unbounded acoustic medium in Ω_{BD} due to the same wave.

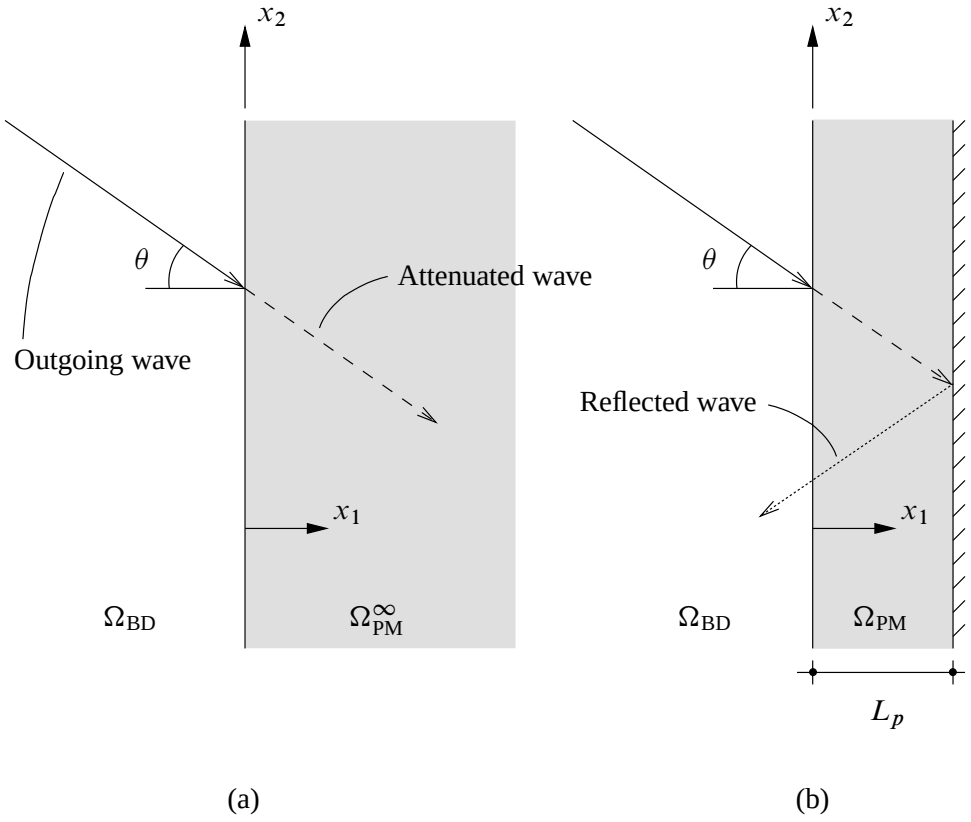

Figure 3.1. (a) A PMM adjacent to a "bounded" (truncated) domain attenuates an outgoing plane wave; (b) a PML with a fixed edge also reflects the wave back towards the bounded domain.

If this outward propagating wave is attenuated enough in a finite distance, then $\Omega_{\text{PM}}^{\infty}$ can be truncated by a fixed boundary without any significant reflection of the wave. Shown in Fig. 3.1b, this layer Ω_{PM} of the PMM is termed the PML. If the wave reflection from the fixed boundary is not significant, then the pressures of this system ($\Omega_{\text{BD}} \cup \Omega_{\text{PM}}$) in Ω_{BD} should be almost the same as those of the unbounded acoustic domain in Ω_{BD}.

The effect of domain truncation in the PMM is analysed by studying the reflection of plane waves by the fixed boundary. As shown in Fig. 3.1b, the plane wave, incident at an angle θ and of unit amplitude as it enters the PML, is reflected from the fixed boundary. Therefore, the total wave motion can be represented as

$$\bar{p}(\boldsymbol{x}) = \exp\left[-\mathrm{i}k\,\tilde{\boldsymbol{x}} \cdot \boldsymbol{r}^{(I)}\right] + R\exp\left[-\mathrm{i}k\,\tilde{\boldsymbol{x}} \cdot \boldsymbol{r}^{(R)}\right] \tag{3.12}$$

where $\boldsymbol{r}^{(I)}$ and $\boldsymbol{r}^{(R)}$ are the propagation directions of the incident and reflected waves respectively.

Imposing $\bar{p}(\boldsymbol{x}) \equiv 0$ for $x_1 = L_P$ and for all x_2, and substituting $r_1^{(I)} = \cos\theta$, gives

$$|R| = \exp\left[-2F_1(L_P)\cos\theta\right] \tag{3.13}$$

which is also the amplitude of the reflected wave as it exits the PML. This reflection coefficient is controlled by the choice of the parameters f_1 and L_P — independently of the size of the bounded domain to which the PML is adjacent — and is influenced by the angle of incidence. This suggests that the bounded domain may be restricted to the region of interest in the analysis, thus lowering the computational cost, if the parameters and the orientation of the PML are chosen appropriately.

The above arguments considered a two-dimensional problem only for the sake of illustration; the same reasoning may be extended to three-dimensional problems to reach an identical conclusion.

3.5 Finite-element implementation

A finite-element implementation of the PMM may be obtained by rewriting its governing equations in a tensorial form. Consider two rectangular Cartesian coordinate systems for the plane as follows: 1) an $\{x_i\}$ system, with respect to an orthonormal basis $\{\boldsymbol{e}_i\}$, and 2) an $\{x_i'\}$ system, with respect to another orthonormal basis $\{\boldsymbol{e}_i'\}$, with the two bases related by the rotation-of-basis matrix $\mathbf{Q}$, with components $Q_{ij} := \boldsymbol{e}_i \cdot \boldsymbol{e}_j'$. Equation (3.6) can be re-written in terms of the coordinates x_i' by replacing x_i by x_i' throughout, as (no summation)

$$\sum_i \frac{1}{\lambda_i(x_i')}\frac{\partial \bar{\varphi}_i'}{\partial x_i'} = -\omega^2 \rho \bar{p} \tag{3.14a}$$

$$\bar{\varphi}_i' = \kappa \bar{\gamma}_i' \tag{3.14b}$$

$$\bar{\gamma}_i' = \frac{1}{\lambda_i(x_i')}\frac{\partial \bar{p}}{\partial x_i'} \tag{3.14c}$$

representing a PMM wherein waves are attenuated in the $\boldsymbol{e}_1'$ and $\boldsymbol{e}_2'$ directions, rather than in the $\boldsymbol{e}_1$ and $\boldsymbol{e}_2$ directions as in Eq. (3.6); $\bar{\varphi}_i'$ and $\bar{\gamma}_i'$ are the components of the vectors $\bar{\boldsymbol{\varphi}} := \bar{\varphi}_i \boldsymbol{e}_i$ and $\bar{\boldsymbol{\gamma}} := \bar{\gamma}_i \boldsymbol{e}_i$, respectively, in the basis $\{\boldsymbol{e}_i'\}$. Further, define a function $\mathcal{J}$ as

$$\mathcal{J} = \begin{cases} \lambda_1(x_1')\lambda_2(x_2') & \text{for two-dimensional problems} \\ \lambda_1(x_1')\lambda_2(x_2')\lambda_3(x_3') & \text{for three-dimensional problems} \end{cases} \tag{3.15}$$

i.e., the determinant of the Jacobian of the coordinate stretch. By multiplying Eq. (3.14a) with $\mathcal{J}$ and using the fact that λ_i is a function of x_i' only, it can be rewritten as

$$\boldsymbol{\nabla}' \cdot \left(\mathcal{J}\boldsymbol{\Lambda}'\bar{\boldsymbol{\varphi}}\right) = -\omega^2 \rho \mathcal{J} \bar{p} \tag{3.16a}$$

$$\bar{\boldsymbol{\varphi}}' = \kappa \bar{\boldsymbol{\gamma}}' \tag{3.16b}$$

$$\bar{\boldsymbol{\gamma}}' = \boldsymbol{\Lambda}'\left(\boldsymbol{\nabla}'\bar{p}\right) \tag{3.16c}$$

where $\bar{\boldsymbol{\varphi}}'$, $\bar{\boldsymbol{\gamma}}'$ and $\boldsymbol{\nabla}'$ are column vectors with components $\bar{\varphi}_i'$, $\bar{\gamma}_i'$ and $\partial/\partial x_i'$, respectively, and

$$\boldsymbol{\Lambda}' = \begin{cases} \text{diag}\left(1/\lambda_1(x_1'), 1/\lambda_2(x_2')\right) & \text{for two-dimensional problems} \\ \text{diag}\left(1/\lambda_1(x_1'), 1/\lambda_2(x_2'), 1/\lambda_3(x_3')\right) & \text{for three-dimensional problems} \end{cases} \tag{3.17}$$

The various primed quantities in Eq. (3.16) can be transformed to the basis $\{\boldsymbol{e}_i\}$ to obtain

$$\boldsymbol{\nabla} \cdot (\mathcal{J} \boldsymbol{\Lambda} \bar{\boldsymbol{\varphi}}) = -\omega^2 \rho \mathcal{J} \bar{p} \tag{3.18a}$$

$$\bar{\boldsymbol{\varphi}} = \kappa \bar{\boldsymbol{\gamma}} \tag{3.18b}$$

$$\bar{\boldsymbol{\gamma}} = \boldsymbol{\Lambda} \, (\boldsymbol{\nabla} \bar{p}) \tag{3.18c}$$

where

$$\boldsymbol{\Lambda} = \mathbf{Q} \boldsymbol{\Lambda}' \mathbf{Q}^T \tag{3.19}$$

is termed the *stretch tensor.* Because this tensor is diagonal in the basis $\{\boldsymbol{e}_i'\}$, this basis is termed the *characteristic basis* of the PMM. In tensorial notation, Eq. (3.18) becomes

$$\text{div}\,(\mathcal{J} \boldsymbol{\Lambda} \bar{\boldsymbol{\varphi}}) = -\omega^2 \rho \mathcal{J} \bar{p} \tag{3.20a}$$

$$\bar{\boldsymbol{\varphi}} = \kappa \bar{\boldsymbol{\gamma}} \tag{3.20b}$$

$$\bar{\boldsymbol{\gamma}} = \boldsymbol{\Lambda} \, (\text{grad}\, \bar{p}) \tag{3.20c}$$

The weak form of Eq. (3.20a) is derived by multiplying it with an arbitrary weighting function w residing in an appropriate admissible space, and then integrating over the entire computational domain Ω using integration-by-parts and the divergence theorem to obtain

$$\int_\Omega \text{grad}\, w \cdot (\boldsymbol{\Lambda} \bar{\boldsymbol{\varphi}}) \; \mathcal{J} \text{d}\Omega - \omega^2 \int_\Omega \rho w \bar{p} \; \mathcal{J} \text{d}\Omega = \int_\Gamma w \, (\boldsymbol{\Lambda} \bar{\boldsymbol{\varphi}}) \cdot \boldsymbol{n} \, \mathcal{J} \text{d}\Gamma, \tag{3.21}$$

where $\Gamma := \partial\Omega$ is the boundary of Ω and $\boldsymbol{n}$ is the unit outward normal to Γ. Assuming element-wise interpolations of $\bar{p}$ and w in terms of nodal shape functions $\boldsymbol{N}$, imposing Eqs. (3.20b) and (3.20c) point-wise in Eq. (3.21), and restricting the domain integrals to the element domain $\Omega = \Omega^e$ gives the "stiffness" and "mass" matrices for a PML element. In terms of nodal submatrices, these are

$$\mathbf{h}_{IJ}^e = \int_{\Omega^e} (\boldsymbol{\Lambda} \, \text{grad}\, N_I)^T \, \kappa \, (\boldsymbol{\Lambda} \, \text{grad}\, N_J) \; \mathcal{J} \text{d}\Omega \tag{3.22a}$$

$$\mathbf{s}_{IJ}^e = \int_{\Omega^e} \rho N_I N_J \, \mathcal{J} \text{d}\Omega, \tag{3.22b}$$

where I and J denote node numbers of the element. In Eq. (3.22), the functions λ_i in $\boldsymbol{\Lambda}$ and in $\mathcal{J}$ are defined globally on the computational domain, not element-wise. The right-hand side in Eq. (3.21) is conveniently ignored by assuming that $(\boldsymbol{\Lambda} \bar{\boldsymbol{\varphi}}) \cdot \boldsymbol{n} = 0$ on a free boundary of the PMM. Note that these system matrices for the PMM could also have been obtained by applying coordinate-stretching to the corresponding matrices for the acoustic medium.

For two-dimensional problems, the above is the FE implementation presented by Collino and Monk [74] and studied further by Harari et al. [44]. These element matrices are symmetric, but intrinsically complex-valued and frequency-dependent. Hence, the system matrices for Ω will be complex, symmetric, and sparse, the PML contributions to which will have to recomputed for each frequency.

3.6 Numerical results

3.6.1 A two-dimensional problem

Consider a two-dimensional acoustic waveguide in the form of a semi-infinite layer, as shown in Fig. 3.2a, with pressures governed by Eq. (3.2) with the following boundary conditions:

$$\bar{p}(\boldsymbol{x}) = 0 \qquad \text{at } x_2 = d,\ \forall x_1 > 0 \tag{3.23a}$$

$$\frac{\partial \bar{p}}{\partial x_2} = 0 \qquad \text{at } x_2 = 0,\ \forall x_1 > 0 \tag{3.23b}$$

$$\frac{\partial \bar{p}}{\partial x_1} = -\rho\psi(x_2/d) \qquad \text{at } x_1 = 0,\ \forall x_2 \in [0, d] \tag{3.23c}$$

and a radiation condition for $x_1 \to \infty$, where ψ is the mode of excitation, given by

$$\psi(s) = 4s(1-s), \qquad s \in [0, 1] \tag{3.24}$$

The wave motion in this waveguide it is dispersive, and consists of not only propagating modes but also an infinite number of evanescent modes, with the propagation (and decay) in the x_1-direction. The response of the system is calculated as the force at $x_1 = 0$ in the mode ψ:

$$\bar{\mathrm{F}} = \int_0^H \psi(x_2/d)\, \bar{p}(x_1 = 0)\, \mathrm{d}x_2 \tag{3.25}$$

This semi-infinite layer is modelled using the bounded-domain-PML model shown in Fig. 3.2b, composed of a bounded domain Ω_{BD} and a PML Ω_{PM}. Motivated by the realistic choice of a stretching function in Eq. (2.18), the stretching functions λ_i are chosen as (no summation)

$$\lambda_i(x_i) := \left[1 + \frac{f_i(x_i)}{a_0}\right] - \mathrm{i}\frac{f_i(x_i)}{a_0} \tag{3.26}$$

to attenuate both propagating and evanescent waves in the system, with f_1 chosen to be linear in the PML — in view of the conclusions of Sec. 2.6 — and $f_2 = 0$ matching the corresponding function in Ω_{BD}. A stretching function of the form in Eq. (3.8) will not be adequate for evanescent modes, an observation mirrored in electromagnetics literature [75, 76], where alternative choices of the stretching function have been considered for attenuating evanescent waves. For purposes of comparison, the layer is also modelled using a viscous-dashpot model [16], with consistent dashpots

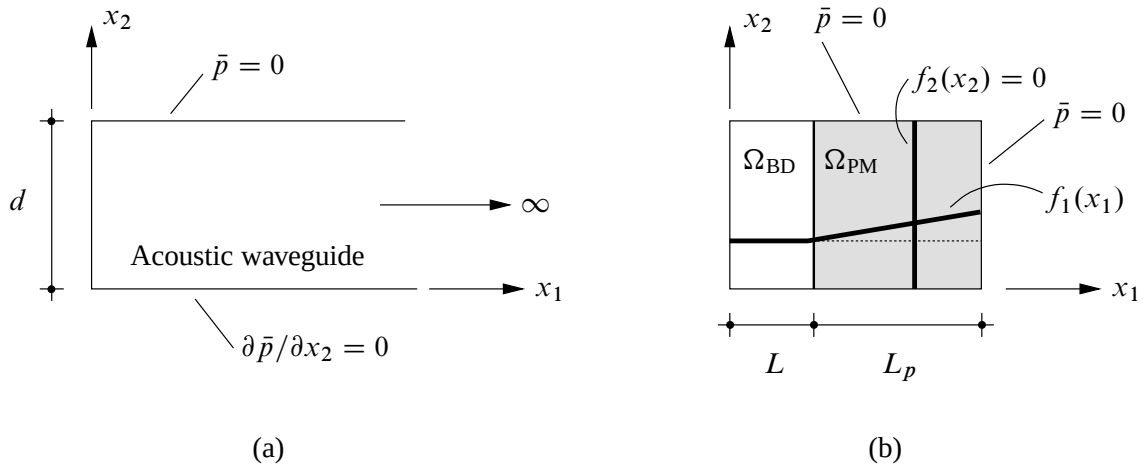

Figure 3.2. (a) Two-dimensional acoustic waveguide of depth d; (b) a PML model.

placed at the edge $x_1 = L + L_P$, and the entire domain $\Omega_{\text{BD}} \cup \Omega_{\text{PM}}$ taken to be acoustic. A uniform finite-element mesh of square four-node bilinear isoparametric elements is used to discretise the entire bounded domain for either model, with 16 elements in the depth of the waveguide.

Figure 3.3 shows the harmonic modal force due to the pressure in the waveguide [Eq. (3.25)] computed using the PML model and the viscous dashpot model, against an analytical solution [77]. It is seen that the results from the PML model are highly accurate, even though they are obtained using a small computational domain and at a low cost: the cost of the PML model is similar to that of the dashpot model, and the grossly inaccurate results from the latter emphasize the small size of the computational domain. Significantly, the high accuracy of the PML results demonstrates that the stretching function of Eq. (3.26) adequately attenuates the infinite number of evanescent modes in this waveguide.

3.6.2 A three-dimensional problem

Consider a three-dimensional acoustic waveguide in the form of a semi-infinite prismatic channel of trapezoidal cross-section, as shown in Fig. 3.4a, with pressures governed by Eq. (3.2) with the following boundary conditions:

$$\bar{p}(\boldsymbol{x}) = 0 \qquad \text{at } x_2 = d \tag{3.27a}$$

$$\frac{\partial \bar{p}}{\partial n} = 0 \qquad \text{at lateral and bottom surfaces} \tag{3.27b}$$

$$\frac{\partial \bar{p}}{\partial x_1} = -\rho \qquad \text{at } x_1 = 0 \tag{3.27c}$$

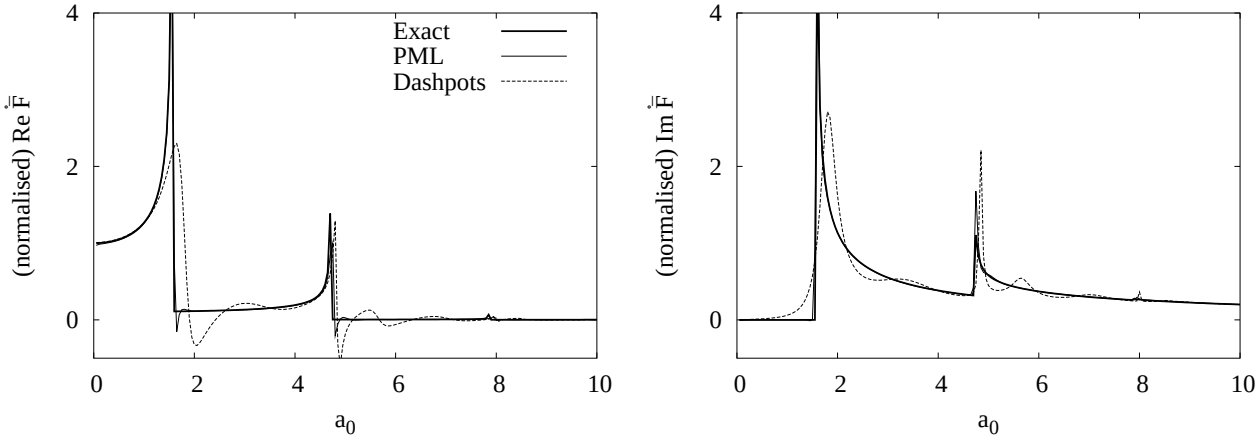

Figure 3.3. Harmonic modal force due to dynamic pressure in two-dimensional waveguide, computed using a PML model as well as a viscous dashpot model, and normalised against its value at $a_0 = 0$; $L = d/2$, $L_P = d$, $f_1(x_1) = 10\langle x_1 - L\rangle / L_P$; $\kappa = 1$, $\rho = 1$; $\langle x\rangle := (x + |x|)/2$.

and a radiation condition for $x_1 \to \infty$, where $\partial/\partial n$ is the normal derivative at a surface. The response of the system is calculated as the force at $x_1 = 0$:

$$\bar{\mathrm{F}} = \int_{\{x_1=0\}} \bar{p}(x_1 = 0)\, \mathrm{d}x_2 \mathrm{d}x_3 \tag{3.28}$$

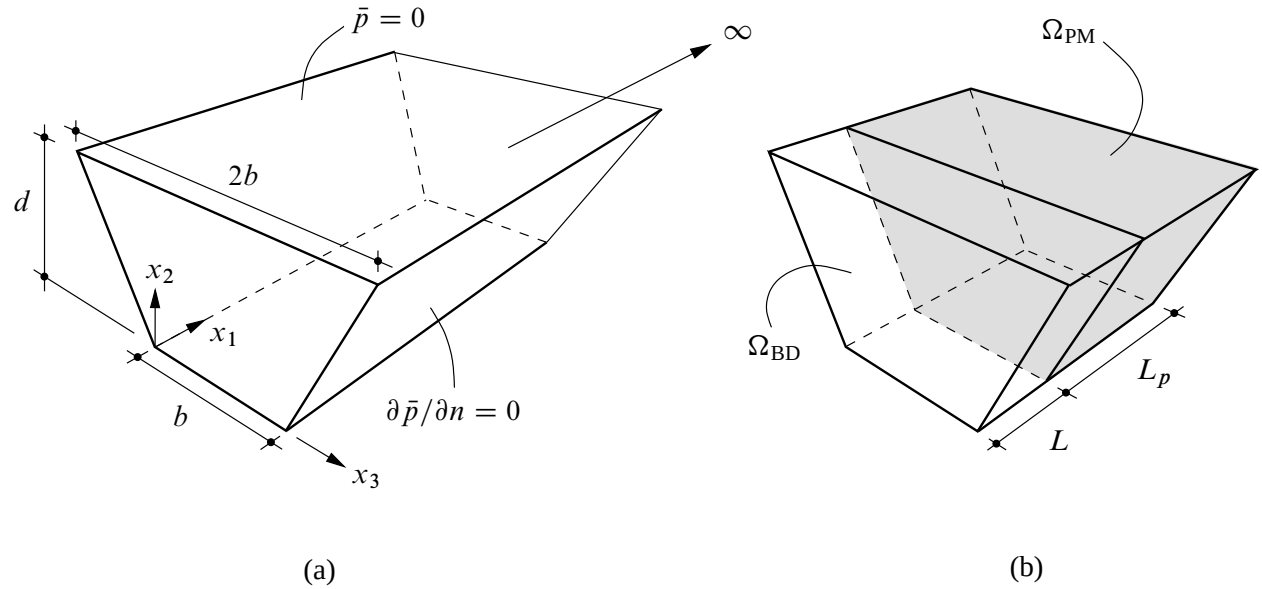

Figure 3.4. (a) Three-dimensional acoustic waveguide of depth d; (b) a PML model.

This semi-infinite channel is modelled using the bounded-domain-PML model shown in Fig. 3.4b, composed of a bounded domain Ω_{BD} and a PML Ω_{PM}. The stretching functions are chosen as in

Eq. (3.26), with f_1 chosen to be linear in the PML and $f_2 = f_3 = 0$ matching the corresponding function in Ω_{BD}. For purposes of comparison, the layer is also modelled using a viscous-dashpot model [16], with consistent dashpots placed at the edge $x_1 = L + L_P$, and the entire domain $\Omega_{\mathrm{BD}} \cup \Omega_{\mathrm{PM}}$ taken to be acoustic. A uniform finite-element mesh of eight-node trilinear isoparametric elements is used to discretise the entire bounded domain for either model, with 20 elements across and along the depth of the channel, and 20 elements per unit length in the x_1 direction.

Figure 3.5 shows the harmonic force due to the pressure in the waveguide [Eq. (3.28)] computed using the PML model and the viscous dashpot model, against a semi-analytical solution [78]. It is seen that the results from the PML model are highly accurate, even though they are obtained using a small computational domain and at a low cost: the cost of the PML model is similar to that of the dashpot model, and the grossly inaccurate results from the latter emphasize the small size of the computational domain.

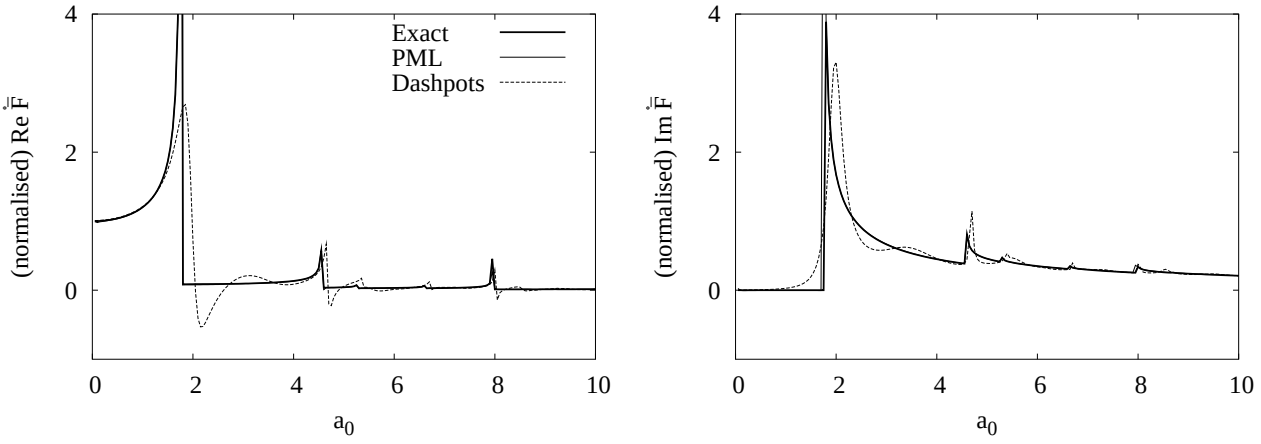

Figure 3.5. Harmonic force due to dynamic pressure in three-dimensional waveguide, computed using a PML model as well as a viscous dashpot model, and normalised against its value at $a_0 = 0$; $L = d/2$, $L_P = d$, $f_1(x_1) = 30\langle x_1 - L\rangle/L_P$; $\kappa = 1$, $\rho = 1$; $\langle x\rangle := (x + |x|)/2$.

4 TRANSIENT ACOUSTIC WAVES: THE SCALAR WAVE EQUATION

4.1 Introduction

The previous chapter developed the PML equations for the Helmholtz equation, which is obtained by a Fourier transform of the scalar wave equation [Eq. (3.1)]. This chapter first develops the PML equations for the scalar wave equation by applying the inverse Fourier transform to the Helmholtz PML equations, and then provides a finite-element implementation of these equations.

Recall that, for both two- and three-dimensional problems, the equations for the time-harmonic acoustic PML are [Eq. (3.20)]:

$$\operatorname{div}(\jmath\boldsymbol{\Lambda}\bar{\boldsymbol{\varphi}}) = -\omega^2\rho\jmath\bar{p} \tag{4.1a}$$

$$\bar{\boldsymbol{\varphi}} = \kappa\bar{\boldsymbol{\gamma}} \tag{4.1b}$$

$$\bar{\boldsymbol{\gamma}} = \boldsymbol{\Lambda}\,(\operatorname{grad}\bar{p}) \tag{4.1c}$$

where the specific definitions of $\boldsymbol{\Lambda}$ [Eqs. (3.19), (3.17)] and $\jmath$ [Eq. (3.15)] distinguish between the two classes of problems.

Because multiplication or division by the factor $\mathrm{i}\omega$ in the frequency domain corresponds to a derivative or an integral, respectively, in the time domain, time-harmonic equations are easily transformed into corresponding equations for transient motion if the frequency-dependence of the former is only a simple dependence on this factor. Therefore, the stretching functions are chosen to be of the form (no summation)

$$\lambda_i(x_i') := \left[1 + f_i^{\mathrm{e}}(x_i')\right] - \mathrm{i}\frac{f_i^{\mathrm{p}}(x_i')}{a_0} \tag{4.2}$$

using a normalised frequency $a_0 = kb$, where b a characteristic length of the physical problem and k is the wavenumber; the functions f_i^{e} serve to attenuate evanescent waves whereas the functions f_i^{p} serve to attenuate propagating waves.

Substituting Eq. (4.2) in Eq. (4.1) through $\boldsymbol{\Lambda}$ and $\jmath$ result in different sets of time-domain equations for two- and three-dimensional problems that are not easily amenable to expression in an unified form in a manner similar to Eq. (4.1) for time-harmonic problems. These two sets of equations are therefore discussed separately in this chapter.

4.2 Two-dimensional problems

4.2.1 Time-domain equations for the PML

For λ_i as in Eq. (4.2), the stretch tensor $\mathbf{\Lambda}$ and the product $\jmath\mathbf{\Lambda}$ for two-dimensional problems can be written as

$$\mathbf{\Lambda} = \left[\mathbf{F}^{\mathrm{e}} + \frac{1}{\mathrm{i}\omega}\mathbf{F}^{\mathrm{p}}\right]^{-1} \qquad \jmath\mathbf{\Lambda} = \tilde{\mathbf{F}}^{\mathrm{e}} + \frac{1}{\mathrm{i}\omega}\tilde{\mathbf{F}}^{\mathrm{p}} \tag{4.3}$$

where

$$\tilde{\mathbf{F}}^{\mathrm{e}} = \mathbf{Q}\tilde{\mathbf{F}}^{\mathrm{e}\prime}\mathbf{Q}^{T}, \quad \tilde{\mathbf{F}}^{\mathrm{p}} = \mathbf{Q}\tilde{\mathbf{F}}^{\mathrm{p}\prime}\mathbf{Q}^{T}, \quad \mathbf{F}^{\mathrm{e}} = \mathbf{Q}\mathbf{F}^{\mathrm{e}\prime}\mathbf{Q}^{T}, \quad \mathbf{F}^{\mathrm{p}} = \mathbf{Q}\mathbf{F}^{\mathrm{p}\prime}\mathbf{Q}^{T} \tag{4.4}$$

with

$$\tilde{\mathbf{F}}^{\mathrm{e}\prime} := \mathrm{diag}\left(1 + f_2^{\mathrm{e}}(x_2'), 1 + f_1^{\mathrm{e}}(x_1')\right), \quad \tilde{\mathbf{F}}^{\mathrm{p}\prime} := \mathrm{diag}\left(f_2^{\mathrm{p}}(x_2'), f_1^{\mathrm{p}}(x_1')\right) \times C/b \tag{4.5a}$$

and

$$\mathbf{F}^{\mathrm{e}\prime} := \mathrm{diag}\left(1 + f_1^{\mathrm{e}}(x_1'), 1 + f_2^{\mathrm{e}}(x_2')\right), \quad \mathbf{F}^{\mathrm{p}\prime} := \mathrm{diag}\left(f_1^{\mathrm{p}}(x_1'), f_2^{\mathrm{p}}(x_2')\right) \times C/b \tag{4.5b}$$

Equation (4.1c) is premultiplied by $\mathrm{i}\omega\mathbf{\Lambda}^{-1}$, Eqs. (4.2) and (4.3) are substituted into Eq. (4.1), and the inverse Fourier transform is applied to the resultant to obtain the time-domain equations for the two-dimensional acoustic PML:

$$\mathrm{div}\,\tilde{\boldsymbol{\varphi}} = \rho f_{\mathrm{m}}\ddot{p} + \rho\frac{C}{b}f_{\mathrm{c}}\dot{p} + \rho\left(\frac{C}{b}\right)^2 f_{\mathrm{k}}p \tag{4.6a}$$

$$\boldsymbol{\varphi} = \kappa\boldsymbol{\gamma} \tag{4.6b}$$

$$\mathbf{F}^{\mathrm{e}}\dot{\boldsymbol{\gamma}} + \mathbf{F}^{\mathrm{p}}\boldsymbol{\gamma} = \mathrm{grad}\,\dot{p} \tag{4.6c}$$

where

$$\tilde{\boldsymbol{\varphi}} := \tilde{\mathbf{F}}^{\mathrm{e}}\boldsymbol{\varphi} + \tilde{\mathbf{F}}^{\mathrm{p}}\boldsymbol{\Phi}, \qquad \text{with} \quad \boldsymbol{\Phi} := \int_0^t \boldsymbol{\varphi}\,\mathrm{d}\tau \tag{4.7}$$

and

$$\begin{aligned} f_{\mathrm{m}} &:= \left[1 + f_1^{\mathrm{e}}(x_1')\right]\left[1 + f_2^{\mathrm{e}}(x_2')\right] \\ f_{\mathrm{c}} &:= \left[1 + f_1^{\mathrm{e}}(x_1')\right] f_2^{\mathrm{p}}(x_2') + \left[1 + f_2^{\mathrm{e}}(x_2')\right] f_1^{\mathrm{p}}(x_1') \\ f_{\mathrm{k}} &:= f_1^{\mathrm{p}}(x_1') f_2^{\mathrm{p}}(x_2') \end{aligned} \tag{4.8}$$

The application of the inverse Fourier transform to obtain $\boldsymbol{\Phi}$ assumes that $\bar{\boldsymbol{\varphi}}(\omega = 0) = 0$.

4.2.2 Finite-element implementation

Equation (4.6) is implemented using a standard displacement-based finite-element approach [71]. The weak form of Eq. (4.6a) is derived by multiplying it with an arbitrary weighting function w residing in an appropriate admissible space, and then integrating over the entire computational domain Ω using integration-by-parts and the divergence theorem to obtain

$$\int_\Omega \rho f_\mathrm{m} w\, \ddot{p}\, \mathrm{d}\Omega + \int_\Omega \rho \frac{C}{b} f_\mathrm{c} w\, \dot{p}\, \mathrm{d}\Omega + \int_\Omega \rho \left(\frac{C}{b}\right)^2 f_\mathrm{k} w p\, \mathrm{d}\Omega + \int_\Omega \operatorname{grad} w \cdot \tilde{\boldsymbol{\varphi}}\, \mathrm{d}\Omega = \int_\Gamma w\, \tilde{\boldsymbol{\varphi}} \cdot \boldsymbol{n}\, \mathrm{d}\Gamma \quad (4.9)$$

where $\Gamma := \partial\Omega$ is the boundary of Ω and $\boldsymbol{n}$ is the unit outward normal to Γ. The weak form is first spatially discretised by interpolating p and w element-wise in terms of nodal quantities using appropriate nodal shape functions. This leads to the system of equations

$$\mathbf{s}\,\ddot{\boldsymbol{p}} + \mathbf{b}\,\dot{\boldsymbol{p}} + \mathbf{h}\,\boldsymbol{p} + \boldsymbol{f}_\mathrm{int} = \boldsymbol{f}_\mathrm{ext} \quad (4.10)$$

where **s**, **b** and **h** are the "mass", "damping" and "stiffness" matrices, respectively, $\boldsymbol{p}$ is a vector of nodal pressures, $\boldsymbol{f}_\mathrm{int}$ is a vector of internal "force" terms, and $\boldsymbol{f}_\mathrm{ext}$ is a vector of external "forces". These matrices and vectors are assembled from corresponding element-level matrices and vectors. In particular, the element-level constituent matrices of **s**, **b** and **h** are, respectively,

$$\mathbf{s}^e = \int_{\Omega^e} \rho f_\mathrm{m} \boldsymbol{N}^T \boldsymbol{N}\, \mathrm{d}\Omega, \quad \mathbf{b}^e = \int_{\Omega^e} \rho \frac{C}{b} f_\mathrm{c} \boldsymbol{N}^T \boldsymbol{N}\, \mathrm{d}\Omega, \quad \mathbf{h}^e = \int_{\Omega^e} \rho \left(\frac{C}{b}\right)^2 f_\mathrm{k} \boldsymbol{N}^T \boldsymbol{N}\, \mathrm{d}\Omega \quad (4.11a)$$

and the element-level internal force term is

$$\boldsymbol{f}^e = \int_{\Omega^e} \mathbf{B}^T \tilde{\boldsymbol{\varphi}}\, \mathrm{d}\Omega \quad (4.11b)$$

where $\boldsymbol{N}$ is a row vector of element-level nodal shape functions, and

$$\mathbf{B} = \begin{bmatrix} \boldsymbol{N}_{,1} \\ \boldsymbol{N}_{,2} \end{bmatrix} \quad (4.12)$$

The functions f_i^e and f_i^p are defined globally on the computational domain, not element-wise. It is conveniently assumed that $\tilde{\boldsymbol{\varphi}} \cdot \boldsymbol{n} = 0$ on a free boundary of the PML.

Equation (4.10) can be solved using a time-stepping algorithm such as the Newmark method [72, 73], along with Newton-Raphson iteration at each time step to enforce equilibrium. If Eq. (4.10) is solved, say, at time station t_{n+1}, given the solution at t_n, the Newton-Raphson iteration at this time step will require a) calculation of $\tilde{\boldsymbol{\varphi}}_{n+1}$, for calculating $\boldsymbol{f}^e_{n+1}$ [$\approx \boldsymbol{f}^e(t_{n+1})$], and b) a consistent linearisation [71, vol. 2] of $\boldsymbol{f}^e_{n+1}$ at $\boldsymbol{p}_{n+1}$ [$\approx \boldsymbol{p}^e(t_{n+1})$], where $\boldsymbol{p}^e$ is a vector of element-level nodal pressures. Therefore, Eq. (4.6c) is discretised using a backward Euler scheme on $\boldsymbol{\gamma}$ to obtain

$$\boldsymbol{\gamma}_{n+1} = \left[\frac{\mathbf{F}^\mathrm{e}}{\Delta t} + \mathbf{F}^\mathrm{p}\right]^{-1} \left[\mathbf{B}\,\dot{\boldsymbol{p}}_{n+1} + \frac{\mathbf{F}^\mathrm{e}}{\Delta t}\,\boldsymbol{\gamma}_n\right] \quad (4.13)$$

where Δt is the time-step size. The time-discrete form of Eq. (4.6b) is

$$\boldsymbol{\varphi}_{n+1} = \kappa \boldsymbol{\gamma}_{n+1} \tag{4.14}$$

Furthermore, Eq. (4.7b) is used to approximate $\boldsymbol{\Phi}_{n+1}$ as

$$\boldsymbol{\Phi}_{n+1} = \boldsymbol{\Phi}_n + \boldsymbol{\varphi}_{n+1} \Delta t \tag{4.15}$$

Equation (4.15) is substituted in Eq. (4.7a) to obtain

$$\tilde{\boldsymbol{\varphi}}_{n+1} = \Delta t \left[\frac{\tilde{\mathbf{F}}^{\mathrm{e}}}{\Delta t} + \tilde{\mathbf{F}}^{\mathrm{p}} \right] \boldsymbol{\varphi}_{n+1} + \tilde{\mathbf{F}}^{\mathrm{p}} \boldsymbol{\Phi}_n \tag{4.16}$$

This gives the internal force term

$$\boldsymbol{f}^{e}_{n+1} = \int_{\Omega^e} \mathbf{B}^T \tilde{\boldsymbol{\varphi}}_{n+1} \, \mathrm{d}\Omega \tag{4.17}$$

Linearisation of Eq. (4.17) gives

$$\Delta \boldsymbol{f}^{e}_{n+1} = \left[\int_{\Omega^e} \mathbf{B}^T \mathbf{D} \mathbf{B} \, \mathrm{d}\Omega \right] \Delta \dot{\boldsymbol{p}}_{n+1} \tag{4.18}$$

where Δ is the differential operator, and

$$\mathbf{D} = \kappa \Delta t \left[\frac{\tilde{\mathbf{F}}^{\mathrm{e}}}{\Delta t} + \tilde{\mathbf{F}}^{\mathrm{p}} \right] \left[\frac{\mathbf{F}^{\mathrm{e}}}{\Delta t} + \mathbf{F}^{\mathrm{p}} \right]^{-1} \tag{4.19}$$

i.e., this linearisation gives a tangent matrix

$$\check{\mathbf{b}}^{e} := \int_{\Omega^e} \mathbf{B}^T \mathbf{D} \mathbf{B} \, \mathrm{d}\Omega \tag{4.20}$$

which may be incorporated into the effective tangent matrix used in the time-stepping algorithm.

A skeleton of the algorithm for computing the element-level effective internal force and tangent matrix is given in Box 4.1. The matrix $\check{\mathbf{b}}^{e}$ is symmetric because $\mathbf{D}$ is symmetric by the virtue of the coaxiality of the constituent matrices. The other system matrices, $\mathbf{s}$, $\mathbf{b}$ and $\mathbf{h}$ are clearly symmetric by Eq. (4.11a). Moreover, because all these matrices are of the same form as the system matrices for an acoustic medium, the effective tangent matrix (say, as found in the Newmark scheme) of the entire computational domain will be positive definite if f^{e}_i and f^{p}_i are positive. Furthermore, since all the system matrices, $\mathbf{s}$, $\mathbf{b}$, $\check{\mathbf{b}}$ and $\mathbf{h}$ that constitute the tangent matrix are independent of $\boldsymbol{p}$, this is effectively a linear model.

Box 4.1. Computing effective force and tangent for 2D acoustic PML element.

1. Compute system matrices $\mathbf{s}^e$, $\mathbf{b}^e$ and $\mathbf{h}^e$ [Eq. (4.11a)].
2. Compute internal force $\boldsymbol{f}^e_{n+1}$ [Eq. (4.17)].
   Use $\boldsymbol{\gamma}_{n+1}$ [Eq. (4.13)], $\boldsymbol{\varphi}_{n+1}$ [Eq. (4.14)] and $\tilde{\boldsymbol{\varphi}}_{n+1}$ [Eq. (4.16)].
3. Compute tangent matrix $\check{\mathbf{b}}^e$ [Eq. (4.20)] using $\mathbf{D}$ [Eq. (4.19)].
4. Compute effective internal force $\tilde{\boldsymbol{f}}^e_{n+1}$ and tangent matrix $\tilde{\mathbf{h}}^e$:

$$\tilde{\boldsymbol{f}}^e_{n+1} = \mathbf{s}^e\,\ddot{\boldsymbol{p}}_{n+1} + \mathbf{b}^e\,\dot{\boldsymbol{p}}_{n+1} + \mathbf{h}^e\,\boldsymbol{p}_{n+1} + \boldsymbol{f}^e_{n+1}$$
$$\tilde{\mathbf{h}}^e = \alpha_{\mathrm{h}}\mathbf{h}^e + \alpha_{\mathrm{b}}\left(\mathbf{b}^e + \check{\mathbf{b}}^e\right) + \alpha_{\mathrm{s}}\mathbf{s}^e$$

   where, for example,

$$\alpha_{\mathrm{h}} = 1, \quad \alpha_{\mathrm{b}} = \frac{\gamma}{\beta\Delta t}, \quad \alpha_{\mathrm{s}} = \frac{1}{\beta\Delta t^2}$$

   for the Newmark method.

Note: The tangent matrix $\tilde{\mathbf{h}}^e$ is independent of the solution, and thus has to be computed only once. However, the internal force $\boldsymbol{f}^e_{n+1}$ has to be re-computed at each time-step because it is dependent on the solution at past times.

4.2.3 Numerical examples

Consider a two-dimensional acoustic wave guide in the form of a semi-infinite layer, as shown in Fig. 3.2a, with pressures governed by Eq. (3.1) with the following boundary conditions:

$$p(\boldsymbol{x}, t) = 0 \qquad \text{at } x_2 = d,\ \forall x_1 > 0 \tag{4.21a}$$
$$\frac{\partial p}{\partial x_2} = 0 \qquad \text{at } x_2 = 0,\ \forall x_1 > 0 \tag{4.21b}$$
$$\frac{\partial p}{\partial x_1} = -\rho\psi(x_2/d)u_0(t) \qquad \text{at } x_1 = 0,\ \forall x_2 \in [0, d] \tag{4.21c}$$

and a radiation condition for $x_1 \to \infty$, where ψ is the mode of excitation, given by Eq. (3.24), and $u_0(t)$ is the excitation-history, given by Eq. (A3). The response of the system is calculated as the force at $x_1 = 0$ in the mode ψ:

$$\mathrm{F}(t) = \int_0^H \psi(x_2/d)\, p(x_1 = 0, t)\, \mathrm{d}x_2 \tag{4.22}$$

This semi-infinite layer is modelled using the bounded-domain-PML model shown in Fig. 3.2b, composed of a bounded domain Ω_{BD} and a PML Ω_{PM}, with the attenuation functions in Eq. (4.2) chosen as $f_1^{\mathrm{e}} = f_1^{\mathrm{p}} = f$, where f is linear in the PML, and $f_2^{\mathrm{e}} = f_2^{\mathrm{p}} = 0$. For comparison, the layer is also modelled using viscous dashpots [16], with consistent dashpots placed at the edge

$x_1 = L + L_P$, and the entire domain $\Omega_{\text{BD}} \cup \Omega_{\text{PM}}$ taken to be acoustic. A uniform finite-element mesh of square four-node bilinear isoparametric elements is used to discretise the entire bounded domain for either model, with 16 elements in the depth of the waveguide.

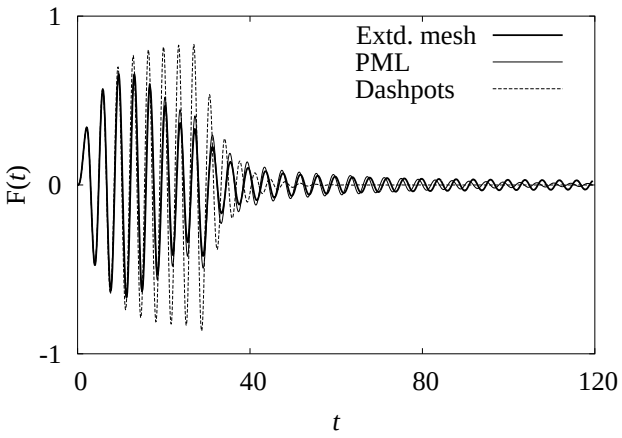

Figure 4.1. Transient modal force due to dynamic pressure in two-dimensional waveguide, computed using a PML model as well as a viscous dashpot model; $L = d/2$, $L_P = d$, $f_1(x_1) = 10\langle x_1 - L\rangle/L_P$; $\kappa = 1$, $\rho = 1$; $t_d = 30$, $\omega_f = 1.85$.

Figure 4.1 show the transient modal force due to the pressure in the waveguide [Eq. (4.22)], computed using the PML model and the viscous dashpot model, against results from an extended-mesh model used as a benchmark; this extended-mesh model is a viscous-dashpot model of depth d and length $60d$. Based on a comparison of the frequency-domain responses of the PML and the viscous dashpot models, the values of ω_f were chosen as the excitation frequencies where the two responses are significantly different. The results from the PML model follow the extended-mesh results closely, even though the domain is small enough that the viscous-dashpot boundary generates spurious reflections, manifested in the higher response amplitudes. Moreover, these accurate results from the PML model are obtained at a low computational cost: the cost of the PML model is observed to be approximately 1.4 times that of the dashpot model, which itself is extremely inexpensive.

4.2.4 Caveat emptor

The time-domain equations for the PML were obtained by a special choice of the stretching functions — Eq. (4.2) — that enabled transformation of the frequency domain PML equations into the time domain. However, these stretching functions differ from those used for frequency-domain analysis, given by Eq. (3.26); these stretching functions produced accurate results in the frequency domain, even for problems with significant evanescent modes in their wave motion [Sec. 3.6.1].

Because the real part of the complex-valued stretching function serves to attenuate evanescent waves, and because the difference between the time-domain and the frequency-domain stretching

functions is only in the real part, it is valid to ask whether the time-domain stretching functions are adequate for evanescent waves. Note that it is difficult to employ the frequency-domain stretching function [Eq. (3.26)] towards a time-domain model because the frequency-dependence of the real part of the stretching function is not through the factor $i\omega$. Because the PML approach is fundamentally a frequency-domain approach, it is valid to test the adequacy of the time-domain stretching function [Eq. (4.2)] by using it to obtain frequency-domain results.

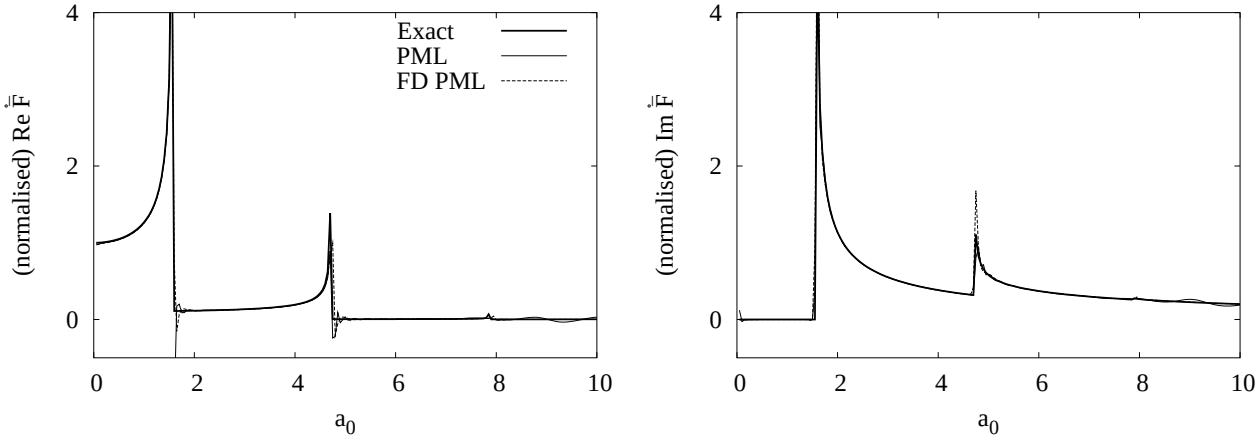

Figure 4.2. Harmonic modal force due to dynamic pressure in two-dimensional waveguide, computed using PML models with two different forms of the stretching function: "PML" from a stretching function that can be implemented in the time domain, and "FD PML" from a stretching function that is more accurate but is only suitable for the frequency domain; normalised against its value at $a_0 = 0$; $L = d/2$, $L_P = d$, $f_1(x_1) = 10\langle x_1 - L\rangle / L_P$; $\kappa = 1$, $\rho = 1$; $\langle x\rangle := (x + |x|)/2$.

Figure 4.2 compares the harmonic modal force due to the pressure in the waveguide [Eq. (3.25)] obtained from PML models using the two stretching functions, against an analytical solution [77]. The mesh used for the PML models is the same as those used for time-domain analysis; the results are obtained using the frequency-domain FE formulation presented earlier 3.5. It is seen that the time-domain stretching function [Eq. (4.2)] produces results — denoted by "PML" — that closely match results from the frequency-domain-only stretching function [Eq. (3.26)], denoted by "FD PML". This suggests that for this system, the time-domain stretching functions are adequate for attenuating the evanescent modes. However, it should be noted that this adequacy may depend on the particular excitation-response combination under consideration: the dynamic stiffness of a semi-infinite elastic layer undergoing anti-plane motion — essentially an "inverse" of the excitation-response studied above — is computed inaccurately for higher frequencies if the time-domain stretching function is used [79].

4.3 Three-dimensional problems

4.3.1 Time-domain equations for the PML

For three-dimensional problems, the stretch tensor $\mathbf{\Lambda}$ may still be expressed as in Eq. (4.3a), but with $\mathbf{F}^{\mathrm{e}\prime}$ and $\mathbf{F}^{\mathrm{p}\prime}$ now given by

$$\begin{aligned} \mathbf{F}^{\mathrm{e}\prime} &:= \operatorname{diag}\left(1 + f_1^{\mathrm{e}}(x_1'),\, 1 + f_2^{\mathrm{e}}(x_2'),\, 1 + f_3^{\mathrm{e}}(x_3')\right), \\ \mathbf{F}^{\mathrm{p}\prime} &:= \operatorname{diag}\left(f_1^{\mathrm{p}}(x_1'),\, f_2^{\mathrm{p}}(x_2'),\, f_3^{\mathrm{p}}(x_3')\right) \times C/b \end{aligned} \tag{4.23}$$

However, the product $\jmath\mathbf{\Lambda}$ is now given by

$$\jmath\mathbf{\Lambda} = \tilde{\mathbf{F}}^{\mathrm{ee}} + \frac{1}{\mathrm{i}\omega}\tilde{\mathbf{F}}^{\mathrm{ep}} - \frac{1}{\omega^2}\tilde{\mathbf{F}}^{\mathrm{pp}} \tag{4.24}$$

where

$$\tilde{\mathbf{F}}^{\mathrm{ee}} = \mathbf{Q}\tilde{\mathbf{F}}^{\mathrm{ee}\prime}\mathbf{Q}^T, \quad \tilde{\mathbf{F}}^{\mathrm{ep}} = \mathbf{Q}\tilde{\mathbf{F}}^{\mathrm{ep}\prime}\mathbf{Q}^T, \quad \tilde{\mathbf{F}}^{\mathrm{pp}} = \mathbf{Q}\tilde{\mathbf{F}}^{\mathrm{pp}\prime}\mathbf{Q}^T \tag{4.25}$$

with

$$\begin{aligned} \tilde{\mathbf{F}}^{\mathrm{ee}\prime} &:= \operatorname{diag}\left(f_{23}^{\mathrm{ee}}, f_{13}^{\mathrm{ee}}, f_{12}^{\mathrm{ee}}\right) \\ \tilde{\mathbf{F}}^{\mathrm{ep}\prime} &:= \operatorname{diag}\left(f_{23}^{\mathrm{ep}}, f_{13}^{\mathrm{ep}}, f_{12}^{\mathrm{ep}}\right) \times C/b \\ \tilde{\mathbf{F}}^{\mathrm{pp}\prime} &:= \operatorname{diag}\left(f_{23}^{\mathrm{pp}}, f_{13}^{\mathrm{pp}}, f_{12}^{\mathrm{pp}}\right) \times (C/b)^2 \end{aligned} \tag{4.26a}$$

where f_{ij}^{ee} etc. are defined as

$$\begin{aligned} f_{ij}^{\mathrm{ee}} &:= \left[1 + f_i^{\mathrm{e}}(x_i')\right]\left[1 + f_j^{\mathrm{e}}(x_j')\right] \\ f_{ij}^{\mathrm{ep}} &:= \left[1 + f_i^{\mathrm{e}}(x_i')\right] f_j^{\mathrm{p}}(x_j') + \left[1 + f_j^{\mathrm{e}}(x_j')\right] f_i^{\mathrm{p}}(x_i') \\ f_{ij}^{\mathrm{pp}} &:= f_i^{\mathrm{p}}(x_i')\, f_j^{\mathrm{p}}(x_j') \end{aligned} \tag{4.26b}$$

Equation (4.1c) is premultiplied by $\mathrm{i}\omega\mathbf{\Lambda}^{-1}$, Eqs. (4.2), (4.3a) and (4.24) are substituted into Eq. (4.1), and the inverse Fourier transform is applied to the resultant to obtain the time-domain equations for the three-dimensional acoustic PML:

$$\operatorname{div}\tilde{\boldsymbol{\varphi}} = \rho f_{\mathrm{M}}\,\ddot{p} + \rho\frac{C}{b}f_{\mathrm{C}}\,\dot{p} + \rho\left(\frac{C}{b}\right)^2 f_{\mathrm{K}}\,p + \rho\left(\frac{C}{b}\right)^3 f_{\mathrm{H}}\,P \tag{4.27a}$$

$$\boldsymbol{\varphi} = \kappa\boldsymbol{\gamma} \tag{4.27b}$$

$$\mathbf{F}^{\mathrm{e}}\dot{\boldsymbol{\gamma}} + \mathbf{F}^{\mathrm{p}}\boldsymbol{\gamma} = \operatorname{grad}\dot{p} \tag{4.27c}$$

where

$$P := \int_0^t p\,\mathrm{d}\tau \tag{4.28}$$

$$\tilde{\boldsymbol{\varphi}} := \tilde{\mathbf{F}}^{\mathrm{ee}}\boldsymbol{\varphi} + \tilde{\mathbf{F}}^{\mathrm{ep}}\boldsymbol{\Phi} + \tilde{\mathbf{F}}^{\mathrm{pp}}\tilde{\boldsymbol{\Phi}}, \qquad \text{with} \quad \boldsymbol{\Phi} := \int_0^t \boldsymbol{\varphi}\,\mathrm{d}\tau, \quad \tilde{\boldsymbol{\Phi}} := \int_0^t \boldsymbol{\Phi}\,\mathrm{d}\tau \tag{4.29}$$

and

$$
\begin{aligned}
f_{\mathrm{M}} &:= \left[1 + f_1^{\mathrm{e}}(x_1')\right]\left[1 + f_2^{\mathrm{e}}(x_2')\right]\left[1 + f_3^{\mathrm{e}}(x_3')\right] \\
f_{\mathrm{C}} &:= \left[1 + f_1^{\mathrm{e}}(x_1')\right]\left[1 + f_2^{\mathrm{e}}(x_2')\right] f_3^{\mathrm{p}}(x_3') + \left[1 + f_1^{\mathrm{e}}(x_1')\right]\left[1 + f_3^{\mathrm{e}}(x_3')\right] f_2^{\mathrm{p}}(x_2') \\
&\qquad + \left[1 + f_2^{\mathrm{e}}(x_2')\right]\left[1 + f_3^{\mathrm{e}}(x_3')\right] f_1^{\mathrm{p}}(x_1') \\
f_{\mathrm{K}} &:= f_1^{\mathrm{p}}(x_1') f_2^{\mathrm{p}}(x_2')\left[1 + f_3^{\mathrm{e}}(x_3')\right] + f_2^{\mathrm{p}}(x_2') f_3^{\mathrm{p}}(x_3')\left[1 + f_1^{\mathrm{e}}(x_1')\right] \\
&\qquad + f_1^{\mathrm{p}}(x_1') f_3^{\mathrm{p}}(x_3')\left[1 + f_2^{\mathrm{e}}(x_2')\right] \\
f_{\mathrm{H}} &:= f_1^{\mathrm{p}}(x_1') f_2^{\mathrm{p}}(x_2') f_3^{\mathrm{p}}(x_3')
\end{aligned}
\tag{4.30}
$$

The application of the inverse Fourier transform to obtain $\boldsymbol{\Phi}$ assumes that $\bar{\boldsymbol{\varphi}}(\omega = 0) = 0$.

4.3.2 Finite-element implementation

Equation (4.27) is implemented using a standard displacement-based finite-element approach [71]. The weak form of Eq. (4.27a) is derived by multiplying it with an arbitrary weighting function w residing in an appropriate admissible space, and then integrating over the entire computational domain Ω using integration-by-parts and the divergence theorem to obtain

$$
\begin{aligned}
&\int_\Omega \rho f_{\mathrm{M}}\, w\, \ddot{p}\, \mathrm{d}\Omega + \int_\Omega \rho \frac{C}{b} f_{\mathrm{C}}\, w\, \dot{p}\, \mathrm{d}\Omega + \int_\Omega \rho \left(\frac{C}{b}\right)^2 f_{\mathrm{K}}\, w p\, \mathrm{d}\Omega \\
&\qquad + \int_\Omega \rho \left(\frac{C}{b}\right)^3 f_{\mathrm{H}}\, w P\, \mathrm{d}\Omega + \int_\Omega \operatorname{grad} w \cdot \tilde{\boldsymbol{\varphi}}\, \mathrm{d}\Omega = \int_\Gamma w\, \tilde{\boldsymbol{\varphi}} \cdot \boldsymbol{n}\, \mathrm{d}\Gamma
\end{aligned}
\tag{4.31}
$$

where $\Gamma := \partial\Omega$ is the boundary of Ω and $\boldsymbol{n}$ is the unit outward normal to Γ. The weak form is first spatially discretised by interpolating p and w element-wise in terms of nodal quantities using appropriate nodal shape functions. This leads to the system of equations

$$
\mathbf{s}\,\ddot{\boldsymbol{p}} + \mathbf{b}\,\dot{\boldsymbol{p}} + \mathbf{h}\,\boldsymbol{p} + \mathbf{H}\mathcal{P} + \boldsymbol{f}_{\mathrm{int}} = \boldsymbol{f}_{\mathrm{ext}}
\tag{4.32}
$$

where $\mathcal{P}$ is the time-integral of $\boldsymbol{p}$, $\mathbf{H}$ is the coefficient matrix associated with $\mathcal{P}$, and the other terms have the same connotation as in Eq. (4.10). The element-level constituent matrices of $\mathbf{s}$, $\mathbf{b}$, $\mathbf{h}$ and $\mathbf{H}$ are, respectively,

$$
\begin{aligned}
\mathbf{s}^e &= \int_{\Omega^e} \rho f_{\mathrm{M}} \boldsymbol{N}^T \boldsymbol{N}\, \mathrm{d}\Omega, \quad \mathbf{b}^e = \int_{\Omega^e} \rho \frac{C}{b} f_{\mathrm{C}} \boldsymbol{N}^T \boldsymbol{N}\, \mathrm{d}\Omega \\
\mathbf{h}^e &= \int_{\Omega^e} \rho \left(\frac{C}{b}\right)^2 f_{\mathrm{K}} \boldsymbol{N}^T \boldsymbol{N}\, \mathrm{d}\Omega, \quad \mathbf{H}^e = \int_{\Omega^e} \rho \left(\frac{C}{b}\right)^3 f_{\mathrm{H}} \boldsymbol{N}^T \boldsymbol{N}\, \mathrm{d}\Omega
\end{aligned}
\tag{4.33}
$$

where $\boldsymbol{N}$ is the row vector of element-level nodal shape functions, and the element-level internal force term is given by Eq. (4.11b), but with $\tilde{\boldsymbol{\varphi}}$ given by Eq. (4.29).

Equations (4.27b) and (4.27c) are discretised to obtain Eqs. (4.14) and (4.13), respectively, but with $\mathbf{F}^{\mathrm{e}}$ and $\mathbf{F}^{\mathrm{p}}$ defined using Eq. (4.23). Furthermore, $\boldsymbol{\Phi}_{n+1}$ is approximated as in Eq. (4.15), and Eq. (4.29c) is used to approximate $\tilde{\boldsymbol{\Phi}}_{n+1}$ as

$$\tilde{\boldsymbol{\Phi}}_{n+1} = \tilde{\boldsymbol{\Phi}}_n + \boldsymbol{\Phi}_{n+1}\Delta t \tag{4.34}$$

Equations (4.15) and (4.34) are substituted in Eq. (4.29a) to obtain

$$\tilde{\boldsymbol{\varphi}}_{n+1} = \tilde{\mathbf{F}}\boldsymbol{\varphi}_{n+1} + \tilde{\mathbf{F}}^{\mathrm{ec}}\boldsymbol{\Phi}_n + \tilde{\mathbf{F}}^{\mathrm{pp}}\tilde{\boldsymbol{\Phi}}_n \tag{4.35}$$

where

$$\begin{aligned} \tilde{\mathbf{F}} &:= \tilde{\mathbf{F}}^{\mathrm{ee}} + \tilde{\mathbf{F}}^{\mathrm{ep}}\Delta t + \tilde{\mathbf{F}}^{\mathrm{pp}}\Delta t^2 \\ \tilde{\mathbf{F}}^{\mathrm{ec}} &:= \tilde{\mathbf{F}}^{\mathrm{ep}} + \tilde{\mathbf{F}}^{\mathrm{pp}}\Delta t \end{aligned} \tag{4.36}$$

The internal force term is given by Eq. (4.17), its linearisation by Eq. (4.18), and the consequent tangent matrix by Eq. (4.20) but with $\mathbf{D}$ now given by

$$\mathbf{D} = \kappa\tilde{\mathbf{F}}\left[\frac{\mathbf{F}^{\mathrm{e}}}{\Delta t} + \mathbf{F}^{\mathrm{p}}\right]^{-1} \tag{4.37}$$

Finally, the time-integral of $\boldsymbol{p}$ is approximated as

$$\mathcal{P}_{n+1} = \mathcal{P}_n + \boldsymbol{p}_{n+1}\Delta t \tag{4.38}$$

Thus the term involving $\mathcal{P}$ in Eq. (4.32) may be linearised as

$$\Delta\left(\mathbf{H}\mathcal{P}_{n+1}\right) = \left(\mathbf{H}\Delta t\right)\Delta\boldsymbol{p}_{n+1} \tag{4.39}$$

A skeleton of the algorithm for computing the element-level effective internal force and tangent matrix is given in Box 4.2. The matrix $\check{\mathbf{b}}^e$ is symmetric because $\mathbf{D}$ is symmetric by the virtue of the coaxiality of the constituent matrices. The other system matrices, $\mathbf{s}$, $\mathbf{b}$, $\mathbf{h}$ and $\mathbf{H}$ are clearly symmetric by Eq. (4.33). Moreover, because all these matrices are of the same form as the system matrices for an elastic medium, the effective tangent matrix (say, as found in the Newmark scheme) of the entire computational domain will be positive definite if f_i^{e} and f_i^{p} are positive. Furthermore, since all the system matrices, $\mathbf{s}$, $\mathbf{b}$, $\check{\mathbf{b}}$, $\mathbf{h}$ and $\mathbf{H}$ that constitute the tangent matrix are independent of $\boldsymbol{p}$, this is effectively a linear model.

4.3.3 Numerical examples

Consider a three-dimensional acoustic waveguide in the form of a semi-infinite prismatic channel of trapezoidal cross-section, as shown in Fig. 3.4a, with pressures governed by Eq. (3.1) with the

Box 4.2. Computing effective force and tangent for 3D acoustic PML element.

1. Compute system matrices $\mathbf{s}^e$, $\mathbf{b}^e$, $\mathbf{h}^e$ and $\mathbf{H}^e$ [Eq. (4.33)].
2. Compute internal force $\boldsymbol{f}^e_{n+1}$ [Eq. (4.17)].
   Use $\boldsymbol{\gamma}_{n+1}$ [Eq. (4.13)], $\boldsymbol{\varphi}_{n+1}$ [Eq. (4.14)] and $\tilde{\boldsymbol{\varphi}}_{n+1}$ [Eq. (4.35)].
3. Compute tangent matrix $\check{\mathbf{b}}^e$ [Eq. (4.20)] using $\mathbf{D}$ [Eq. (4.37)].
4. Compute effective internal force $\tilde{\boldsymbol{f}}^e_{n+1}$ and tangent matrix $\tilde{\mathbf{h}}^e$:

$$\tilde{\boldsymbol{f}}^e_{n+1} = \mathbf{s}^e\,\ddot{\boldsymbol{p}}_{n+1} + \mathbf{b}^e\,\dot{\boldsymbol{p}}_{n+1} + \mathbf{h}^e\,\boldsymbol{p}_{n+1} + \mathbf{H}^e\boldsymbol{\mathcal{P}}_{n+1} + \boldsymbol{f}^e_{n+1}$$
$$\tilde{\mathbf{h}}^e = \alpha_{\mathrm{h}}\,(\mathbf{h}^e + \mathbf{H}^e\,\Delta t) + \alpha_{\mathrm{b}}\left(\mathbf{b}^e + \check{\mathbf{b}}^e\right) + \alpha_{\mathrm{s}}\mathbf{s}^e$$

   where, for example,

$$\alpha_{\mathrm{h}} = 1, \quad \alpha_{\mathrm{b}} = \frac{\gamma}{\beta\Delta t}, \quad \alpha_{\mathrm{s}} = \frac{1}{\beta\Delta t^2}$$

   for the Newmark method.

Note: The tangent matrix $\tilde{\mathbf{h}}^e$ is independent of the solution, and thus has to be computed only once. However, the internal force $\boldsymbol{f}^e_{n+1}$ has to be re-computed at each time-step because it is dependent on the solution at past times.

following boundary conditions:

$$p(\boldsymbol{x}, t) = 0 \qquad \text{at } x_2 = d \tag{4.40a}$$
$$\frac{\partial p}{\partial n} = 0 \qquad \text{at lateral and bottom surfaces} \tag{4.40b}$$
$$\frac{\partial p}{\partial x_1} = -\rho u_0(t) \qquad \text{at } x_1 = 0 \tag{4.40c}$$

and a radiation condition for $x_1 \to \infty$, where $\partial/\partial n$ is the normal derivative at a surface. The response of the system is calculated as the force at $x_1 = 0$:

$$\mathrm{F}(t) = \int_{\{x_1=0\}} p(x_1 = 0, t)\,\mathrm{d}x_2\mathrm{d}x_3 \tag{4.41}$$

This semi-infinite channel is modelled using the bounded-domain-PML model shown in Fig. 3.4b, composed of a bounded domain Ω_{BD} and a PML Ω_{PM}, with the attenuation functions in Eq. (4.2) chosen as $f^{\mathrm{e}}_1 = f^{\mathrm{p}}_1 = f$, where f is linear in the PML, and $f^{\mathrm{e}}_2 = f^{\mathrm{p}}_2 = 0$, $f^{\mathrm{e}}_3 = f^{\mathrm{p}}_3 = 0$. For comparison, the layer is also modelled using viscous dashpots [16], with consistent dashpots placed at the edge $x_1 = L + L_P$, and the entire domain $\Omega_{\mathrm{BD}} \cup \Omega_{\mathrm{PM}}$ taken to be acoustic. A uniform finite-element mesh of eight-node trilinear isoparametric elements is used to discretise the entire bounded domain for either model, with 20 elements across and along the depth of the channel, and 20 elements per unit length in the x_1 direction.

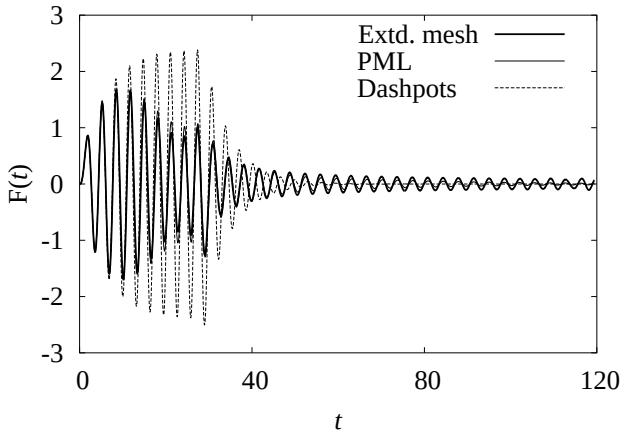

Figure 4.3. Transient force due to dynamic pressure in three-dimensional waveguide, computed using a PML model as well as a viscous dashpot model; $L = d/2$, $L_P = d$, $f_1(x_1) = 10\langle x_1 - L\rangle/L_P$; $\kappa = 1$, $\rho = 1$; $t_d = 30$, $\omega_f = 2$.

Figure 4.3 show the transient modal force due to the pressure in the waveguide [Eq. (4.41)], computed using the PML model and the viscous dashpot model, against results from an extended-mesh model used as a benchmark; this extended-mesh model is a viscous-dashpot model of depth d and length $40d$. Based on a comparison of the frequency-domain responses of the PML and the viscous dashpot models, the values of ω_f were chosen as the excitation frequencies where the two responses are significantly different. The results from the PML model follow the extended-mesh results closely, even though the domain is small enough that the viscous-dashpot boundary generates spurious reflections, manifested in the higher response amplitudes. Moreover, these accurate results from the PML model are obtained at a low computational cost: the cost of the PML model is observed to be approximately 1.6 times that of the dashpot model, which itself is extremely inexpensive.

Figure 4.4 demonstrates the adequacy of the time-domain stretching functions by comparing the harmonic force due to the pressure in the waveguide [Eq. (3.28)] obtained from frequency-domain PML models using two different stretching functions. It is seen that the time-domain stretching function [Eq. (4.2)] produces results — denoted by "PML" — that match results from the frequency-domain-only stretching function [Eq. (3.26)], denoted by "FD PML", for $a_0 \lessapprox 7$ but show slight inaccuracies for higher frequencies.

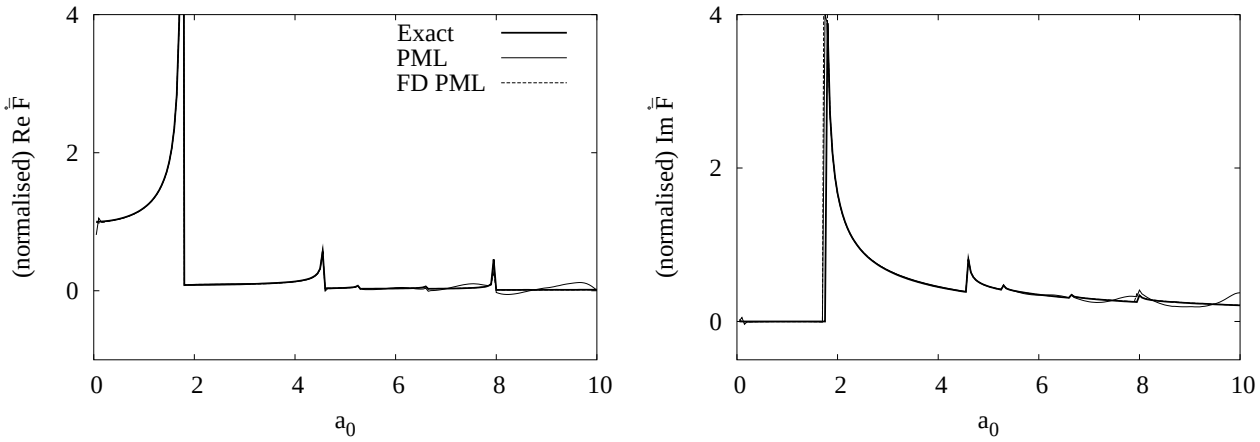

Figure 4.4. Harmonic force due to dynamic pressure in three-dimensional waveguide, computed using PML models with two different forms of the stretching function: "PML" from a stretching function that can be implemented in the time domain, and "FD PML" from a stretching function that is more accurate but is only suitable for the frequency domain; normalised against its value at $a_0 = 0$; $L = d/2$, $L_P = d$, $f_1(x_1) = 10\langle x_1 - L\rangle/L_P$; $\kappa = 1$, $\rho = 1$; $\langle x\rangle := (x + |x|)/2$.

5 TIME-HARMONIC ELASTIC WAVES

5.1 Introduction

This chapter uses the groundwork laid by the previous chapters to develop the PML model — and its finite-element implementation — for time-harmonic elastic waves.

5.2 Elastic medium

Consider a homogeneous isotropic elastic medium undergoing motion in the absence of body forces. The displacements $\boldsymbol{u}(\boldsymbol{x}, t)$ of such a medium are governed by the following equations:

$$\sum_j \frac{\partial \sigma_{ij}}{\partial x_j} = \rho \ddot{u}_i \tag{5.1a}$$

$$\sigma_{ij} = \sum_{k,l} \mathrm{C}_{ijkl}\, \varepsilon_{kl} \tag{5.1b}$$

$$\varepsilon_{ij} = \frac{1}{2}\left[\frac{\partial u_i}{\partial x_j} + \frac{\partial u_j}{\partial x_i}\right] \tag{5.1c}$$

where C_{ijkl} written in terms of the Kronecker delta δ_{ij} is

$$\mathrm{C}_{ijkl} = \left(\kappa - \frac{2}{3}\mu\right)\delta_{ij}\delta_{kl} + \mu\left(\delta_{ik}\delta_{jl} + \delta_{il}\delta_{jk}\right) \tag{5.2}$$

σ_{ij} and ε_{ij} are the components of $\boldsymbol{\sigma}$ and $\boldsymbol{\varepsilon}$, the stress and infinitesimal strain tensors, C_{ijkl} are the components of $\mathbf{C}$, the material stiffness tensor; the indices i, j, k, l range over the spatial dimensions of the problem; κ is the bulk modulus, μ the shear modulus, and ρ the mass density of the medium. For two-dimensional problems, Eq. (5.1) describes either plane-strain or plane-stress motion, following an appropriate definition of κ.

If the medium is subjected to a time-harmonic excitation (through boundary conditions) then the displacement $\boldsymbol{u}$ is time-harmonic of the form $\boldsymbol{u}(\boldsymbol{x}, t) = \bar{\boldsymbol{u}}(\boldsymbol{x}) \exp(\mathrm{i}\omega t)$, where ω is the frequency

of excitation, with $\bar{\boldsymbol{u}}(\boldsymbol{x})$ governed by the following equation

$$\sum_j \frac{\partial \bar{\sigma}_{ij}}{\partial x_j} = -\omega^2 \rho \bar{u}_i \tag{5.3a}$$

$$\bar{\sigma}_{ij} = \sum_{k,l} \mathrm{C}_{ijkl}\, \bar{\varepsilon}_{kl} \tag{5.3b}$$

$$\bar{\varepsilon}_{ij} = \frac{1}{2}\left[\frac{\partial \bar{u}_i}{\partial x_j} + \frac{\partial \bar{u}_j}{\partial x_i}\right] \tag{5.3c}$$

where $\bar{\sigma}_{ij}$ and $\bar{\varepsilon}_{ij}$ are the harmonic amplitudes of σ_{ij} and ε_{ij}, respectively.

On an unbounded domain, Eq. (5.3) admits body-wave solutions [80] in the form of 1) P waves:

$$\bar{\boldsymbol{u}}(\boldsymbol{x}) = \boldsymbol{q} \exp\left[-\mathrm{i} k_p\, \boldsymbol{x} \cdot \boldsymbol{r}\right] \tag{5.4a}$$

where $k_p = \omega/c_p$, with $c_p = \sqrt{(\kappa + 4\mu/3)/\rho}$ the P-wave speed, $\boldsymbol{r}$ is a unit vector denoting the propagation direction, and $\boldsymbol{q} = \pm \boldsymbol{r}$ the direction of particle motion, and 2) S waves:

$$\bar{\boldsymbol{u}}(\boldsymbol{x}) = \boldsymbol{q} \exp\left[-\mathrm{i} k_s\, \boldsymbol{x} \cdot \boldsymbol{r}\right] \tag{5.4b}$$

where $k_s = \omega/c_s$, with $c_s = \sqrt{\mu/\rho}$ the S-wave speed, and $\boldsymbol{q} \cdot \boldsymbol{r} = 0$. Equation (5.1) also admits interface-guided waves, such as Rayleigh waves and Stoneley waves. Rayleigh waves propagate along a free surface, and Stoneley waves may propagate along the interface of two semi-infinite elastic media. Both types of waves propagate with exponentially-decreasing amplitude in the direction normal to and away from the surface or interface, respectively.

A visco-elastic medium is described by the above equations, but with complex-valued moduli $\kappa^* = \kappa(1 + 2\mathrm{i}\zeta)$ and $\mu^* = \mu(1 + 2\mathrm{i}\zeta)$, with ζ the hysteretic damping ratio, and corresponding complex-valued wave speeds.

5.3 Perfectly matched medium and layer

The summation convention is abandoned in this section.

A PMM for elastodynamic motion is defined to be a medium governed by the following equations:

$$\sum_j \frac{1}{\lambda_j(x_j)} \frac{\partial \bar{\sigma}_{ij}}{\partial x_j} = -\omega^2 \rho \bar{u}_i \tag{5.5a}$$

$$\bar{\sigma}_{ij} = \sum_{k,l} \mathrm{C}_{ijkl}\, \bar{\varepsilon}_{kl} \tag{5.5b}$$

$$\bar{\varepsilon}_{ij} = \frac{1}{2}\left[\frac{1}{\lambda_j(x_j)} \frac{\partial \bar{u}_i}{\partial x_j} + \frac{1}{\lambda_i(x_i)} \frac{\partial \bar{u}_j}{\partial x_i}\right] \tag{5.5c}$$

where λ_i are nowhere-zero, continuous, complex-valued coordinate stretching functions; the constitutive relation Eq. (5.5b) is the same as for the elastic medium. Consequently, for two-dimensional problems, Eq. (5.5) describes either plane-strain or plane-stress motion, following an appropriate definition of κ. A (visco-)elastic medium corresponds to $\lambda_i(x_i) \equiv 1$. Equation (5.5) is defined independently of, but motivated by, the definition of $\tilde{x}_i$ given by Eq. (3.4).

The continuity of λ_i can be used to show that on an unbounded domain, Eq. (5.5) admits solutions of the same form as Eq. (5.4), but with $\boldsymbol{x}$ replaced by $\tilde{\boldsymbol{x}}$. A P-type wave solution is of the form

$$\bar{\boldsymbol{u}}(\boldsymbol{x}) = \boldsymbol{q} \exp\left[-\mathrm{i}k_p\, \tilde{\boldsymbol{x}} \cdot \boldsymbol{r}\right] \tag{5.6a}$$

with $\boldsymbol{q} = \pm\boldsymbol{r}$, and an S-type wave solution is of the form

$$\bar{\boldsymbol{u}}(\boldsymbol{x}) = \boldsymbol{q} \exp\left[-\mathrm{i}k_s\, \tilde{\boldsymbol{x}} \cdot \boldsymbol{r}\right] \tag{5.6b}$$

with $\boldsymbol{q} \cdot \boldsymbol{r} = 0$. It can be argued that for appropriately defined λ_i and appropriate boundary conditions, Eq. (5.5) also admits solutions of the forms of Rayleigh and Stoneley waves.

These PMMs exhibit the perfect matching property: if two PMMs with different λ_i are placed adjacent to each other, with the functions λ_i such that they match at the interface of the two media, then any propagating waveform will pass through the interface without generating any reflected wave. The argument for this claim is the same as that for PMMs for acoustic waves.

A choice of λ_i of the form in Eq. (3.8), but with k_s replacing k, leads to attenuated solutions of the form

$$\bar{\boldsymbol{u}}(\boldsymbol{x}) = \exp\left[-\frac{c_s}{c_p}\sum_i F_i(x_i) r_i\right] \boldsymbol{q} \exp\left[-\mathrm{i}k_p\, \boldsymbol{x} \cdot \boldsymbol{r}\right] \tag{5.7a}$$

for P-type waves and

$$\bar{\boldsymbol{u}}(\boldsymbol{x}) = \exp\left[-\sum_i F_i(x_i) r_i\right] \boldsymbol{q} \exp\left[-\mathrm{i}k_s\, \boldsymbol{x} \cdot \boldsymbol{r}\right] \tag{5.7b}$$

for S-type waves if $F_i(x_i) > 0$ and $r_i > 0$, with F_i defined in Eq. (3.10); the attenuation is independent of the frequency if r_i is. It can be argued that suitable choices of λ_i lead to Rayleigh-type (and Stoneley-type) wave solutions that are attenuated in the direction of their propagation.

The absorptive and attenuative properties of the PMM can be used to define an absorbing layer — the PML — adjacent to a bounded domain, e.g., as shown in Fig. 3.1b. The argument for this claim is as for acoustic waves.

The absorptive capability of such a layer is analysed by studying the reflection of plane waves from the fixed boundary. Consider plane-strain motion in the domain shown in Fig. 3.1b, with Ω_{BD} governed by Eq. (5.3) and Ω_{PM} governed by Eq. (5.5), with λ_1 of the form in Eq. (3.8), satisfying $f_1(0) = 0$, and $\lambda_2 \equiv 1$. Furthermore, consider a P-wave with unit amplitude as it enters

the PML at an angle of incidence θ. The incident wave will be reflected from the boundary as a P-type wave and an S-type wave, with the total wave motion represented as

$$\begin{aligned}\bar{\boldsymbol{u}}(\boldsymbol{x}) = \boldsymbol{q}_p^{(I)} \exp\left[-\mathrm{i}k_p\, \tilde{\boldsymbol{x}} \cdot \boldsymbol{r}_p^{(I)}\right] \\ + \; R_{pp}\boldsymbol{q}_p^{(R)} \exp\left[-\mathrm{i}k_p\, \tilde{\boldsymbol{x}} \cdot \boldsymbol{r}_p^{(R)}\right] \; + \; R_{sp}\boldsymbol{q}_s^{(R)} \exp\left[-\mathrm{i}k_s\, \tilde{\boldsymbol{x}} \cdot \boldsymbol{r}_s^{(R)}\right]\end{aligned} \tag{5.8}$$

where the s and p subscripts refer to S-type and P-type waves, respectively, and superscripts (I) and (R) refer to incident and reflected waves, respectively. Imposing $\bar{\boldsymbol{u}}(\boldsymbol{x}) \equiv 0$ for $x_1 = L_P$ and for all x_2, and expressing the directions of propagation and of particle motion in terms of θ, gives

$$|R_{pp}| = \frac{\cos(\theta + \theta_s)}{\cos(\theta - \theta_s)} \exp\left[-2\frac{c_s}{c_p} F_1(L_P) \cos\theta\right] \tag{5.9a}$$

$$|R_{sp}| = \frac{\sin 2\theta}{\cos(\theta - \theta_s)} \exp\left[-F_1(L_P)\left(\frac{c_s}{c_p}\cos\theta + \cos\theta_s\right)\right] \tag{5.9b}$$

with θ_s given by

$$\sin\theta_s = \frac{c_s}{c_p}\sin\theta$$

a similar analysis can be performed to determine the reflection coefficients due to an incident S-type wave. The amplitudes of the reflected P- and S-type waves as they exit the PML, given by $|R_{pp}|$ and $|R_{sp}|$, respectively, are controlled by the choice of parameters f_1 and L_P — independently of the size of the bounded domain to which the PML is adjacent — and are also influenced by the angle of incidence. This suggests that the bounded domain may be restricted to the region of interest in the analysis, thus lowering the computational cost, if the parameters and the orientation of the PML are chosen appropriately.

The above arguments considered a two-dimensional problem only for the sake of illustration; the same reasoning may be extended to three-dimensional problems to reach an identical conclusion.

5.4 Finite-element implementation

A finite-element implementation of this PMM is obtained by expressing the PMM equations in a tensorial form. Consider two rectangular Cartesian coordinate systems for the plane: 1) an $\{x_i\}$ system, with respect to an orthonormal basis $\{\boldsymbol{e}_i\}$, and 2) an $\{x_i'\}$ system, with respect to another orthonormal basis $\{\boldsymbol{e}_i'\}$, with the two bases related by the rotation-of-basis matrix $\mathbf{Q}$, with compo-

nents $Q_{ij} := \boldsymbol{e}_i \cdot \boldsymbol{e}'_j$. Equation (5.5) can be re-written in the basis $\{\boldsymbol{e}'_i\}$ as (no summation)

$$\sum_j \frac{1}{\lambda_j(x'_j)} \frac{\partial \bar{\sigma}'_{ij}}{\partial x'_j} = -\omega^2 \rho \bar{u}'_i \tag{5.10a}$$

$$\bar{\sigma}'_{ij} = \sum_{k,l} \mathrm{C}'_{ijkl}\, \bar{\varepsilon}'_{kl} \tag{5.10b}$$

$$\bar{\varepsilon}'_{ij} = \frac{1}{2}\left[\frac{1}{\lambda_j(x'_j)} \frac{\partial \bar{u}'_i}{\partial x'_j} + \frac{1}{\lambda_i(x'_i)} \frac{\partial \bar{u}'_j}{\partial x'_i} \right] \tag{5.10c}$$

where the various primed quantities represent the components in the basis $\{\boldsymbol{e}'_i\}$ of the corresponding vector or tensor. This represents a PMM where waves are attenuated in the $\boldsymbol{e}'_1$ and $\boldsymbol{e}'_2$ directions. On multiplying Eq. (5.10a) with $\mathcal{J}$, given by [Eq. (3.15)]

$$\mathcal{J} = \begin{cases} \lambda_1(x'_1)\lambda_2(x'_2) & \text{for two-dimensional problems} \\ \lambda_1(x'_1)\lambda_2(x'_2)\lambda_3(x'_3) & \text{for three-dimensional problems} \end{cases}$$

and using the fact that λ_i is a function of x'_i only, Eq. (5.10) can be re-written in matrix notation as

$$\left(\bar{\boldsymbol{\sigma}}' \mathcal{J} \boldsymbol{\Lambda}'\right) \boldsymbol{\nabla}' = -\omega^2 \rho \mathcal{J} \bar{\boldsymbol{u}}' \tag{5.11a}$$

$$\bar{\boldsymbol{\sigma}}' = \mathbf{C}' \bar{\boldsymbol{\varepsilon}}' \tag{5.11b}$$

$$\bar{\boldsymbol{\varepsilon}}' = \frac{1}{2}\left[\left(\bar{\boldsymbol{u}}' \boldsymbol{\nabla}'^T\right) \boldsymbol{\Lambda}' + \boldsymbol{\Lambda}'^T \left(\bar{\boldsymbol{u}}' \boldsymbol{\nabla}'^T\right)^T \right] \tag{5.11c}$$

where

$$\bar{\boldsymbol{\sigma}}' := \left[\bar{\sigma}'_{ij}\right], \quad \bar{\boldsymbol{\varepsilon}} := \left[\bar{\varepsilon}_{ij}\right], \quad \bar{\boldsymbol{u}}' := \left\{\bar{u}'_i\right\}, \quad \boldsymbol{\nabla}' := \left\{\partial / \partial x'_i\right\} \tag{5.12}$$

and $\boldsymbol{\Lambda}'$ is given by [Eq. (3.17)]

$$\boldsymbol{\Lambda}' = \begin{cases} \mathrm{diag}\left(1/\lambda_1(x'_1), 1/\lambda_2(x'_2)\right) & \text{for two-dimensional problems} \\ \mathrm{diag}\left(1/\lambda_1(x'_1), 1/\lambda_2(x'_2), 1/\lambda_3(x'_3)\right) & \text{for three-dimensional problems} \end{cases}$$

Equation (5.11b) is understood in indicial notation. Equation (5.11) can be transformed to the basis $\{\boldsymbol{e}_i\}$ to obtain

$$\left(\bar{\boldsymbol{\sigma}} \mathcal{J} \boldsymbol{\Lambda}\right) \boldsymbol{\nabla} = -\omega^2 \rho \mathcal{J} \bar{\boldsymbol{u}} \tag{5.13a}$$

$$\bar{\boldsymbol{\sigma}} = \mathbf{C} \bar{\boldsymbol{\varepsilon}} \tag{5.13b}$$

$$\bar{\boldsymbol{\varepsilon}} = \frac{1}{2}\left[\left(\bar{\boldsymbol{u}} \boldsymbol{\nabla}^T\right) \boldsymbol{\Lambda} + \boldsymbol{\Lambda}^T \left(\bar{\boldsymbol{u}} \boldsymbol{\nabla}^T\right)^T \right] \tag{5.13c}$$

where the unprimed quantities are obtained from the corresponding primed quantities in Eq. (5.11) via the usual change-of-basis rules for vector and tensor components, e.g., $\boldsymbol{\Lambda}$ is given by Eq. (3.19).

In tensorial notation, Eq. (5.13) becomes

$$\operatorname{div}(\bar{\boldsymbol{\sigma}}\,\jmath\boldsymbol{\Lambda}) = -\omega^2\rho\jmath\bar{\boldsymbol{u}} \tag{5.14a}$$

$$\bar{\boldsymbol{\sigma}} = \mathbf{C}\bar{\boldsymbol{\varepsilon}} \tag{5.14b}$$

$$\bar{\boldsymbol{\varepsilon}} = \frac{1}{2}\left[(\operatorname{grad}\bar{\boldsymbol{u}})\,\boldsymbol{\Lambda} + \boldsymbol{\Lambda}^T\,(\operatorname{grad}\bar{\boldsymbol{u}})^T\right] \tag{5.14c}$$

The weak form of Eq. (5.14a) is derived by taking its inner product with an arbitrary weighting function $\boldsymbol{w}$ residing in an appropriate admissible space, and integrating the resultant scalar over the entire computational domain Ω using integration-by-parts and the divergence theorem to obtain

$$\int_\Omega \tilde{\boldsymbol{\varepsilon}} : \bar{\boldsymbol{\sigma}}\,\jmath\mathrm{d}\Omega - \omega^2\int_\Omega \rho\boldsymbol{w}\cdot\bar{\boldsymbol{u}}\,\jmath\mathrm{d}\Omega = \int_\Gamma \boldsymbol{w}\cdot\bar{\boldsymbol{\sigma}}\,\boldsymbol{\Lambda}\boldsymbol{n}\,\jmath\mathrm{d}\Gamma \tag{5.15}$$

with $\Gamma := \partial\Omega$ the boundary of Ω and $\boldsymbol{n}$ the unit outward normal to it. The symmetry of $\bar{\boldsymbol{\sigma}}$ has been used to obtain the first integral on the left hand side, with

$$\tilde{\boldsymbol{\varepsilon}} = \frac{1}{2}\left[(\operatorname{grad}\boldsymbol{w})\,\boldsymbol{\Lambda} + \boldsymbol{\Lambda}^T\,(\operatorname{grad}\boldsymbol{w})^T\right] \tag{5.16}$$

Assuming element-wise interpolations of $\bar{\boldsymbol{u}}$ and $\boldsymbol{w}$ in terms of shape functions $\boldsymbol{N}$, imposing Eqs. (5.14b) and (5.14c) point-wise in Eq. (5.15), and restricting the integrals to the element domain $\Omega = \Omega^e$ gives the stiffness and mass matrices for a PML element. In terms of nodal submatrices, with I and J the node numbers, these are

$$\mathbf{k}^e_{IJ} = \int_{\Omega^e} \mathbf{B}_I^T\mathbf{D}\mathbf{B}_J\,\jmath\mathrm{d}\Omega \tag{5.17a}$$

$$\mathbf{m}^e_{IJ} = \int_{\Omega^e} \rho N_I N_J\,\jmath\mathrm{d}\Omega\,\mathbf{I} \tag{5.17b}$$

where $\mathbf{I}$ is the identity matrix of the order of the spatial dimension of the problem, and

$$\mathbf{D} := \begin{bmatrix} \kappa+4\mu/3 & \kappa-2\mu/3 & \cdot \\ \kappa-2\mu/3 & \kappa+4\mu/3 & \cdot \\ \cdot & \cdot & \mu \end{bmatrix}, \quad \mathbf{B}_I := \begin{bmatrix} N_{I1} & \cdot \\ \cdot & N_{I2} \\ N_{I2} & N_{I1} \end{bmatrix} \tag{5.18a}$$

for two-dimensional problems, while

$$\mathbf{D} := \begin{bmatrix} \kappa+4\mu/3 & \kappa-2\mu/3 & \kappa-2\mu/3 & \cdot & \cdot & \cdot \\ \kappa-2\mu/3 & \kappa+4\mu/3 & \kappa-2\mu/3 & \cdot & \cdot & \cdot \\ \kappa-2\mu/3 & \kappa-2\mu/3 & \kappa+4\mu/3 & \cdot & \cdot & \cdot \\ \cdot & \cdot & \cdot & \mu & \cdot & \cdot \\ \cdot & \cdot & \cdot & \cdot & \mu & \cdot \\ \cdot & \cdot & \cdot & \cdot & \cdot & \mu \end{bmatrix}, \quad \mathbf{B}_I := \begin{bmatrix} N_{I1} & \cdot & \cdot \\ \cdot & N_{I2} & \cdot \\ \cdot & \cdot & N_{I3} \\ N_{I2} & N_{I1} & \cdot \\ N_{I3} & \cdot & N_{I1} \\ \cdot & N_{I3} & N_{I2} \end{bmatrix} \tag{5.18b}$$

for three-dimensional problems, with

$$N_{Ii} := \Lambda_{ij} N_{I,j} \tag{5.19}$$

In Eq. (5.17), the functions λ_i in $\mathbf{B}$ and in $\mathcal{J}$ are defined globally on the computational domain, not element-wise. The right hand side in Eq. (5.15) can be ignored by assuming that the traction-like term $\boldsymbol{\sigma\Lambda n} = \boldsymbol{0}$ on a free boundary of the PMM. Note that these system matrices for the PMM could also have been obtained by applying coordinate-stretching to the corresponding matrices for the elastic medium.

The FE matrices in Eq. (5.17) are symmetric, but intrinsically complex-valued and frequency-dependent. Hence, the system matrices for Ω will be complex, symmetric, and sparse, the PML contributions to will have to recomputed for each frequency.

5.5 Numerical results

5.5.1 Two-dimensional problems

Numerical results are presented for the classical soil-structure interaction problems of a rigid strip-footing on a i) half-plane, ii) layer on a half-plane, and iii) layer on a rigid base.

Figure 5.1a shows a cross section of a rigid strip-footing of half-width b with its three degrees-of-freedom (DOFs) identified — vertical (V), horizontal (H), and rocking (R) — supported by a homogeneous isotropic (visco-)elastic half-plane with shear modulus μ, mass density ρ, Poisson's ratio ν, and hysteretic damping ratio ζ for the visco-elastic medium. Let $\bar{P}_i$ and $\bar{\Delta}_i$, $i \in \{V, H, R\}$, denote the amplitudes of the harmonic force and of the harmonic displacement, respectively, along the i-th DOF. The two are related through the dynamic flexibility matrix $\mathbf{F}^{\infty}(a_0)$ ($a_0 = \omega b/c_s$) as follows:

$$\begin{Bmatrix} \bar{\Delta}_V \\ \bar{\Delta}_H \\ b\bar{\Delta}_R \end{Bmatrix} = \mathbf{F}^{\infty}(a_0) \begin{Bmatrix} \bar{P}_V \\ \bar{P}_H \\ \bar{P}_R/b \end{Bmatrix} = \begin{bmatrix} F_{VV}(a_0) & 0 & 0 \\ 0 & F_{HH}(a_0) & F_{HR}(a_0) \\ 0 & F_{RH}(a_0) & F_{RR}(a_0) \end{bmatrix} \begin{Bmatrix} \bar{P}_V \\ \bar{P}_H \\ \bar{P}_R/b \end{Bmatrix}. \tag{5.20}$$

This unbounded-domain system is modelled using the bounded-domain-PML model shown in Fig. 5.1b, composed of a bounded domain Ω_{BD} and a PML Ω_{PM}. The stretching functions λ_i are chosen as in Eq. (3.26), with the attenuation functions chosen to be linear in the PML, following Sec. 2.6. Note that the choice of attenuation functions, especially in the corner regions, follows naturally from the requirements that $f_i \equiv 0$ in Ω_{BD}, f_i be a function of x_i only, and that f_i be continuous in the entire computational domain. A finite-element mesh of rectangular four-node bilinear isoparametric elements are used to discretise the entire bounded domain. The mesh is chosen to be adequately dense for the range of frequencies considered, and is graded to capture adequately sharp variations in stresses near the footing. For purposes of comparison, the half-space is also modelled using a viscous-dashpot model [15], wherein the entire domain $\Omega_{\mathrm{BD}} \cup \Omega_{\mathrm{PM}}$ is taken

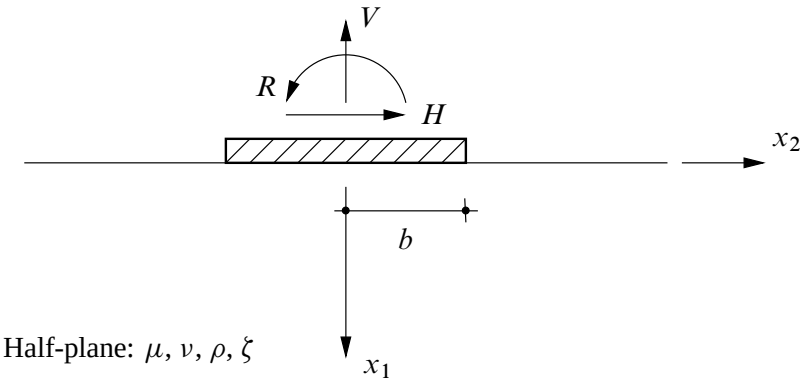

(a)

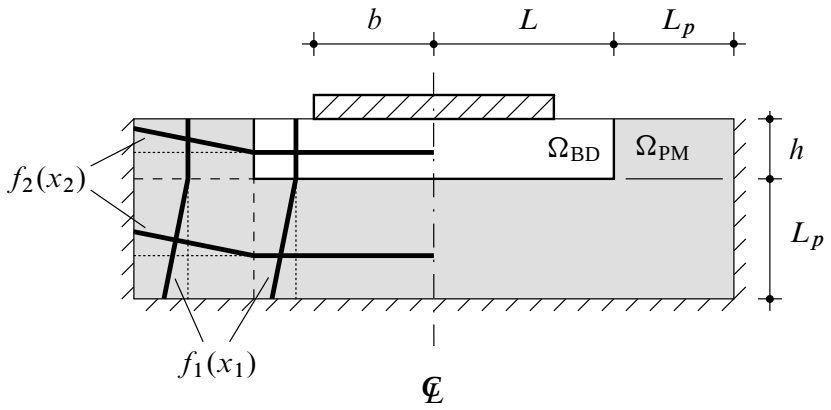

(b)

Figure 5.1. (a) Cross-section of a rigid strip of half-width b on a homogeneous isotropic (visco-)elastic half-plane; (b) a PML model.

to be (visco-)elastic and consistent viscous-dashpot elements replace the fixed outer boundary. The mesh used for the dashpot model is thus comparable to that used for the PML model.

Figure 5.2 presents the dynamic flexibility coefficients computed for an elastic medium from the PML model and from the viscous-dashpot model, against "exact" analytical results [81]. The domain size parameters are chosen to be $L = 3b/2$, $h = b/2$, $L_P = b$. Note that the bounded domain chosen is small, extending only upto $b/2$ on either side of the footing and below it, and the PML width equal to b, the half-width of the footing. Using this small domain, the results obtained from the PML model are highly accurate, even though they are obtained at a low computational cost: the cost of the PML model is similar to that of the dashpot model. The gross inaccuracy of the results from the dashpot model emphasizes the small size of the computational domain. Figure 5.3

compares results for a visco-elastic medium with $\zeta = 0.05$, computed for the same meshes used for the elastic medium, with "exact" semi-analytical results [82]. The results from the PML model are highly accurate, even though the domain is too small for the dashpot model to produce accurate results for this visco-elastic medium.

Figure 5.4a shows a cross section of the rigid strip supported by a visco-elastic layer on a half-plane, and Fig. 5.4b shows a corresponding PML model where λ_i are of the form in Eq. (3.26) with linear attenuation functions in the PMLs. The moduli for the PMLs employed for the layer and the half-plane are set to the moduli for the corresponding elastic media. For comparison, a viscous-dashpot model is also employed, where the entire bounded domain is taken to be visco-elastic, and consistent dashpots replace the fixed outer boundary. Figure 5.5 compares results from the PML model and from the dashpot model against semi-analytical results [83, 84]. The results from the PML model are reasonably accurate, even though the computational domain is small and the cost is comparable to that of the dashpot model. The smallness of the domain is evident in the inaccuracy of results from the dashpot model, especially for vertical and for horizontal motion.

Figure 5.6a shows a cross section of the rigid strip supported by a visco-elastic layer on a rigid base, and Fig. 5.6b shows a corresponding PML model where λ_i are of the form in Eq. (3.26) with $f_1(x_1) = 0$ and $f_2(x_2)$ linear in the PML. Figure 5.7 presents results from the PML model and from a comparable viscous-dashpot model against semi-analytical results [83, 84]. The PML model produces reasonably accurate results at a cost comparable to that of the dashpot model. The boundedness of the domain in the horizontal direction is made prominent by the gross inaccuracy of results for F_{HH} as computed from the dashpot model. Notably, accurate PML results are obtained for this waveguide system with significant evanescent modes. Thus, the stretching function of Eq. (3.26) is adequate for these evanescent modes, but with $f_i(L_P) = 20$, rather than the value of 10 used for other examples in this section; a value of $f_i(L_P) = 10$ for this problem produces results that are slightly less accurate.

5.5.2 Three-dimensional problems

A numerical evaluation of the three-dimensional time-harmonic elastic PML was considered, similar to that for the two-dimensional problem above, by presenting results for the classical soil-structure interaction problem of a rigid circular footing on a half-space [85–88]. However, such an evaluation proved intractable because no existing efficient equation solvers were found for directly solving the large complex, symmetric system of equations that arise from the PML model. Consequently, the three-dimensional PML model is presented above serves only as a record of the formulation, to be used to solve three-dimensional problems at such a time when efficient solvers are readily available. It should be noted that this formulation has been used to succesfully analyse MEMS systems [89], but that required the in-house development of special reduced-model solvers.

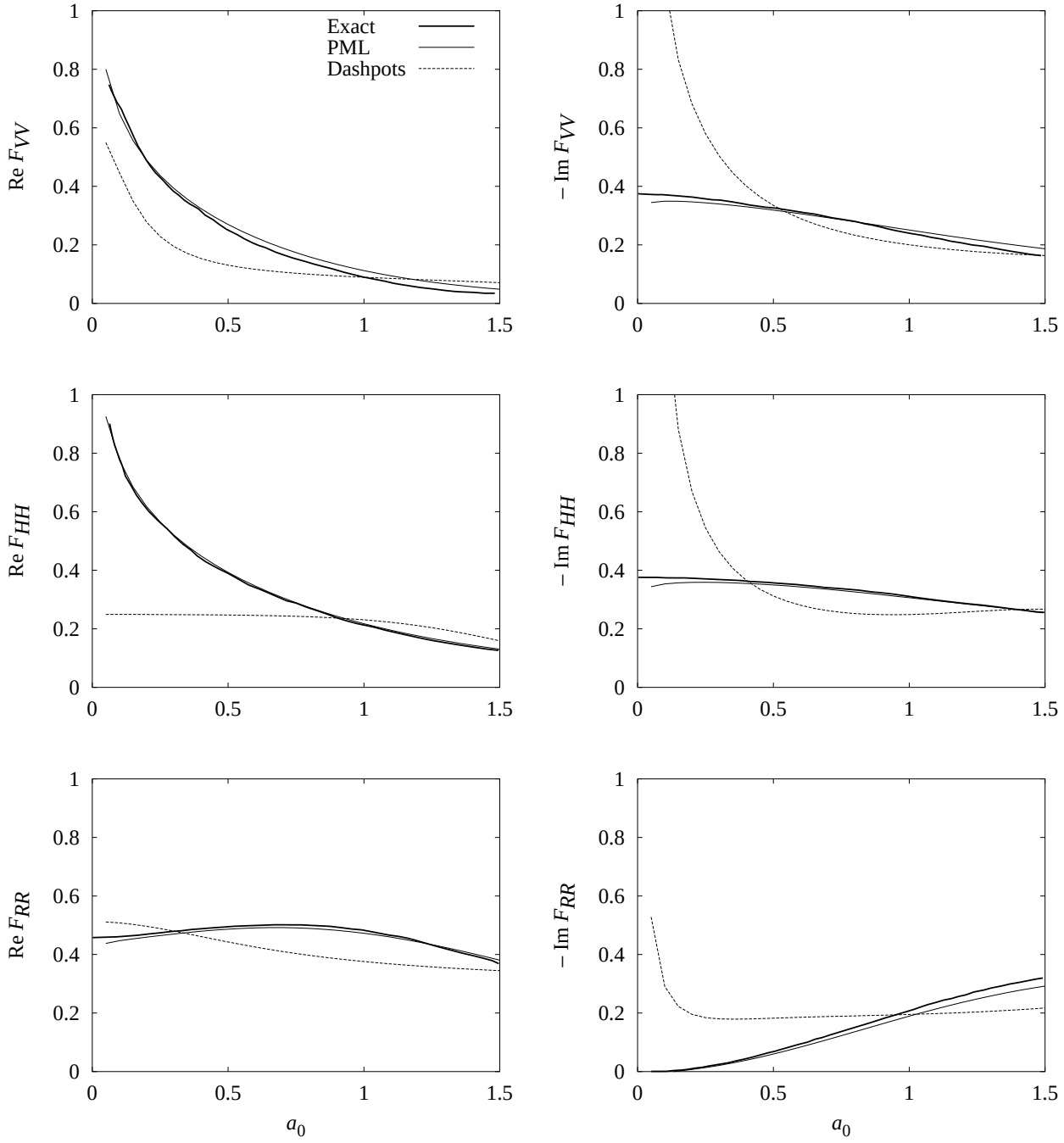

Figure 5.2. Dynamic flexibility coefficients of rigid strip on elastic half-plane computed using a PML model as well as a viscous dashpot boundary model; $L = 3b/2$, $h = b/2$, $L_P = b$, $f_1(x_1) = 10\langle x_1 - h\rangle/L_P$, $f_2(x_2) = 10\langle |x_2| - L\rangle/L_P$; $\langle x\rangle := (x + |x|)/2$; $\mu = 1$, $\nu = 0.25$ ($\kappa = 1.67$).

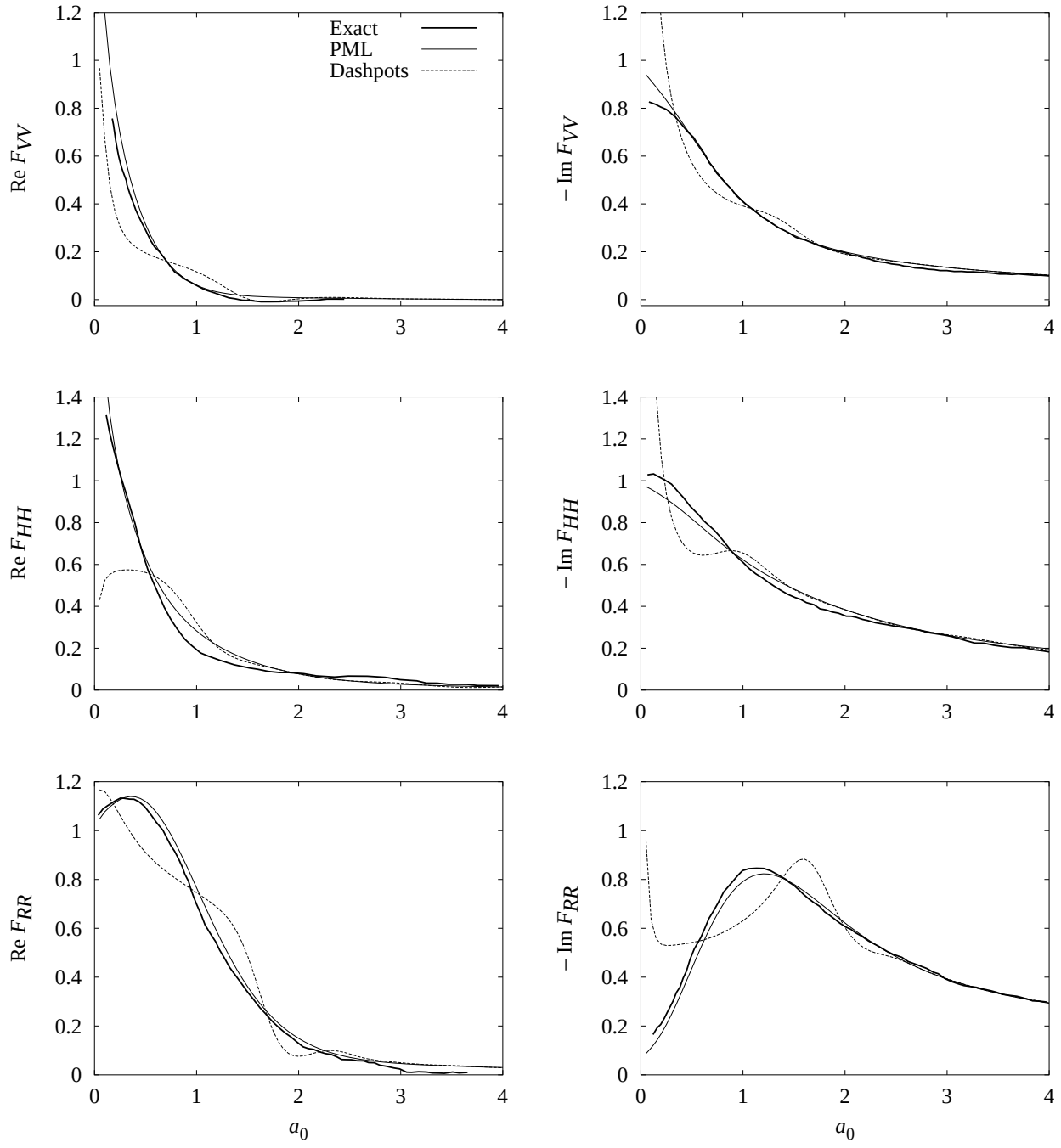

Figure 5.3. Dynamic flexibility coefficients of rigid strip on visco-elastic half-plane computed using a PML model as well as a viscous dashpot boundary model; $L = 3b/2$, $h = b/2$, $L_P = b$, $f_1(x_1) = 10\langle x_1 - h\rangle/L_P$, $f_2(x_2) = 10\langle|x_2| - L\rangle/L_P$; $E = 1$, $\nu = 0.33$ ($\kappa = 0.98$, $\mu = 0.38$), $\zeta = 0.05$, $a_0 = \omega b/\sqrt{E/\rho}$.

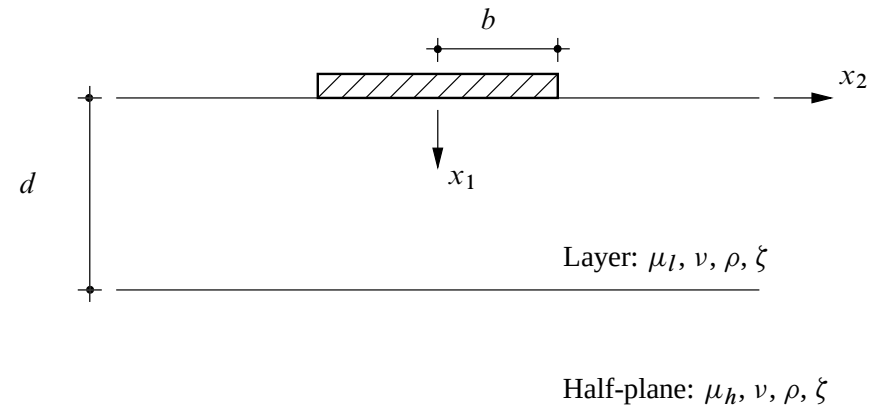

(a)

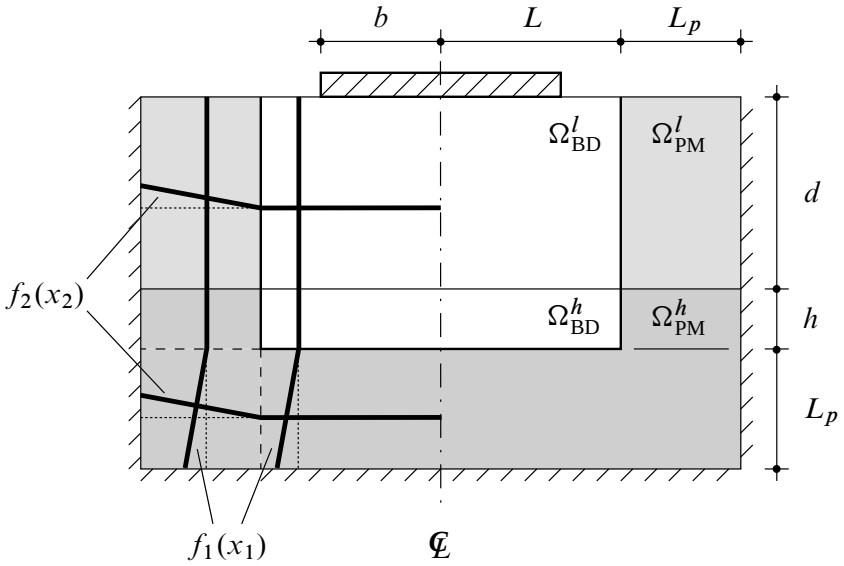

(b)

Figure 5.4. (a) Cross-section of the rigid strip of half-width b on a homogeneous isotropic visco-elastic layer on half-plane; (b) a PML model.

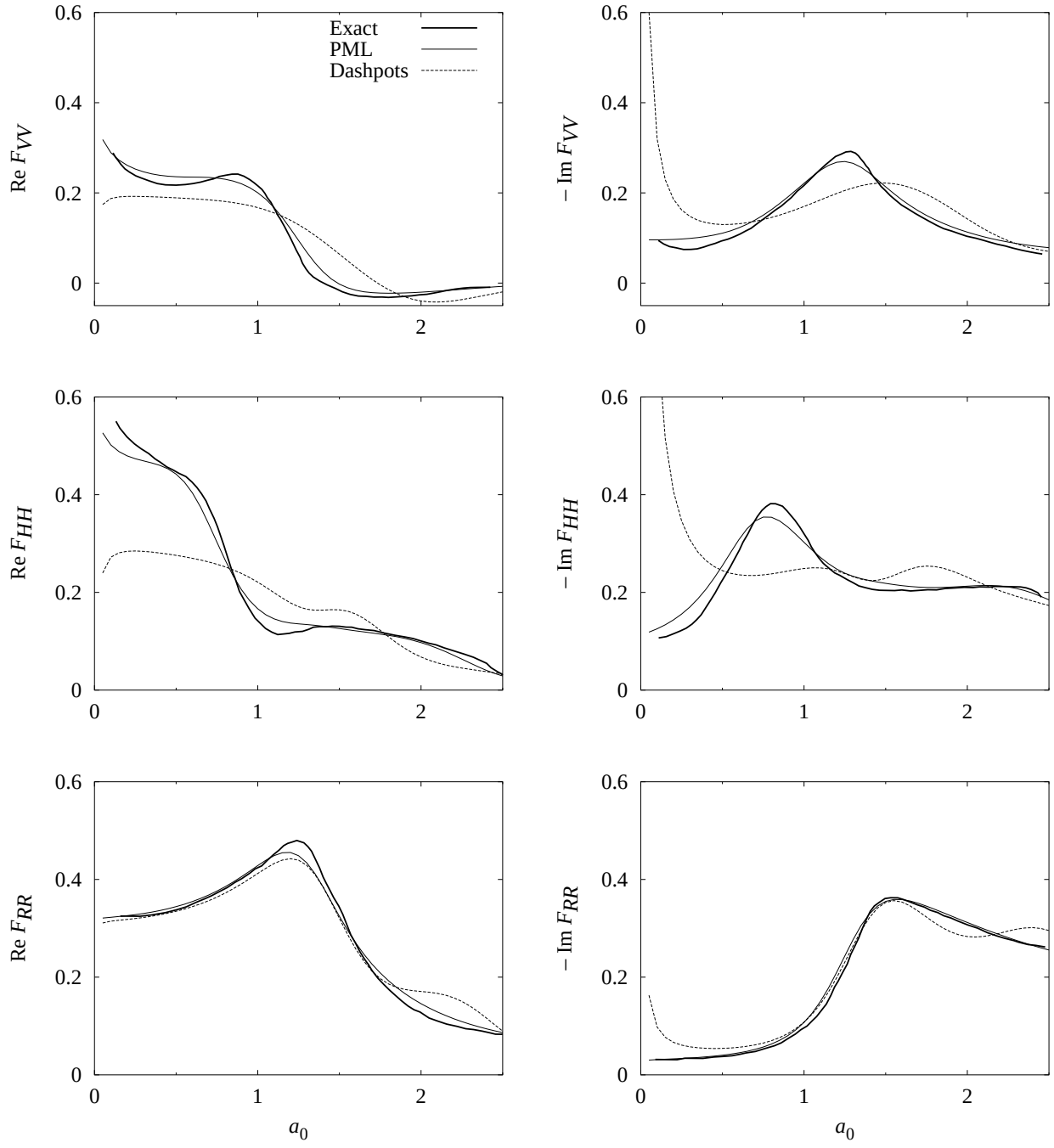

Figure 5.5. Dynamic flexibility coefficients of rigid strip on visco-elastic layer on half-plane computed using a PML model as well as a viscous dashpot boundary model; $L = 3b/2$, $L_P = b$, $h = b/2$, $f_1(x_1) = 10\langle x_1 - (d+h)\rangle/L_P$, $f_2(x_2) = 10\langle |x_2| - L\rangle/L_P$; $d = 2b$, $\mu_h = 4\mu_l$, $\mu_l = 1$, $\nu = 0.4$ ($\kappa_l = 4.67$), $\zeta = 0.05$, $a_0 = \omega b/\sqrt{\mu_l/\rho}$.

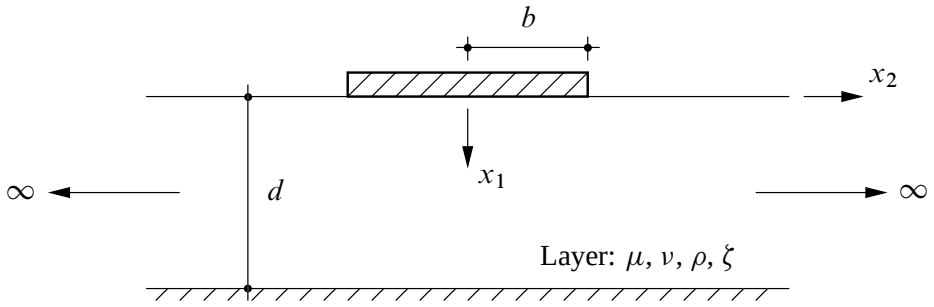

(a)

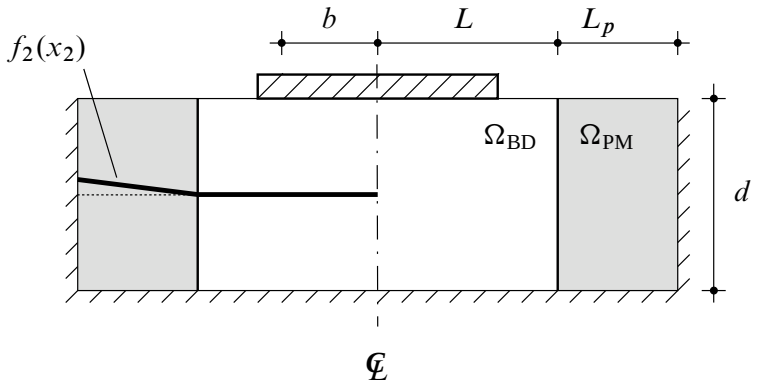

(b)

Figure 5.6. (a) Cross-section of the rigid strip of half-width b on a homogeneous isotropic viscoelastic layer on rigid base; (b) a PML model.

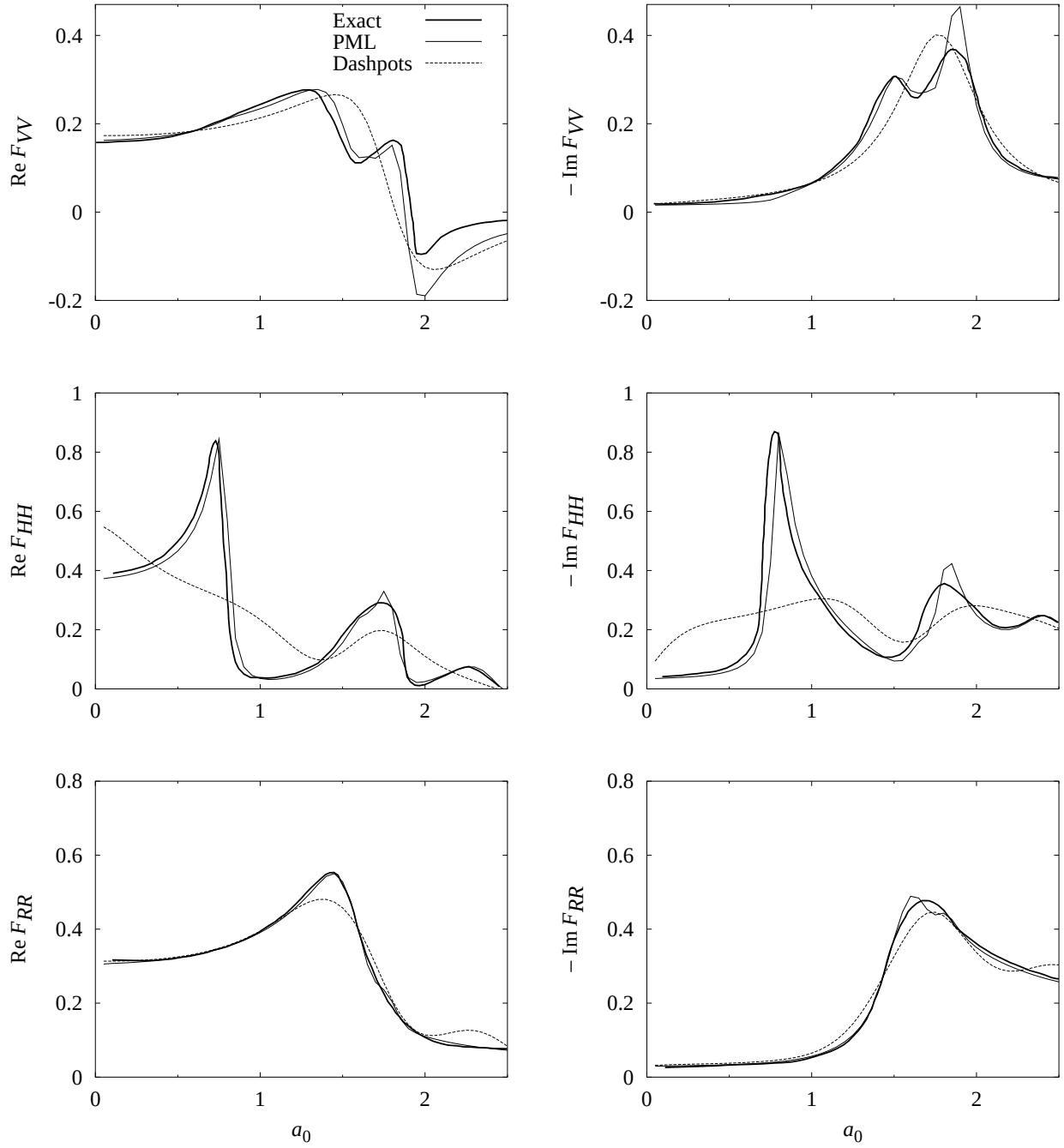

Figure 5.7. Dynamic flexibility coefficients of rigid strip on visco-elastic layer on rigid base computed using a PML model as well as a viscous dashpot boundary model; $L = 3b/2$, $L_P = b$, $f_1(x_1) = 0$, $f_2(x_2) = 20\langle|x_2| - L\rangle/L_P$; $d = 2b$, $\mu = 1$, $\nu = 0.4$ ($\kappa = 4.67$), $\zeta = 0.05$.

6 TRANSIENT ELASTIC WAVES

6.1 Introduction

The previous chapter developed the PML equations for the time-harmonic elastic wave equation, which is obtained by a Fourier transform of the transient elastic wave equation [Eq. (5.1)]. This chapter first develops the PML equations for transient elastic waves by applying the inverse Fourier transform to the time-harmonic elastic PML equations, and then provides a finite-element implementation of these equations.

Recall that, for both two- and three-dimensional problems, the equations for the time-harmonic elastic PML are [cf. Eq. (5.14)]:

$$\operatorname{div}(\bar{\boldsymbol{\sigma}}\jmath\boldsymbol{\Lambda}) = -\omega^2\rho\jmath\bar{\boldsymbol{u}} \tag{6.1a}$$

$$\bar{\boldsymbol{\sigma}} = (1 + 2\mathrm{i}a_0\zeta)\mathbf{C}\bar{\boldsymbol{\varepsilon}} \tag{6.1b}$$

$$\bar{\boldsymbol{\varepsilon}} = \frac{1}{2}\left[(\operatorname{grad}\bar{\boldsymbol{u}})\,\boldsymbol{\Lambda} + \boldsymbol{\Lambda}^T\,(\operatorname{grad}\bar{\boldsymbol{u}})^T\right] \tag{6.1c}$$

where the specific definitions of $\boldsymbol{\Lambda}$ [Eqs. (3.19), (3.17)] and $\jmath$ [Eq. (3.15)] distinguish between the two classes of problems. Equation (6.1) explicitly incorporates Voigt material damping through the correspondence principle in terms of a damping ratio ζ and a non-dimensional frequency $a_0 = k_s b$, where b is a characteristic length of the physical problem. This damping model is chosen over the traditional hysteretic damping model because the latter is non-causal [90]; implementation of a causal hysteretic model in a PML formulation is beyond the scope of this report.

Choosing the stretching functions to be of the form in Eq. (4.2), with a_0 defined as above, allows transformation of Eq. (6.1) into the time domain. However, substituting Eq. (4.2) in Eq. (6.1) through $\boldsymbol{\Lambda}$ and $\jmath$ result in different sets of time-domain equations for two- and three-dimensional problems that are not easily amenable to expression in an unified form in a manner similar to Eq. (6.1) for time-harmonic problems. These two sets of equations are therefore discussed separately in this chapter.

6.2 Two-dimensional problems

6.2.1 Time-domain equations for the PML

Equation (6.1c) is premultiplied by $\mathrm{i}\omega\boldsymbol{\Lambda}^{-T}$ and postmultiplied by $\boldsymbol{\Lambda}^{-1}$, Eqs. (4.2) and (4.3) are substituted into Eq. (6.1), and the inverse Fourier transform is applied to the resultant to obtain the

time-domain equations for the two-dimensional elastic PML:

$$\operatorname{div}\left(\boldsymbol{\sigma}\tilde{\mathbf{F}}^{\mathrm{e}} + \boldsymbol{\Sigma}\tilde{\mathbf{F}}^{\mathrm{p}}\right) = \rho f_{\mathrm{m}}\ddot{\boldsymbol{u}} + \rho\frac{c_s}{b} f_{\mathrm{c}}\dot{\boldsymbol{u}} + \frac{\mu}{b^2} f_{\mathrm{k}}\boldsymbol{u} \tag{6.2a}$$

$$\boldsymbol{\sigma} = \mathbf{C}\left(\boldsymbol{\varepsilon} + \frac{2\zeta b}{c_s}\dot{\boldsymbol{\varepsilon}}\right) \tag{6.2b}$$

$$\begin{aligned}\mathbf{F}^{\mathrm{e}T}\dot{\boldsymbol{\varepsilon}}\mathbf{F}^{\mathrm{e}} + \left(\mathbf{F}^{\mathrm{p}T}\boldsymbol{\varepsilon}\mathbf{F}^{\mathrm{e}} + \mathbf{F}^{\mathrm{e}T}\boldsymbol{\varepsilon}\mathbf{F}^{\mathrm{p}}\right) + \mathbf{F}^{\mathrm{p}T}\mathbf{E}\mathbf{F}^{\mathrm{p}} = \\ \frac{1}{2}\left[\mathbf{F}^{\mathrm{e}T}\left(\operatorname{grad}\dot{\boldsymbol{u}}\right) + \left(\operatorname{grad}\dot{\boldsymbol{u}}\right)^T\mathbf{F}^{\mathrm{e}}\right] + \frac{1}{2}\left[\mathbf{F}^{\mathrm{p}T}\left(\operatorname{grad}\boldsymbol{u}\right) + \left(\operatorname{grad}\boldsymbol{u}\right)^T\mathbf{F}^{\mathrm{p}}\right]\end{aligned} \tag{6.2c}$$

where $\tilde{\mathbf{F}}^{\mathrm{e}}$, $\tilde{\mathbf{F}}^{\mathrm{p}}$, $\mathbf{F}^{\mathrm{e}}$ and $\mathbf{F}^{\mathrm{p}}$ are as in Eqs. (4.4) and (4.5), but with c_s replacing C, f_{m}, f_{c} and f_{k} are as in Eq. (4.8), and

$$\boldsymbol{\Sigma} := \int_0^t \boldsymbol{\sigma}\,\mathrm{d}\tau, \qquad \mathbf{E} := \int_0^t \boldsymbol{\varepsilon}\,\mathrm{d}\tau \tag{6.3}$$

Application of the inverse Fourier transform to obtain $\boldsymbol{\Sigma}$ and $\mathbf{E}$ assumes that $\bar{\boldsymbol{\sigma}}(\omega = 0) = 0$ and $\bar{\boldsymbol{\varepsilon}}(\omega = 0) = 0$.

6.2.2 Finite-element implementation

Equation (6.2) is implemented using a standard displacement-based finite-element approach [71]. The weak form of Eq. (6.2a) is derived by taking its inner product with an arbitrary weighting function $\boldsymbol{w}$ residing in an appropriate admissible space, and then integrating over the entire computational domain Ω using integration-by-parts and the divergence theorem to obtain

$$\begin{aligned}\int_\Omega \rho f_{\mathrm{m}}\boldsymbol{w}\cdot\ddot{\boldsymbol{u}}\,\mathrm{d}\Omega + \int_\Omega \rho\frac{c_s}{b} f_{\mathrm{c}}\boldsymbol{w}\cdot\dot{\boldsymbol{u}}\,\mathrm{d}\Omega + \int_\Omega \frac{\mu}{b^2} f_{\mathrm{k}}\boldsymbol{w}\cdot\boldsymbol{u}\,\mathrm{d}\Omega \\ + \int_\Omega \tilde{\boldsymbol{\varepsilon}}^{\mathrm{e}} : \boldsymbol{\sigma}\,\mathrm{d}\Omega + \int_\Omega \tilde{\boldsymbol{\varepsilon}}^{\mathrm{p}} : \boldsymbol{\Sigma}\,\mathrm{d}\Omega = \int_\Gamma \boldsymbol{w}\cdot\left(\boldsymbol{\sigma}\tilde{\mathbf{F}}^{\mathrm{e}} + \boldsymbol{\Sigma}\tilde{\mathbf{F}}^{\mathrm{p}}\right)\boldsymbol{n}\,\mathrm{d}\Gamma\end{aligned} \tag{6.4}$$

where $\Gamma := \partial\Omega$ is the boundary of Ω and $\boldsymbol{n}$ is the unit outward normal to Γ. The symmetry of $\boldsymbol{\sigma}$ and $\boldsymbol{\Sigma}$ is used to obtain the last two integrals on the left-hand side, with

$$\tilde{\boldsymbol{\varepsilon}}^{\mathrm{e}} := \frac{1}{2}\left[\left(\operatorname{grad}\boldsymbol{w}\right)\tilde{\mathbf{F}}^{\mathrm{e}} + \tilde{\mathbf{F}}^{\mathrm{e}T}\left(\operatorname{grad}\boldsymbol{w}\right)^T\right], \quad \tilde{\boldsymbol{\varepsilon}}^{\mathrm{p}} := \frac{1}{2}\left[\left(\operatorname{grad}\boldsymbol{w}\right)\tilde{\mathbf{F}}^{\mathrm{p}} + \tilde{\mathbf{F}}^{\mathrm{p}T}\left(\operatorname{grad}\boldsymbol{w}\right)^T\right] \tag{6.5}$$

The weak form is first spatially discretised by interpolating $\boldsymbol{u}$ and $\boldsymbol{w}$ element-wise in terms of nodal quantities using appropriate nodal shape functions. This leads to the system of equations

$$\mathbf{m}\ddot{\boldsymbol{d}} + \mathbf{c}\dot{\boldsymbol{d}} + \mathbf{k}\boldsymbol{d} + \boldsymbol{f}_{\mathrm{int}} = \boldsymbol{f}_{\mathrm{ext}} \tag{6.6}$$

where $\mathbf{m}$, $\mathbf{c}$ and $\mathbf{k}$ are the mass, damping and stiffness matrices, respectively, $\boldsymbol{d}$ is a vector of nodal displacements, $\boldsymbol{f}_{\mathrm{int}}$ is a vector of internal force terms, and $\boldsymbol{f}_{\mathrm{ext}}$ is a vector of external forces. The

system matrices are assembled from element-level constituent matrices, given in terms of their IJ-th nodal submatrices as, respectively,

$$\mathbf{m}^e_{IJ} = \int_{\Omega^e} \rho f_{\mathrm{m}} N_I N_J \,\mathrm{d}\Omega \mathbf{I}, \quad \mathbf{c}^e_{IJ} = \int_{\Omega^e} \rho \frac{c_s}{b} f_{\mathrm{c}} N_I N_J \,\mathrm{d}\Omega \mathbf{I}, \quad \mathbf{k}^e_{IJ} = \int_{\Omega^e} \frac{\mu}{b^2} f_{\mathrm{k}} N_I N_J \,\mathrm{d}\Omega \mathbf{I} \tag{6.7a}$$

where N_I is the shape function for node I and $\mathbf{I}$ is the identity matrix of size 2×2. The element-level internal force term is given by

$$\boldsymbol{f}^e = \int_{\Omega^e} \tilde{\mathbf{B}}^{\mathrm{e}T} \hat{\boldsymbol{\sigma}} \,\mathrm{d}\Omega + \int_{\Omega^e} \tilde{\mathbf{B}}^{\mathrm{p}T} \hat{\boldsymbol{\Sigma}} \,\mathrm{d}\Omega \tag{6.7b}$$

where $\tilde{\mathbf{B}}^{\mathrm{e}}$ and $\tilde{\mathbf{B}}^{\mathrm{p}}$ are given in terms of their nodal submatrices as

$$\tilde{\mathbf{B}}^{\mathrm{e}}_I := \begin{bmatrix} \tilde{N}^{\mathrm{e}}_{I1} & \cdot \\ \cdot & \tilde{N}^{\mathrm{e}}_{I2} \\ \tilde{N}^{\mathrm{e}}_{I2} & \tilde{N}^{\mathrm{e}}_{I1} \end{bmatrix}, \quad \tilde{\mathbf{B}}^{\mathrm{p}}_I := \begin{bmatrix} \tilde{N}^{\mathrm{p}}_{I1} & \cdot \\ \cdot & \tilde{N}^{\mathrm{p}}_{I2} \\ \tilde{N}^{\mathrm{p}}_{I2} & \tilde{N}^{\mathrm{p}}_{I1} \end{bmatrix} \tag{6.8}$$

with

$$\tilde{N}^{\mathrm{e}}_{Ii} := \tilde{F}^{\mathrm{e}}_{ij} N_{I,j} \quad \text{and} \quad \tilde{N}^{\mathrm{p}}_{Ii} := \tilde{F}^{\mathrm{p}}_{ij} N_{I,j} \tag{6.9}$$

and

$$\hat{\boldsymbol{\sigma}} := \begin{Bmatrix} \sigma_{11} \\ \sigma_{22} \\ \sigma_{12} \end{Bmatrix} \tag{6.10}$$

with $\hat{\boldsymbol{\Sigma}}$ the time-integral of $\hat{\boldsymbol{\sigma}}$. Note that the above vector representation of the tensor $\boldsymbol{\sigma}$ assumes its symmetry, which requires a minor symmetry of $\mathbf{C}$; because the PML medium is unphysical, a physically-motivated axiom — the balance of angular momentum — cannot be employed to show the symmetry of $\boldsymbol{\sigma}$. The attenuation functions f^{e}_i and f^{p}_i are defined globally on the computational domain, not element-wise. It is conveniently assumed that there is no contribution to $\boldsymbol{f}_{\mathrm{ext}}$ from a free boundary of the PML.

Solution of the equations of motion [Eq. (6.6)] using a time-stepping algorithm requires calculating $\boldsymbol{\sigma}_{n+1}$ and $\boldsymbol{\Sigma}_{n+1}$ at t_{n+1}, to calculate $\boldsymbol{f}^e_{n+1}$, and also a consistent linearisation of $\boldsymbol{f}^e_{n+1}$ at $\boldsymbol{d}_{n+1}$. Towards this, the approximations

$$\dot{\boldsymbol{\varepsilon}}(t_{n+1}) \approx \frac{\boldsymbol{\varepsilon}_{n+1} - \boldsymbol{\varepsilon}_n}{\Delta t}, \qquad \mathbf{E}(t_{n+1}) \approx \mathbf{E}_n + \boldsymbol{\varepsilon}_{n+1} \Delta t \tag{6.11}$$

are used in Eq. (6.2c) to obtain

$$\hat{\boldsymbol{\varepsilon}}_{n+1} = \frac{1}{\Delta t} \left[\mathbf{B}^{\epsilon} \boldsymbol{v}_{n+1} + \mathbf{B}^{\varrho} \boldsymbol{d}_{n+1} + \frac{1}{\Delta t} \hat{\mathbf{F}}^{\epsilon} \hat{\boldsymbol{\varepsilon}}_n - \hat{\mathbf{F}}^{\varrho} \hat{\mathbf{E}}_n \right] \tag{6.12}$$

where $\boldsymbol{v}_{n+1} \approx \dot{\boldsymbol{d}}^e(t_{n+1})$, and

$$\hat{\boldsymbol{\varepsilon}} := \begin{Bmatrix} \varepsilon_{11} \\ \varepsilon_{22} \\ 2\varepsilon_{12} \end{Bmatrix} \tag{6.13}$$

and $\hat{\mathbf{E}}$ is the time-integral of $\hat{\boldsymbol{\varepsilon}}$. The matrices $\mathbf{B}^{\epsilon}$, $\mathbf{B}^{\varrho}$, $\hat{\mathbf{F}}^{\epsilon}$ and $\hat{\mathbf{F}}^{\varrho}$ in Eq. (6.12) are defined in Appendix B.

The use of Eq. (6.11a) in the constitutive equation [Eq. (6.2b)] gives

$$\hat{\boldsymbol{\sigma}}_{n+1} = \left(1 + \frac{2\zeta b}{c_s \Delta t}\right) \mathbf{D}\hat{\boldsymbol{\varepsilon}}_{n+1} - \frac{2\zeta b}{c_s \Delta t}\mathbf{D}\hat{\boldsymbol{\varepsilon}}_n \tag{6.14}$$

where

$$\mathbf{D} := \begin{bmatrix} \kappa + 4\mu/3 & \kappa - 2\mu/3 & \cdot \\ \kappa - 2\mu/3 & \kappa + 4\mu/3 & \cdot \\ \cdot & \cdot & \mu \end{bmatrix} \tag{6.15}$$

Furthermore, $\hat{\boldsymbol{\Sigma}}_{n+1}$ is approximated as

$$\hat{\boldsymbol{\Sigma}}_{n+1} = \hat{\boldsymbol{\Sigma}}_n + \hat{\boldsymbol{\sigma}}_{n+1}\Delta t \tag{6.16}$$

Substituting Eq. (6.16) into Eq. (6.7b) gives

$$\boldsymbol{f}^e_{n+1} = \int_{\Omega^e} \tilde{\mathbf{B}}^T \hat{\boldsymbol{\sigma}}_{n+1}\, \mathrm{d}\Omega + \int_{\Omega^e} \tilde{\mathbf{B}}^{\mathrm{p}T} \hat{\boldsymbol{\Sigma}}_n\, \mathrm{d}\Omega \tag{6.17}$$

where

$$\tilde{\mathbf{B}} := \tilde{\mathbf{B}}^{\mathrm{e}} + \Delta t \tilde{\mathbf{B}}^{\mathrm{p}} \tag{6.18}$$

Linearisation of Eq. (6.17) gives, on using Eq. (6.14) along with Eq. (6.12),

$$\Delta \boldsymbol{f}^e_{n+1} = \left[\int_{\Omega^e} \tilde{\mathbf{B}}^T \tilde{\mathbf{D}} \mathbf{B}^{\epsilon}\, \mathrm{d}\Omega\right] \Delta \boldsymbol{v}_{n+1} + \left[\int_{\Omega^e} \tilde{\mathbf{B}}^T \tilde{\mathbf{D}} \mathbf{B}^{\varrho}\, \mathrm{d}\Omega\right] \Delta \boldsymbol{d}_{n+1} \tag{6.19}$$

where

$$\tilde{\mathbf{D}} = \frac{1}{\Delta t}\left(1 + \frac{2\zeta b}{c_s \Delta t}\right)\mathbf{D} \tag{6.20}$$

i.e., this linearisation gives tangent matrices

$$\check{\mathbf{c}}^e := \int_{\Omega^e} \tilde{\mathbf{B}}^T \tilde{\mathbf{D}} \mathbf{B}^{\epsilon}\, \mathrm{d}\Omega, \qquad \check{\mathbf{k}}^e := \int_{\Omega^e} \tilde{\mathbf{B}}^T \tilde{\mathbf{D}} \mathbf{B}^{\varrho}\, \mathrm{d}\Omega \tag{6.21}$$

which may be incorporated into the effective tangent stiffness used in the time-stepping algorithm. Unfortunately, these matrices are not symmetric. However, since all the system matrices are independent of $\boldsymbol{d}$, this is effectively a linear model. Note that the attenuation functions, representing the coordinate-stretching, affect the various compatibility matrices, e.g., $\tilde{\mathbf{B}}^{\mathrm{e}}$, $\tilde{\mathbf{B}}^{\epsilon}$ etc. but not the material moduli matrix $\mathbf{D}$. Consequently, this FE formulation can be applied to both plane-strain and plane-stress problems by defining κ appropriately.

A skeleton of the algorithm for computing the element-level effective internal force and tangent matrix is given in Box 6.1.

Box 6.1. Computing effective force and stiffness for 2D elastic PML element.

1. Compute system matrices $\mathbf{m}^e$, $\mathbf{c}^e$ and $\mathbf{k}^e$ [Eq. (6.7a)].
2. Compute internal force $\boldsymbol{f}^e_{n+1}$ [Eq. (6.17)].
   Use $\hat{\boldsymbol{\varepsilon}}_{n+1}$ [Eq. (6.12) with Appendix B], and $\hat{\boldsymbol{\sigma}}_{n+1}$ [Eq. (6.14)].
3. Compute tangent matrices $\check{\mathbf{c}}^e$ and $\check{\mathbf{k}}^e$ [Eq. (6.21) with Eq. (6.18)].
4. Compute effective internal force $\tilde{\boldsymbol{f}}^e_{n+1}$ and tangent stiffness $\tilde{\mathbf{k}}^e$:

$$\tilde{\boldsymbol{f}}^e_{n+1} =^e \boldsymbol{a}_{n+1} + \mathbf{c}^e \boldsymbol{v}_{n+1} + \mathbf{k}^e \boldsymbol{d}_{n+1} + \boldsymbol{f}^e_{n+1}$$
$$\tilde{\mathbf{k}}^e = \alpha_{\mathrm{k}} \left(\mathbf{k}^e + \check{\mathbf{k}}^e \right) + \alpha_{\mathrm{c}} \left(\mathbf{c}^e + \check{\mathbf{c}}^e \right) + \alpha^e_{\mathrm{m}}$$

   where $\boldsymbol{a}_{n+1} \approx \ddot{\boldsymbol{d}}^e(t_{n+1})$, and, for example,

$$\alpha_{\mathrm{k}} = 1, \quad \alpha_{\mathrm{c}} = \frac{\gamma}{\beta \Delta t}, \quad \alpha_{\mathrm{m}} = \frac{1}{\beta \Delta t^2}$$

   for the Newmark method.

Note: The tangent stiffness $\tilde{\mathbf{k}}^e$ is independent of the solution, and thus has to be computed only once. However, the internal force $\boldsymbol{f}^e_{n+1}$ has to be re-computed at each time-step because it is dependent on the solution at past times.

6.2.3 Numerical results

Numerical results are presented for the classical soil-structure interaction problems of a rigid strip-footing on a i) half-plane, ii) layer on a half-plane, and iii) layer on a rigid base.

The time-domain response of a rigid strip-footing on a half-plane, shown in Fig. 5.1a, is studied through the reactions along the three DOFs due to an imposed displacement along any of the three DOFs; the imposed displacement is chosen to be of the form of Eq. (A3) and the reaction along DOF i due to an imposed displacement along j is denoted by P_{ij}, with $i, j \in \{V, H, R\}$.

This unbounded-domain system is modelled using the bounded-domain-PML model shown in Fig. 5.1b, composed of a bounded domain Ω_{BD} and a PML Ω_{PM}, with the attenuation functions in Eq. (4.2) chosen as $f_i^{\mathrm{e}} = f_i^{\mathrm{p}} = f_i$, with f_i chosen to be linear in the PML. For comparison, the half-plane is also modelled using a viscous-dashpot model [15], wherein the entire domain $\Omega_{\mathrm{BD}} \cup \Omega_{\mathrm{PM}}$ is taken to be (visco-)elastic and consistent dashpot elements replace the fixed outer boundary. The finite-element meshes chosen for these models are the same as those used for time-harmonic analysis in Sec. 5.5.1. Because of the dearth of analytical results in the time domain, the half-plane is modelled using an extended mesh; the results from this mesh will serve as a benchmark. From the center of the footing, this mesh extends to a distance of $35b$ downwards and laterally; the entire domain is taken to be (visco-)elastic, and viscous dashpots are placed on the outer boundary.

Figure 6.1a compares the reactions computed for an elastic medium using the PML model and the dashpot model with results from the extended mesh. Based on a comparison of the frequency-domain responses of the PML and the viscous dashpot models, the values of ω_f were chosen as the excitation frequencies where the two responses are significantly different. The results obtained from the PML model follow the extended mesh results closely, even though the domain is small enough for the dashpots to reflect waves back to the footing, as manifested in the higher response amplitudes. The computational cost of the PML model is observed to be approximately 1.6 times that of the dashpot model; this cost is not significantly large because the dashpot model itself is computationally inexpensive. Thus, the highly accurate results from the PML model are obtained at low computational cost. Significantly, the cost of the extended-mesh model is observed to be approximately 17 times that of the PML model. Figure 6.1b presents similar comparisons for a visco-elastic half-plane. The PML results are visually indistinguishable from the extended mesh results, even though the computational domain is small: the dashpots generate spurious reflections even when the medium is visco-elastic.

Figures 6.2 and 6.3 present frequency-dependent flexibility coefficients $F_{ij}(a_0)$ for the rigid strip-footing on a half-plane computed using a PML model employing the time-domain stretching functions in Eq. (4.2). The flexibility coefficients are defined as the displacement amplitudes along DOF i due to a unit-amplitude harmonic force along DOF j. Results for the elastic half-plane are compared in Fig. 6.2 against available analytical results [81]. Due to the dearth of analytical solutions for the strip on a Voigt visco-elastic half-plane, the results obtained from the (possibly less accurate) time-domain stretching functions are compared in Fig. 6.3 to results from a PML model employing the frequency-domain-only stretching functions [Eq. (3.26)], denoted by "FD PML" in the figures. The rationale behind this approach is that the frequency-domain stretching functions produce highly accurate results for hysteretic damping (Sec. 5.5.1) and hence can be expected to also produce excellent results for Voigt damping. The results demonstrate that the time-domain stretching functions indeed produce accurate results as expected, because the wave motion in the half-plane consists primarily of propagating modes, which are adequately attenuated even by the time-domain stretching functions.

Figure 5.4a shows a cross section of the rigid strip supported by a layer on a half-plane, and Fig. 5.4b shows a corresponding PML model with the attenuation functions in Eq. (4.2) chosen as $f_i^{\mathrm{e}} = f_i^{\mathrm{p}} = f_i$, with f_i chosen to be linear in the PML. The elastic moduli for the PMLs employed for the layer and the half-plane are set to the moduli for the corresponding elastic media. For comparison, a viscous-dashpot model is also employed, where the entire bounded domain is taken to be (visco-)elastic and consistent dashpots replace the fixed outer boundary. An extended-mesh model, with viscous dashpots at the outer boundary, is taken as a benchmark model for the layer on a half-plane; this mesh extends to a distance of $40b$ laterally and downwards from the center of the footing.

Figure 6.4 shows the reactions of the rigid strip on a layer-on-half-plane due to imposed displacements. The PML results typically follow the results from the extended mesh, even though the domain is small enough for the viscous dashpots to generate spurious reflections. The computational cost of the PML model is not significantly large: it is observed to be approximately 1.5 times

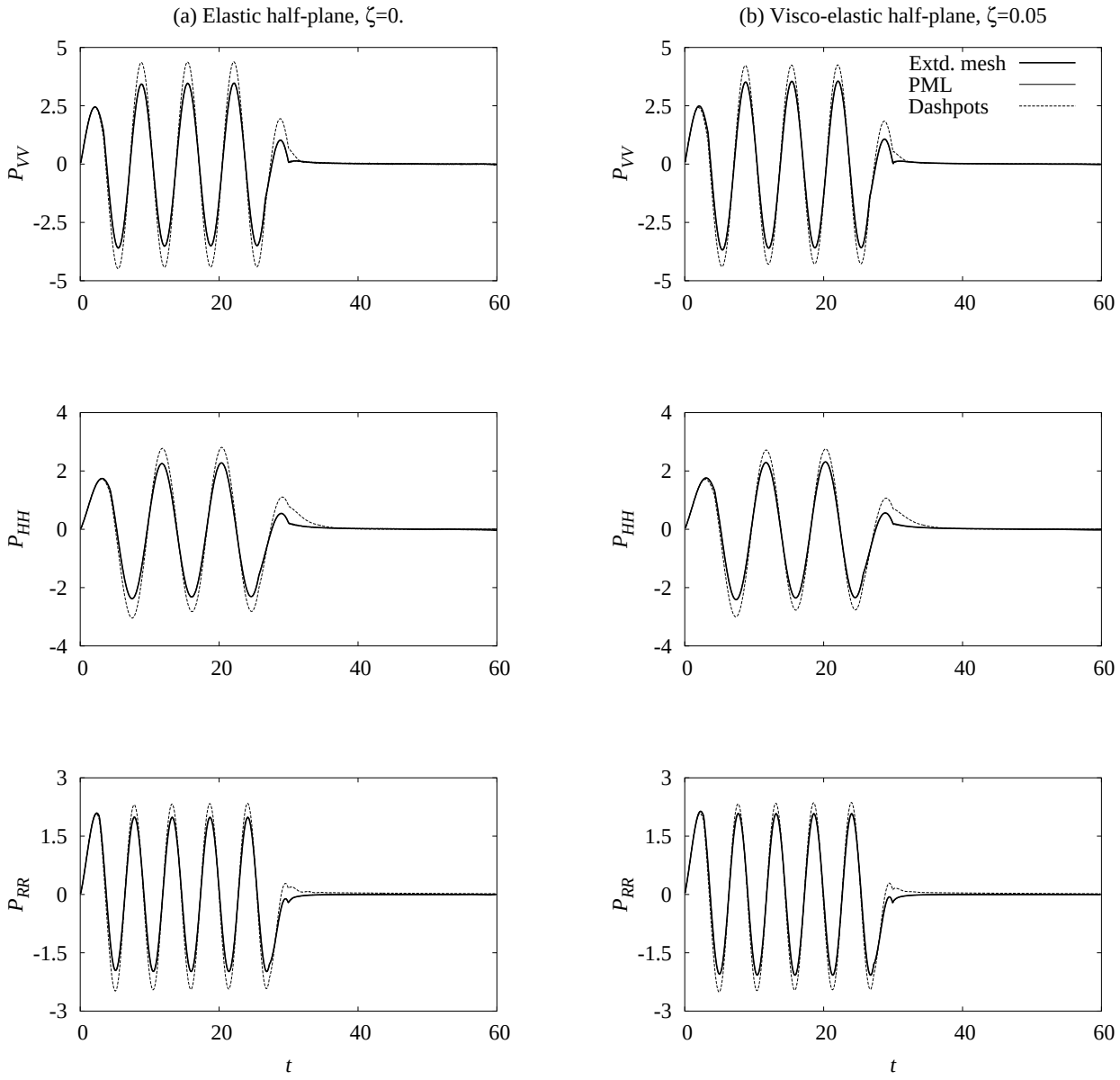

Figure 6.1. Reactions of a rigid strip on (visco-)elastic half-plane due to imposed displacements; $L = 3b/2$, $h = b/2$, $L_P = b$, $f_1(x_1) = 10\langle x_1 - h\rangle/L_P$, $f_2(x_2) = 10\langle|x_2| - L\rangle/L_P$; $\langle x\rangle := (x + |x|)/2$; $\mu = 1$, $\nu = 0.25$ ($\kappa = 1.67$); $t_d = 30$, $\omega_f = 1.00$ for vertical excitation, 0.75 for horizontal excitation, 1.25 for rocking excitation.

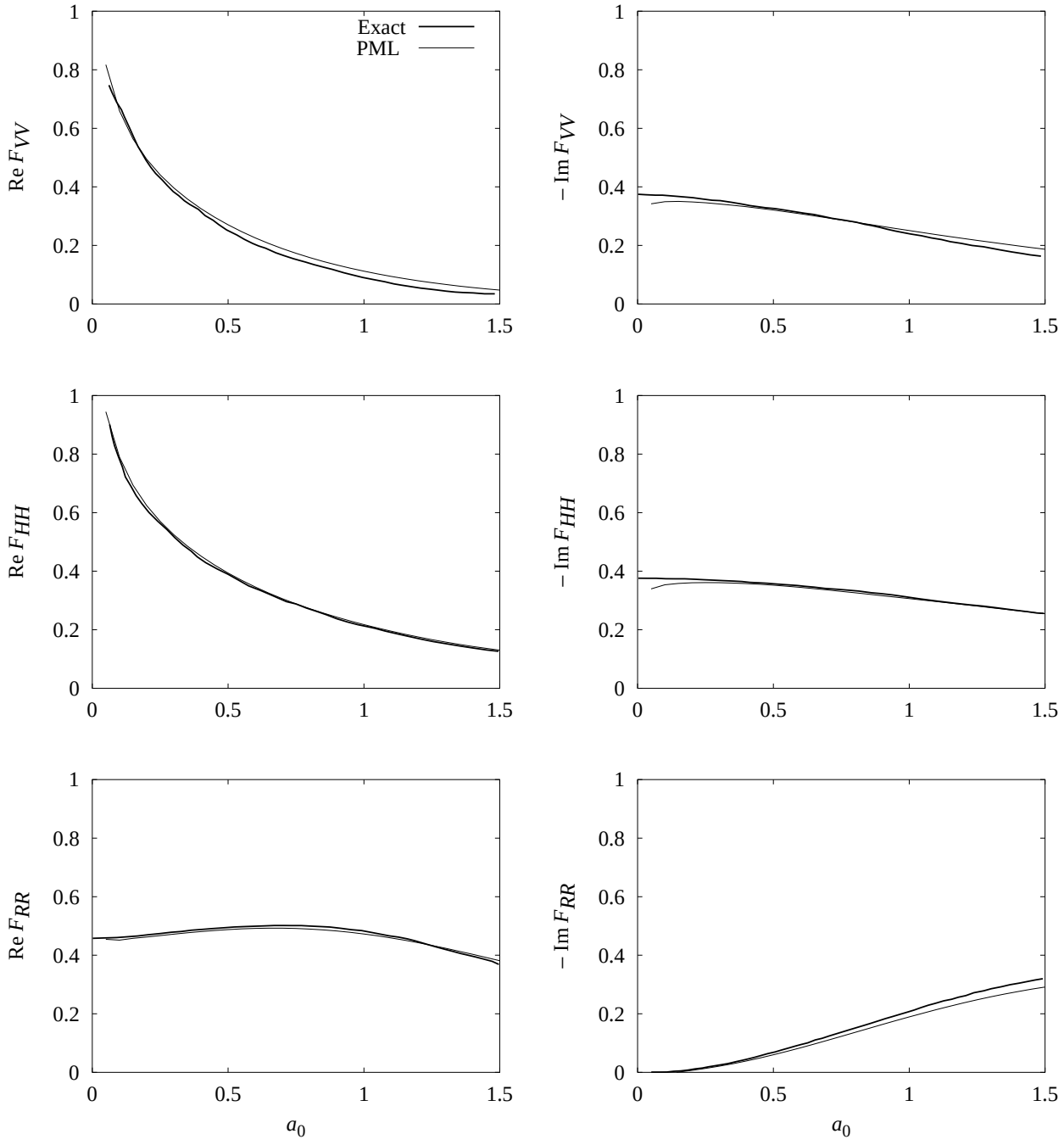

Figure 6.2. Dynamic flexibility coefficients of rigid strip on elastic half-plane computed using a PML model with stretching functions suitable for time-domain analysis; $L = 3b/2$, $h = b/2$, $L_P = b$, $f_1(x_1) = 10\langle x_1 - h\rangle/L_P$, $f_2(x_2) = 10\langle|x_2| - L\rangle/L_P$; $\mu = 1$, $\nu = 0.25$; "Exact" results from Ref. 81.

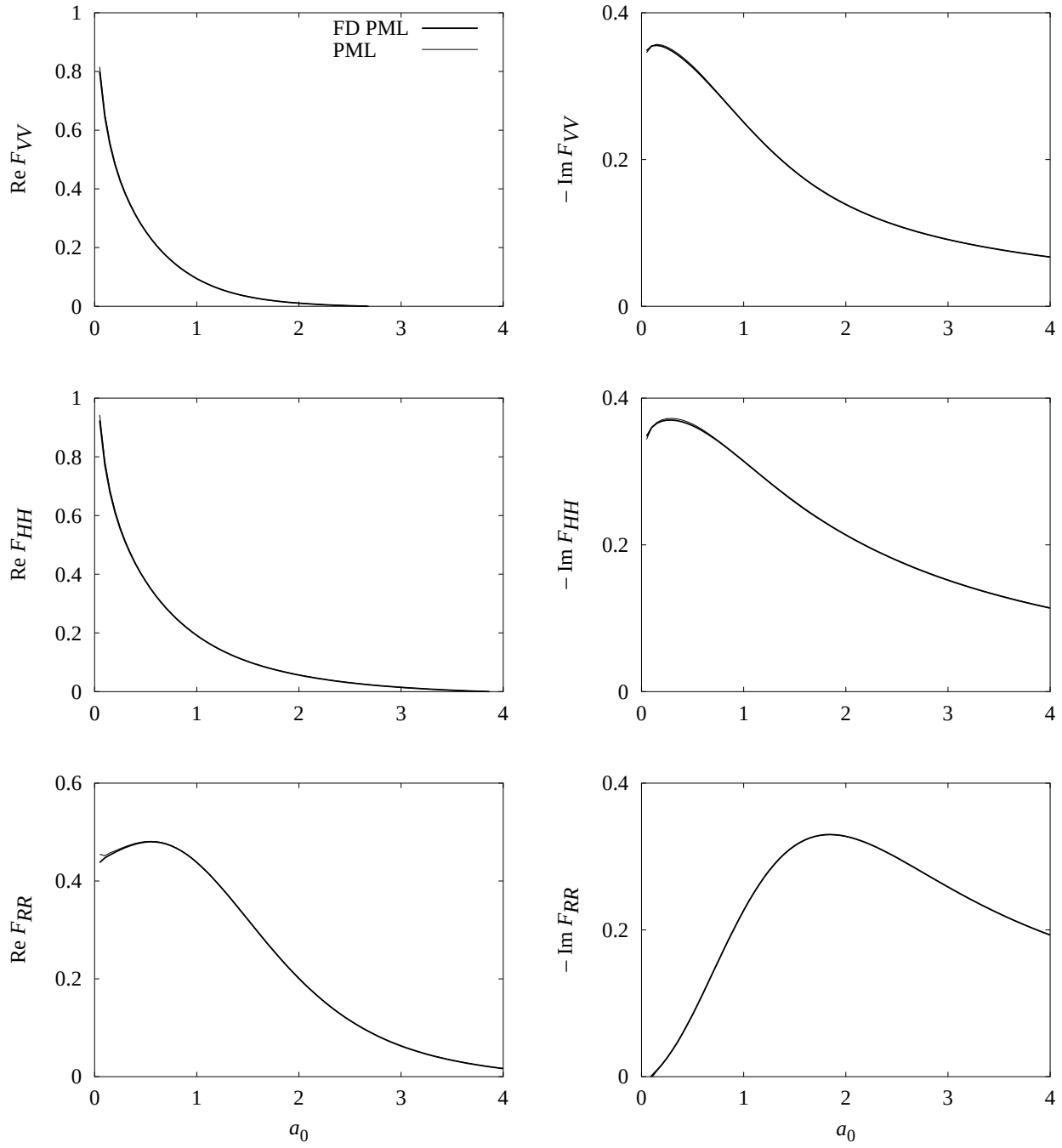

Figure 6.3. Dynamic flexibility coefficients of rigid strip on visco-elastic half-plane computed using a PML model with stretching functions suitable for time-domain analysis; $L = 3b/2$, $h = b/2$, $L_P = b$, $f_1(x_1) = 10\langle x_1 - h\rangle / L_P$, $f_2(x_2) = 10\langle |x_2| - L\rangle / L_P$; $\mu = 1$, $\nu = 0.25$, $\zeta = 0.05$; "FD PML": a substitute for an exact result, obtained using frequency-domain stretching functions in PML model.

that of the dashpot model. Significantly, the extended-mesh results show some spurious reflections for vertical motion of the footing: the P-wave speed in the half-plane is high enough that the depth of the extended mesh is not adequate for the time interval in the analysis; the cost of the extended-mesh model is observed to be approximately 18 times that of the PML model. Figures 6.5 and 6.6 demonstrate that the time-domain stretching functions provide frequency-dependent flexibility coefficients that closely match those obtained using the frequency-domain-only stretching functions.

Figure 5.6a shows a cross section of the rigid strip supported by a layer on a rigid base, and Fig. 5.6b shows a corresponding PML model where $f_i^{\mathrm{e}} = f_i^{\mathrm{p}} = f_i$ in Eq. (4.2), with $f_1(x_1) = 0$ and $f_2(x_2)$ linear in the PML. The corresponding viscous-dashpot model includes the entire bounded domain as (visco-)elastic, with viscous dashpots replacing the fixed lateral boundaries. The extended-mesh model is also a viscous-dashpot model, but extending to $40b$ on either side from the center of the footing. Figure 6.7 demonstrates the high accuracy of the PML model, as well as the small size of the computational domain through the inadequacy of the dashpot model. These results from the PML model are obtained at a cost approximately 1.2 times that of the dashpot model, i.e., the computational cost is not significantly large. The cost of the extended-mesh model is observed to be approximately 3 times that of the PML model; it is relatively cheaper here than in the previous two cases because the extension of the mesh is only in the lateral directions, not downwards.

Figure 6.8 demonstrates that for a rigid strip on an elastic layer on rigid base, the frequency-dependent flexibility coefficients obtained using the time-domain stretching functions do not always closely follow those from the frequency-domain-only stretching functions; this is presumably due to the presence of evanescent modes in the system. However, this apparent inadequacy of the time-domain stretching functions is not reflected in the time domain results in Fig. 6.7a. The time-domain stretching functions provide accurate results for a rigid strip on a visco-elastic layer, as demonstrated in Fig. 6.9.

6.3 Three-dimensional problems

6.3.1 Time-domain equations for the PML

For three-dimensional problems, the stretch tensor $\mathbf{\Lambda}$ is given by Eqs. (4.3a) and (4.23), and the product $\jmath\mathbf{\Lambda}$ is given by Eq. (4.24), but with c_s replacing C in all instances. Following the approach of Sec. 6.2.1, but using the above definitions of $\mathbf{\Lambda}$ and $\jmath\mathbf{\Lambda}$, Eq. (6.1) is transformed into the time-domain equations for the three-dimensional elastic PML:

$$\operatorname{div}\left(\boldsymbol{\sigma}\tilde{\mathbf{F}}^{\mathrm{ee}} + \mathbf{\Sigma}\tilde{\mathbf{F}}^{\mathrm{ep}} + \tilde{\mathbf{\Sigma}}\tilde{\mathbf{F}}^{\mathrm{pp}}\right) = \rho f_{\mathrm{M}}\,\ddot{\boldsymbol{u}} + \rho\frac{c_s}{b}f_{\mathrm{C}}\,\dot{\boldsymbol{u}} + \frac{\mu}{b^2}f_{\mathrm{K}}\,\boldsymbol{u} + \rho\left(\frac{c_s}{b}\right)^3 f_{\mathrm{H}}\,\boldsymbol{U} \tag{6.22a}$$

$$\boldsymbol{\sigma} = \mathbf{C}\left(\boldsymbol{\varepsilon} + \frac{2\zeta b}{c_s}\,\dot{\boldsymbol{\varepsilon}}\right) \tag{6.22b}$$

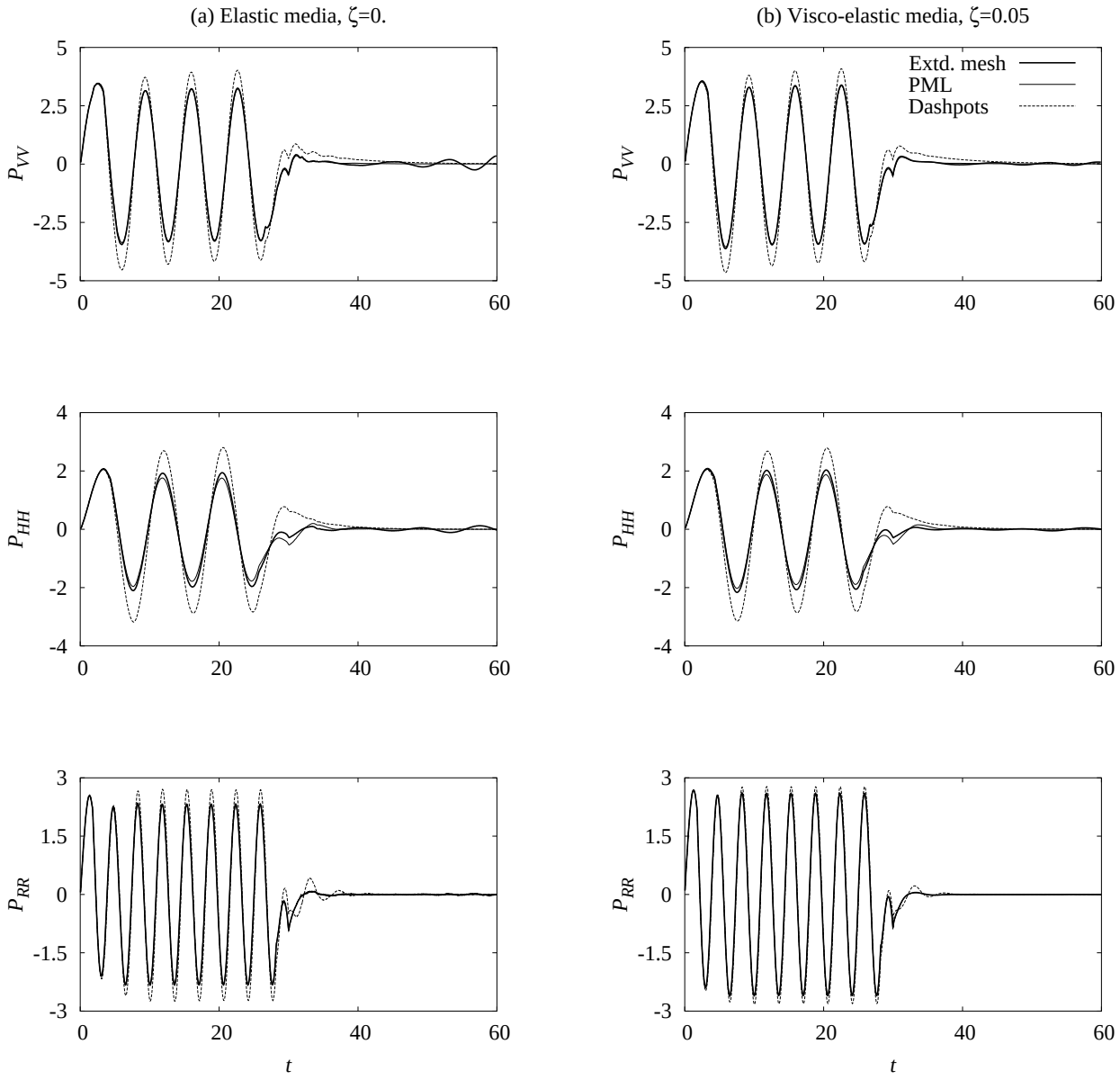

Figure 6.4. Reactions of a rigid strip on (visco-)elastic layer on half-plane, due to imposed displacements; $L = 3b/2$, $L_P = b$, $h = b/2$, $f_1(x_1) = 10\langle x_1 - (d+h)\rangle/L_P$, $f_2(x_2) = 10\langle |x_2| - L\rangle/L_P$; $d = 2b$, $\mu_l = 1$, $\mu_h = 4\mu_l$, $\nu = 0.4$ ($\kappa = 4.67$); $t_d = 30$, $\omega_f = 1.00$ for vertical excitation, 0.75 for horizontal excitation, 1.75 for rocking excitation.

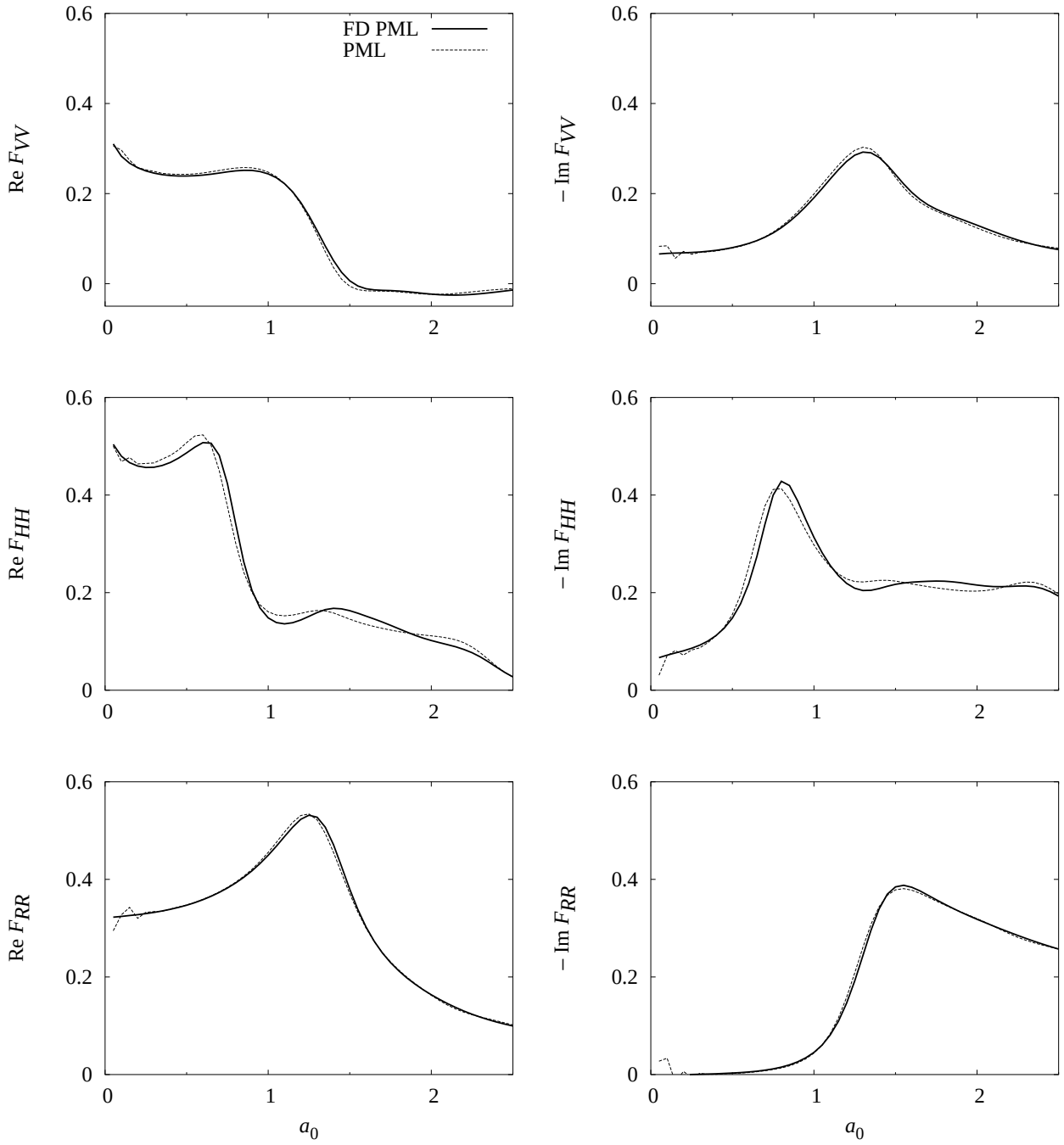

Figure 6.5. Dynamic flexibility coefficients of rigid strip on elastic layer on half-plane computed using a PML model with stretching functions suitable for time-domain analysis; $L = 3b/2$, $L_P = b$, $h = b/2$, $f_1(x_1) = 10\langle x_1 - (d + h)\rangle/L_P$, $f_2(x_2) = 10\langle |x_2| - L\rangle/L_P$; $d = 2b$, $\mu_l = 1$, $\mu_h = 4\mu_l$, $\nu = 0.4$, $a_0 = \omega b/\sqrt{\mu_l/\rho}$; "FD PML": a substitute for an exact result, obtained using frequency-domain stretching functions in PML model.

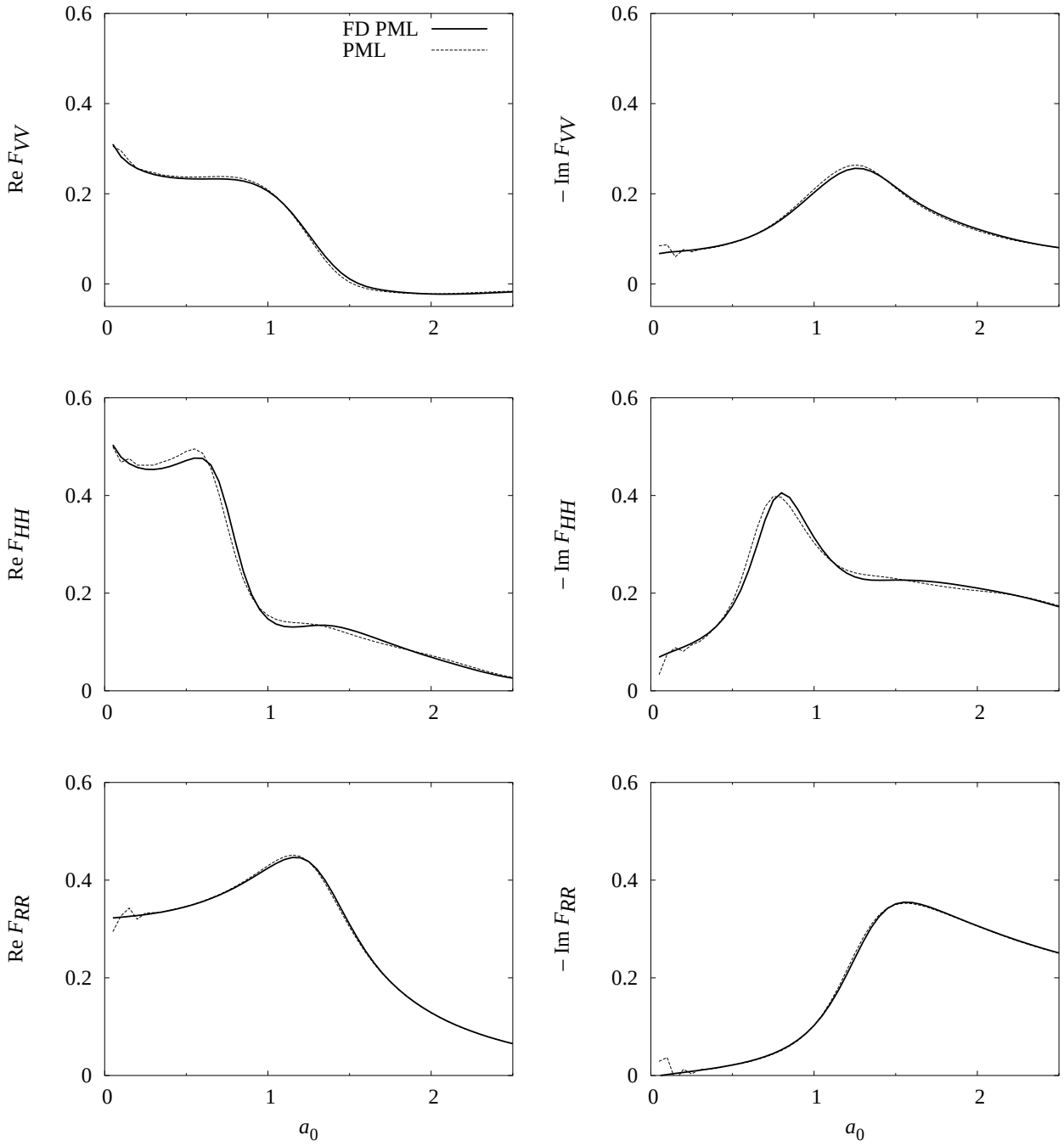

Figure 6.6. Dynamic flexibility coefficients of rigid strip on visco-elastic layer on half-plane computed using a PML model with stretching functions suitable for time-domain analysis; $L = 3b/2$, $L_P = b$, $h = b/2$, $f_1(x_1) = 10\langle x_1 - (d + h)\rangle/L_P$, $f_2(x_2) = 10\langle |x_2| - L\rangle/L_P$; $d = 2b$, $\mu_l = 1$, $\mu_h = 4\mu_l$, $\nu = 0.4$, $\zeta = 0.05$, $a_0 = \omega b/\sqrt{\mu_l/\rho}$; "FD PML": a substitute for an exact result, obtained using frequency-domain stretching functions in PML model.

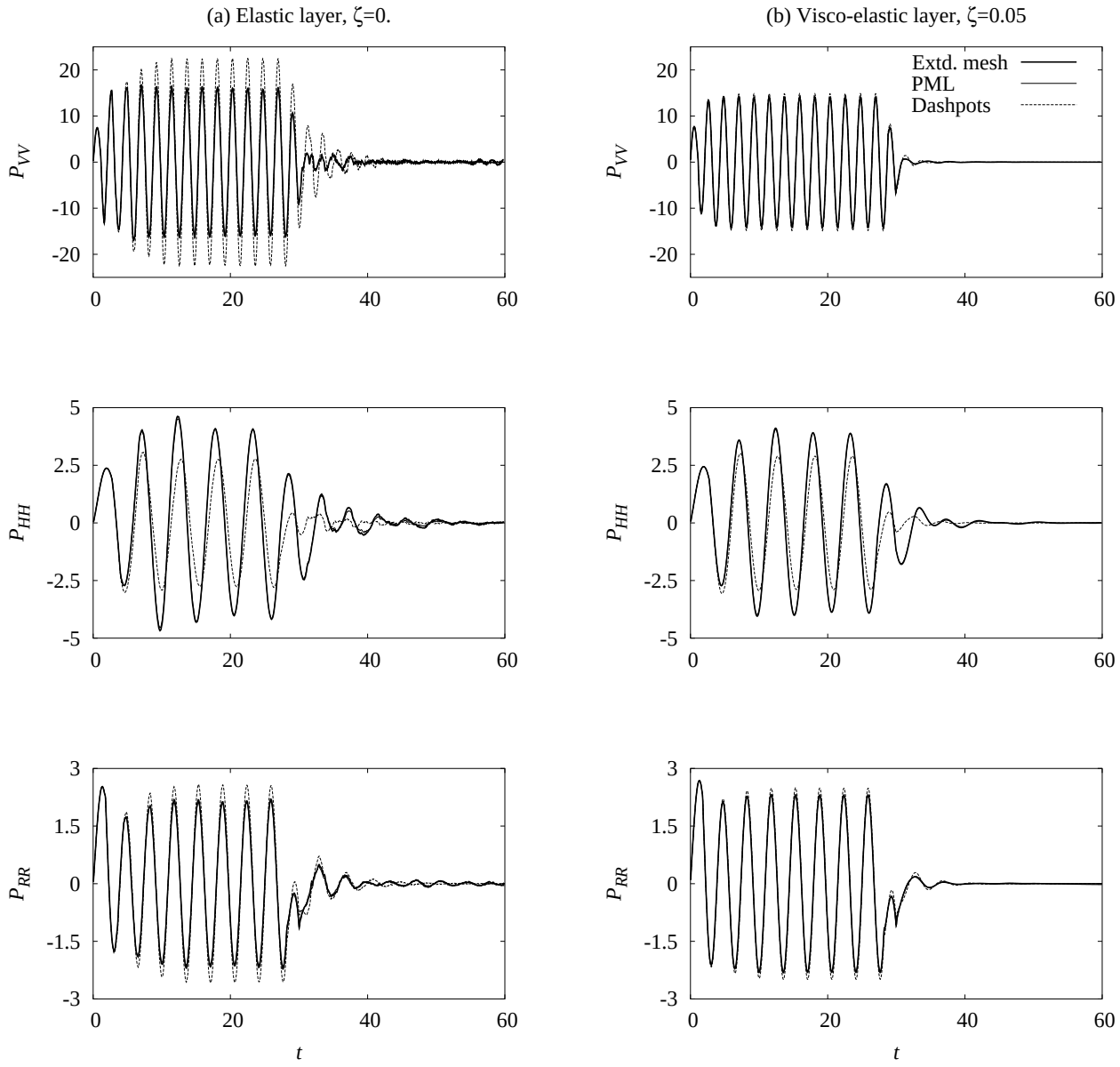

Figure 6.7. Reactions of a rigid strip on (visco-)elastic layer on rigid base, due to imposed displacements; $L = 3b/2$, $L_P = b$, $f_1(x_1) = 0$, $f_2(x_2) = 20\langle|x_2| - L\rangle/L_P$; $d = 2b$, $\mu = 1$, $\nu = 0.4$ ($\kappa = 4.67$); $t_d = 30$, $\omega_f = 2.75$ for vertical excitation, 1.25 for horizontal excitation, 1.75 for rocking excitation.

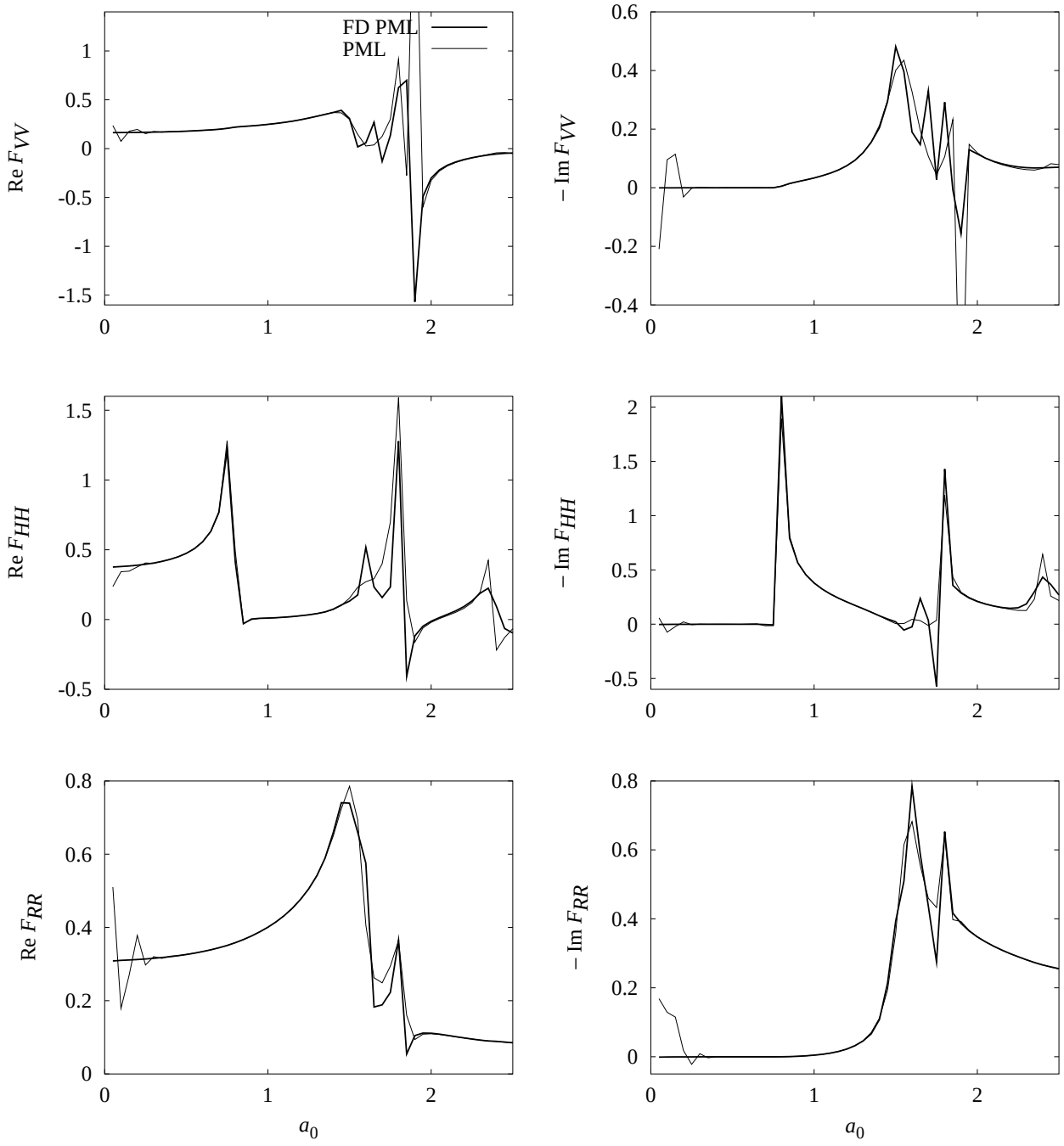

Figure 6.8. Dynamic flexibility coefficients of rigid strip on elastic layer on rigid base computed using a PML model with stretching functions suitable for time-domain analysis; $L = 3b/2$, $L_P = b$, $f_1(x_1) = 0$, $f_2(x_2) = 20\langle|x_2| - L\rangle/L_P$; $d = 2b$, $\mu = 1$, $\nu = 0.4$; "FD PML": a substitute for an exact result, obtained using frequency-domain stretching functions in PML model.

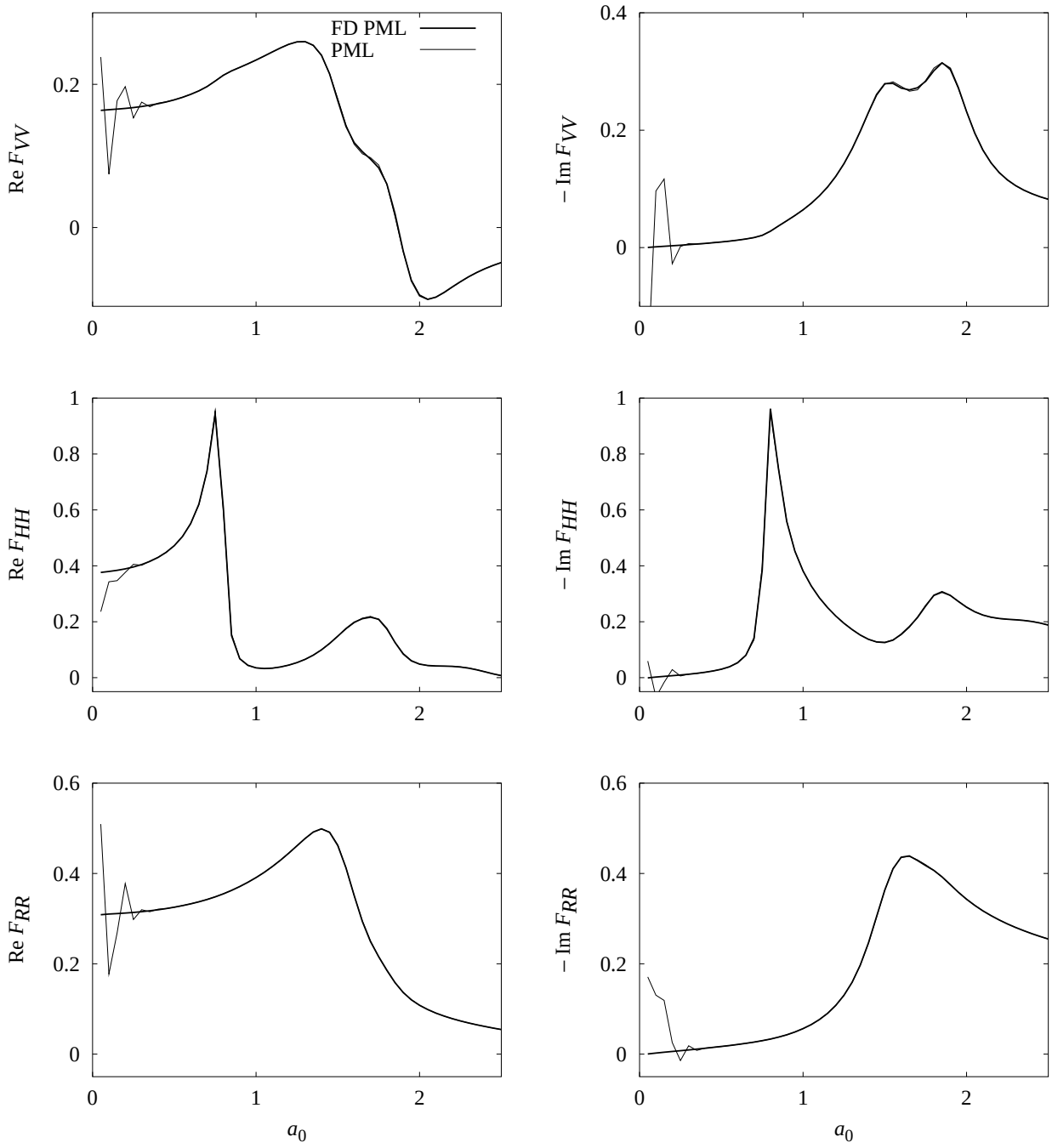

Figure 6.9. Dynamic flexibility coefficients of rigid strip on visco-elastic layer on rigid base computed using a PML model with stretching functions suitable for time-domain analysis; $L = 3b/2$, $L_P = b$, $f_1(x_1) = 0$, $f_2(x_2) = 20\langle|x_2| - L\rangle/L_P$; $d = 2b$, $\mu = 1$, $\nu = 0.4$, $\zeta = 0.05$; "FD PML": a substitute for an exact result, obtained using frequency-domain stretching functions in PML model.

$$\mathbf{F}^{\mathrm{e}T}\dot{\boldsymbol{\varepsilon}}\mathbf{F}^{\mathrm{e}} + \left(\mathbf{F}^{\mathrm{p}T}\boldsymbol{\varepsilon}\mathbf{F}^{\mathrm{e}} + \mathbf{F}^{\mathrm{e}T}\boldsymbol{\varepsilon}\mathbf{F}^{\mathrm{p}}\right) + \mathbf{F}^{\mathrm{p}T}\mathbf{E}\mathbf{F}^{\mathrm{p}} = \frac{1}{2}\left[\mathbf{F}^{\mathrm{e}T}\,(\operatorname{grad}\dot{\boldsymbol{u}}) + (\operatorname{grad}\dot{\boldsymbol{u}})^T\,\mathbf{F}^{\mathrm{e}}\right] + \frac{1}{2}\left[\mathbf{F}^{\mathrm{p}T}\,(\operatorname{grad}\boldsymbol{u}) + (\operatorname{grad}\boldsymbol{u})^T\,\mathbf{F}^{\mathrm{p}}\right] \tag{6.22c}$$

where $\tilde{\mathbf{F}}^{\mathrm{ee}}$, $\tilde{\mathbf{F}}^{\mathrm{ep}}$ and $\tilde{\mathbf{F}}^{\mathrm{pp}}$ are as in Eqs. (4.25) and (4.26), and $\mathbf{F}^{\mathrm{e}}$ and $\mathbf{F}^{\mathrm{p}}$ defined for three-dimensional problems as in Eq. (4.23), but with c_s replacing C throughout, f_{M}, f_{C}, f_{K} and f_{H} are as in Eq. (4.30), and

$$\boldsymbol{U} := \int_0^t \boldsymbol{u}\,\mathrm{d}\tau, \qquad \mathbf{E} := \int_0^t \boldsymbol{\varepsilon}\,\mathrm{d}\tau, \qquad \boldsymbol{\Sigma} := \int_0^t \boldsymbol{\sigma}\,\mathrm{d}\tau, \qquad \tilde{\boldsymbol{\Sigma}} := \int_0^t \boldsymbol{\Sigma}\,\mathrm{d}\tau \tag{6.23}$$

Application of the inverse Fourier transform to obtain $\boldsymbol{U}$, $\mathbf{E}$ and $\boldsymbol{\Sigma}$ assumes that $\bar{\boldsymbol{u}}(\omega = 0) = 0$, $\bar{\boldsymbol{\varepsilon}}(\omega = 0) = 0$, $\bar{\boldsymbol{\sigma}}(\omega = 0) = 0$.

6.3.2 Finite-element implementation

Equation (6.22) is implemented using a standard displacement-based finite-element approach [71]. The weak form of Eq. (6.22a) is derived by taking its inner product with an arbitrary weighting function $\boldsymbol{w}$ residing in an appropriate admissible space, and then integrating over the entire computational domain Ω using integration-by-parts and the divergence theorem to obtain

$$\int_\Omega \rho f_{\mathrm{M}}\boldsymbol{w}\cdot\ddot{\boldsymbol{u}}\,\mathrm{d}\Omega + \int_\Omega \rho\frac{c_s}{b}f_{\mathrm{C}}\boldsymbol{w}\cdot\dot{\boldsymbol{u}}\,\mathrm{d}\Omega + \int_\Omega \frac{\mu}{b^2}f_{\mathrm{K}}\boldsymbol{w}\cdot\boldsymbol{u}\,\mathrm{d}\Omega + \int_\Omega \rho\left(\frac{c_s}{b}\right)^3 f_{\mathrm{H}}\boldsymbol{w}\cdot\boldsymbol{U}\,\mathrm{d}\Omega + \int_\Omega \tilde{\boldsymbol{\varepsilon}}^{\mathrm{ee}} : \boldsymbol{\sigma}\,\mathrm{d}\Omega + \int_\Omega \tilde{\boldsymbol{\varepsilon}}^{\mathrm{ep}} : \boldsymbol{\Sigma}\,\mathrm{d}\Omega + \int_\Omega \tilde{\boldsymbol{\varepsilon}}^{\mathrm{pp}} : \tilde{\boldsymbol{\Sigma}}\,\mathrm{d}\Omega = \int_\Gamma \boldsymbol{w}\cdot\left(\boldsymbol{\sigma}\tilde{\mathbf{F}}^{\mathrm{ee}} + \boldsymbol{\Sigma}\tilde{\mathbf{F}}^{\mathrm{ep}} + \tilde{\boldsymbol{\Sigma}}\tilde{\mathbf{F}}^{\mathrm{pp}}\right)\boldsymbol{n}\,\mathrm{d}\Gamma \tag{6.24}$$

where $\Gamma := \partial\Omega$ is the boundary of Ω and $\boldsymbol{n}$ is the unit outward normal to Γ. The symmetry of $\boldsymbol{\sigma}$ and $\boldsymbol{\Sigma}$ is used to obtain the last three integrals on the left-hand side, with

$$\tilde{\boldsymbol{\varepsilon}}^{\mathrm{ee}} := \frac{1}{2}\left[(\operatorname{grad}\boldsymbol{w})\,\tilde{\mathbf{F}}^{\mathrm{ee}} + \tilde{\mathbf{F}}^{\mathrm{ee}T}\,(\operatorname{grad}\boldsymbol{w})^T\right], \quad \tilde{\boldsymbol{\varepsilon}}^{\mathrm{ep}} := \frac{1}{2}\left[(\operatorname{grad}\boldsymbol{w})\,\tilde{\mathbf{F}}^{\mathrm{ep}} + \tilde{\mathbf{F}}^{\mathrm{ep}T}\,(\operatorname{grad}\boldsymbol{w})^T\right]$$
$$\tilde{\boldsymbol{\varepsilon}}^{\mathrm{pp}} := \frac{1}{2}\left[(\operatorname{grad}\boldsymbol{w})\,\tilde{\mathbf{F}}^{\mathrm{pp}} + \tilde{\mathbf{F}}^{\mathrm{pp}T}\,(\operatorname{grad}\boldsymbol{w})^T\right] \tag{6.25}$$

The weak form is first spatially discretised by interpolating $\boldsymbol{u}$ and $\boldsymbol{w}$ element-wise in terms of nodal quantities using appropriate nodal shape functions. This leads to the system of equations

$$\mathbf{m}\ddot{\boldsymbol{d}} + \mathbf{c}\dot{\boldsymbol{d}} + \mathbf{k}\boldsymbol{d} + \mathbf{K}\mathcal{D} + \boldsymbol{f}_{\mathrm{int}} = \boldsymbol{f}_{\mathrm{ext}} \tag{6.26}$$

where $\mathcal{D}$ is the time-integral of $\boldsymbol{d}$, $\mathbf{K}$ is the coefficient matrix associated with $\mathcal{D}$, and the other terms have the same connotation as in Eq. (6.6). The system matrices are assembled from element-level constituent matrices, given in terms of their IJ-th nodal submatrices as

$$\mathbf{m}^e_{IJ} = \int_{\Omega^e} \rho f_{\mathrm{M}} N_I N_J\,\mathrm{d}\Omega\,\mathbf{I}, \quad \mathbf{c}^e_{IJ} = \int_{\Omega^e} \rho\frac{c_s}{b} f_{\mathrm{C}} N_I N_J\,\mathrm{d}\Omega\,\mathbf{I}$$
$$\mathbf{k}^e_{IJ} = \int_{\Omega^e} \frac{\mu}{b^2} f_{\mathrm{K}} N_I N_J\,\mathrm{d}\Omega\,\mathbf{I}, \quad \mathbf{K}^e_{IJ} = \int_{\Omega^e} \rho\left(\frac{c_s}{b}\right)^3 f_{\mathrm{H}} N_I N_J\,\mathrm{d}\Omega\,\mathbf{I} \tag{6.27a}$$

where N_I is the shape function for node I and $\mathbf{I}$ is the identity matrix of size 3×3. The element-level internal force term is given by

$$\boldsymbol{f}^e = \int_{\Omega^e} \tilde{\mathbf{B}}^{\mathrm{ee}\,T} \hat{\boldsymbol{\sigma}}\, \mathrm{d}\Omega + \int_{\Omega^e} \tilde{\mathbf{B}}^{\mathrm{ep}\,T} \hat{\boldsymbol{\Sigma}}\, \mathrm{d}\Omega + \int_{\Omega^e} \tilde{\mathbf{B}}^{\mathrm{pp}\,T} \hat{\tilde{\boldsymbol{\Sigma}}}\, \mathrm{d}\Omega \tag{6.27b}$$

where $\tilde{\mathbf{B}}^{\mathrm{ee}}$ is given in terms of its nodal submatrices as

$$\tilde{\mathbf{B}}^{\mathrm{ee}}_I := \begin{bmatrix} \tilde{N}^{\mathrm{ee}}_{I1} & \cdot & \cdot \\ \cdot & \tilde{N}^{\mathrm{ee}}_{I2} & \cdot \\ \cdot & \cdot & \tilde{N}^{\mathrm{ee}}_{I3} \\ \tilde{N}^{\mathrm{ee}}_{I2} & \tilde{N}^{\mathrm{ee}}_{I1} & \cdot \\ \tilde{N}^{\mathrm{ee}}_{I3} & \cdot & \tilde{N}^{\mathrm{ee}}_{I1} \\ \cdot & \tilde{N}^{\mathrm{ee}}_{I3} & \tilde{N}^{\mathrm{ee}}_{I2} \end{bmatrix} \tag{6.28}$$

and $\tilde{\mathbf{B}}^{\mathrm{ep}}$ and $\tilde{\mathbf{B}}^{\mathrm{pp}}$ are defined similarly, but with $\tilde{N}^{\mathrm{ee}}_{Ii}$ replaced by $\tilde{N}^{\mathrm{ep}}_{Ii}$ and $\tilde{N}^{\mathrm{pp}}_{Ii}$, respectively, where $\tilde{N}^{\mathrm{ee}}_{Ii}$ etc. are defined as

$$\tilde{N}^{\mathrm{ee}}_{Ii} := \tilde{F}^{\mathrm{ee}}_{ij} N_{I,j}, \quad \tilde{N}^{\mathrm{ep}}_{Ii} := \tilde{F}^{\mathrm{ep}}_{ij} N_{I,j}, \quad \tilde{N}^{\mathrm{pp}}_{Ii} := \tilde{F}^{\mathrm{pp}}_{ij} N_{I,j} \tag{6.29}$$

Furthermore

$$\hat{\boldsymbol{\sigma}} := \begin{Bmatrix} \sigma_{11} \\ \sigma_{22} \\ \sigma_{33} \\ \sigma_{12} \\ \sigma_{13} \\ \sigma_{23} \end{Bmatrix} \tag{6.30}$$

with $\hat{\boldsymbol{\Sigma}}$ the time-integral of $\hat{\boldsymbol{\sigma}}$, and $\hat{\tilde{\boldsymbol{\Sigma}}}$ that of $\hat{\boldsymbol{\Sigma}}$. The attenuation functions f^{e}_i and f^{p}_i are defined globally on the computational domain, not element-wise. It is conveniently assumed that there is no contribution to $\boldsymbol{f}_{\mathrm{ext}}$ from a free boundary of the PML.

Towards solution of the equations of motion, Eq. (6.22c) is approximated as in Eq. (6.12), but with

$$\hat{\boldsymbol{\varepsilon}} := \begin{Bmatrix} \varepsilon_{11} \\ \varepsilon_{22} \\ \varepsilon_{33} \\ 2\varepsilon_{12} \\ 2\varepsilon_{13} \\ 2\varepsilon_{23} \end{Bmatrix} \tag{6.31}$$

and the matrices $\mathbf{B}^{\epsilon}$, $\mathbf{B}^{\varrho}$, $\hat{\mathbf{F}}^{\epsilon}$ and $\hat{\mathbf{F}}^{\varrho}$ as defined in Appendix C. Equation (6.22b) is approximated as in Eq. (6.14) but with $\mathbf{D}$ now defined as in the first expression in Eq. (5.18b).

Equation (6.27b) is cast into a time-discrete form by approximating $\hat{\boldsymbol{\Sigma}}_{n+1}$ as in Eq. (6.16) and approximating $\hat{\tilde{\boldsymbol{\Sigma}}}_{n+1}$ as

$$\hat{\tilde{\boldsymbol{\Sigma}}}_{n+1} = \hat{\tilde{\boldsymbol{\Sigma}}}_n + \hat{\boldsymbol{\Sigma}}_{n+1} \Delta t \tag{6.32}$$

Substituting these approximations into Eq. (6.27b) gives

$$\boldsymbol{f}^e_{n+1} = \int_{\Omega^e} \tilde{\mathbf{B}}^T \hat{\boldsymbol{\sigma}}_{n+1}\,\mathrm{d}\Omega + \int_{\Omega^e} \tilde{\mathbf{B}}^{\mathrm{ec}\,T} \hat{\boldsymbol{\Sigma}}_n\,\mathrm{d}\Omega + \int_{\Omega^e} \tilde{\mathbf{B}}^{\mathrm{pp}\,T} \hat{\tilde{\boldsymbol{\Sigma}}}_n\,\mathrm{d}\Omega \tag{6.33}$$

where

$$\begin{aligned} \tilde{\mathbf{B}} &:= \tilde{\mathbf{B}}^{\mathrm{ee}} + \tilde{\mathbf{B}}^{\mathrm{ep}}\Delta t + \tilde{\mathbf{B}}^{\mathrm{pp}}\Delta t^2 \\ \tilde{\mathbf{B}}^{\mathrm{ec}} &:= \tilde{\mathbf{B}}^{\mathrm{ep}} + \tilde{\mathbf{B}}^{\mathrm{pp}}\Delta t \end{aligned} \tag{6.34}$$

The linearisation of Eq. (6.33) gives tangent matrices as in Eq. (6.21) with Eq. (6.20), but with the relevant matrices appropriately defined for three-dimensional problems, as above. These matrices are not symmetric, but are independent of $\boldsymbol{d}$, making this a linear model.

Finally, the time-integral of $\boldsymbol{d}$ is approximated as

$$\mathcal{D}_{n+1} = \mathcal{D}_n + \boldsymbol{d}_{n+1}\Delta t \tag{6.35}$$

Thus the term involving $\mathcal{D}$ in Eq. (6.26) may be linearised as

$$\Delta\left(\mathbf{K}\mathcal{D}_{n+1}\right) = \left(\mathbf{K}\Delta t\right)\Delta\boldsymbol{d}_{n+1} \tag{6.36}$$

Note that $\mathcal{D}$ is required only where $\mathbf{K}^e \neq \mathbf{0}$, i.e., from Eq. (6.27a), wherever $f_{\mathrm{H}} \neq 0$. From Eq. (4.30), it can be seen that this holds only in the corner regions of the PML, where waves are attenuated in all three coordinate directions. Thus $\mathcal{D}_n$ needs to be stored and updated only in the corner regions.

The profusion of notation and equations in this section cries out for a synopsis of the algorithm for computing the element-level effective internal force and tangent stiffness; this is presented in Box 6.2.

6.3.3 Explicit integration

The implementation of the three-dimensional time-domain elastic PML for implicit integration produces a large unsymmetric system of equations which are difficult to solve directly using existing equation solvers. Consequently, it is prudent to use explicit time-integration [64] to compute the response of the system, and thus avoid computation of its stiffness matrix.

Explicit integration requires that inertial matrices be lumped. To this end, the matrices in Eq. (6.27a) — all of which arise from the inertical term on the right-hand side of Eq. (6.1a) — are lumped by assigning to each diagonal entry the sum of all the entries in its row, to get:

$$\begin{aligned} \mathbf{m}^e &= \int_{\Omega^e} \rho f_{\mathrm{M}} \mathbf{N}_d\,\mathrm{d}\Omega, \quad \mathbf{c}^e = \int_{\Omega^e} \rho \left(\frac{c_s}{b}\right) f_{\mathrm{C}} \mathbf{N}_d\,\mathrm{d}\Omega \\ \mathbf{k}^e &= \int_{\Omega^e} \frac{\mu}{b^2} f_{\mathrm{K}} \mathbf{N}_d\,\mathrm{d}\Omega, \quad \mathbf{K}^e = \int_{\Omega^e} \rho \left(\frac{c_s}{b}\right)^3 f_{\mathrm{H}} \mathbf{N}_d\,\mathrm{d}\Omega \end{aligned} \tag{6.37}$$

Box 6.2. Computing effective force and stiffness for 3D elastic PML element.

1. Compute system matrices $\mathbf{m}^e$, $\mathbf{c}^e$, $\mathbf{k}^e$ and $\mathbf{K}^e$ [Eq. (6.27a)].
2. Compute internal force $\boldsymbol{f}^e_{n+1}$ [Eq. (6.33)].
   Use $\hat{\boldsymbol{\varepsilon}}_{n+1}$ [Eq. (6.12) with Appendix C], and $\hat{\boldsymbol{\sigma}}_{n+1}$ [Eq. (6.14) with Eq. (5.18b)].
3. Compute tangent matrices $\check{\mathbf{c}}^e$ and $\check{\mathbf{k}}^e$ [Eq. (6.21) with Eq. (6.34)].
4. Compute effective internal force $\tilde{\boldsymbol{f}}^e_{n+1}$ and tangent stiffness $\tilde{\mathbf{k}}^e$:

$$\tilde{\boldsymbol{f}}^e_{n+1} = \mathbf{m}^e \boldsymbol{a}_{n+1} + \mathbf{c}^e \boldsymbol{v}_{n+1} + \mathbf{k}^e \boldsymbol{d}_{n+1} + \mathbf{K}^e \mathcal{D}_{n+1} + \boldsymbol{f}^e_{n+1}$$
$$\tilde{\mathbf{k}}^e = \alpha_{\mathrm{k}} \left(\mathbf{k}^e + \check{\mathbf{k}}^e + \mathbf{K}^e \Delta t \right) + \alpha_{\mathrm{c}} \left(\mathbf{c}^e + \check{\mathbf{c}}^e \right) + \alpha^e_{\mathrm{m}}$$

   where $\boldsymbol{a}_{n+1} \approx \ddot{\boldsymbol{d}}^e(t_{n+1})$, and, for example,

$$\alpha_{\mathrm{k}} = 1, \quad \alpha_{\mathrm{c}} = \frac{\gamma}{\beta \Delta t}, \quad \alpha_{\mathrm{m}} = \frac{1}{\beta \Delta t^2}$$

   for the Newmark method.

Note: The tangent stiffness $\tilde{\mathbf{k}}^e$ is independent of the solution, and thus has to be computed only once. However, the internal force $\boldsymbol{f}^e_{n+1}$ has to be re-computed at each time-step because it is dependent on the solution at past times.

where

$$\mathbf{N}_d = \mathrm{diag}\,(N_1 \mathbf{1}, N_2 \mathbf{1}, \ldots, N_8 \mathbf{1}) \qquad \text{with} \quad \mathbf{1} := [1, 1, 1] \tag{6.38}$$

It is necessary to lump all the inertial matrices; lumping only the mass matrix, the minimum requirement for explicit integration, may lead to strong long-time instabilities in the system. To obtain a displacement-based formulation, the terms $\mathbf{c}\dot{\boldsymbol{d}}$, $\mathbf{k}\boldsymbol{d}$ and $\mathbf{K}\mathcal{D}$ in Eq. (6.26) are computed at the element level using Eq. (6.37), and then assembled into the global force vector.

Furthermore, because an explicit time-integration scheme does not have the overhead of solving a system of equations, it is crucial to compute the internal force as efficiently as possible. Toward this goal, the strain terms are computed from Eq. (6.22c) by transforming into the PML basis $\{\boldsymbol{e}'_i\}$, which diagonalises the matrices $\mathbf{F}^{\mathrm{e}}$ and $\mathbf{F}^{\mathrm{p}}$. The approximations in Eq. (6.11) are used in Eq. (6.22c) to obtain

$$\begin{aligned} \boldsymbol{\varepsilon}_{n+1} \Delta t = {} & \frac{1}{2} \left[\mathbf{F}^{\epsilon T} \left(\mathrm{grad}\, \dot{\boldsymbol{u}}|_{n+1/2} \right) \mathbf{F}^{\imath} + \mathbf{F}^{\imath T} \left(\mathrm{grad}\, \dot{\boldsymbol{u}}|_{n+1/2} \right)^T \mathbf{F}^{\epsilon} \right] \\ & + \frac{1}{2} \left[\mathbf{F}^{\varrho T} \left(\mathrm{grad}\, \boldsymbol{u}_{n+1} \right) \mathbf{F}^{\imath} + \mathbf{F}^{\imath T} \left(\mathrm{grad}\, \boldsymbol{u}_{n+1} \right)^T \mathbf{F}^{\varrho} \right] \\ & + \frac{1}{\Delta t} \mathbf{F}^{\epsilon T} \boldsymbol{\varepsilon}_n \mathbf{F}^{\epsilon} - \mathbf{F}^{\varrho T} \mathbf{E}_n \mathbf{F}^{\varrho} \end{aligned} \tag{6.39}$$

where

$$\mathbf{F}^{\iota} := \left[\frac{\mathbf{F}^{\mathrm{e}}}{\Delta t} + \mathbf{F}^{\mathrm{p}}\right]^{-1}, \quad \mathbf{F}^{\epsilon} := \mathbf{F}^{\mathrm{e}}\mathbf{F}^{\iota}, \quad \mathbf{F}^{\varrho} := \mathbf{F}^{\mathrm{p}}\mathbf{F}^{\iota} \tag{6.40}$$

Transforming Eq. (6.39) into the PML basis $\{\boldsymbol{e}'_i\}$ gives

$$\begin{aligned}\boldsymbol{\varepsilon}'_{n+1}\Delta t = &\frac{1}{2}\left[\mathbf{F}^{\epsilon\prime}\mathbf{Q}^T\left(\operatorname{grad}\dot{\boldsymbol{u}}|_{n+1/2}\right)\mathbf{Q}\mathbf{F}^{\iota\prime} + \mathbf{F}^{\iota\prime}\mathbf{Q}^T\left(\operatorname{grad}\dot{\boldsymbol{u}}|_{n+1/2}\right)^T\mathbf{Q}\mathbf{F}^{\epsilon\prime}\right]\\ &+\frac{1}{2}\left[\mathbf{F}^{\varrho\prime}\mathbf{Q}^T\left(\operatorname{grad}\boldsymbol{u}_{n+1}\right)\mathbf{Q}\mathbf{F}^{\iota\prime} + \mathbf{F}^{\iota\prime}\mathbf{Q}^T\left(\operatorname{grad}\boldsymbol{u}_{n+1}\right)^T\mathbf{Q}\mathbf{F}^{\varrho\prime}\right]\\ &+\frac{1}{\Delta t}\mathbf{F}^{\epsilon\prime}\boldsymbol{\varepsilon}'_n\mathbf{F}^{\epsilon\prime} - \mathbf{F}^{\varrho\prime}\mathbf{E}'_n\mathbf{F}^{\varrho\prime}\end{aligned} \tag{6.41}$$

where the primed tensors are given by, e.g., $\boldsymbol{\varepsilon}'_n = \mathbf{Q}^T\boldsymbol{\varepsilon}_n\mathbf{Q}$. Note that the tensors $\mathbf{F}^{\epsilon\prime}$, $\mathbf{F}^{\varrho\prime}$ and $\mathbf{F}^{\iota\prime}$ are diagonal tensors.

The quantity $\mathbf{Q}^T\left(\operatorname{grad}\boldsymbol{u}\right)\mathbf{Q}$ in Eq. (6.41) — dropping the time-step subscript for ease of notation — is in fact the displacement gradient in the PML basis, which can be checked by computing it using indices: if the displacement $\boldsymbol{u}$ is interpolated as $u_k = N_I d_k^I$, where N_I is the shape function value for node I, and d_k^I is the displacement of node I in the direction $\boldsymbol{e}_i$, then

$$\mathbf{Q}^T\left(\operatorname{grad}\boldsymbol{u}\right)\mathbf{Q} \equiv u'_{i,j} = d_i^{I\prime}N'_{I,j} \quad \text{with} \quad d_i^{I\prime} := Q_{ki}d_k^I, \quad N'_{I,j} := Q_{lj}N_{I,l} \tag{6.42}$$

where $d_i^{I\prime}$ is the displacement in the direction $\boldsymbol{e}'_i$ at node I, obtained by transforming d_k^I into the PML basis, and $N'_{I,j}$ is the gradient of N_I in the direction $\boldsymbol{e}'_j$.

Upon rewriting the velocity terms in Eq. (6.41) in a similar manner, $\boldsymbol{\varepsilon}'_{n+1}$ may be obtained in components as (no summation):

$$\begin{aligned}\left(\varepsilon'_{ij}|_{n+1}\right)\Delta t = &\frac{1}{2}\left[F_i^{\epsilon\prime}\left(v'_{i,j}|_{n+1/2}\right)F_j^{\iota\prime} + F_i^{\iota\prime}\left(v'_{j,i}|_{n+1/2}\right)F_j^{\epsilon\prime}\right]\\ &+\frac{1}{2}\left[F_i^{\varrho\prime}\left(u'_{i,j}|_{n+1}\right)F_j^{\iota\prime} + F_i^{\iota\prime}\left(u'_{j,i}|_{n+1}\right)F_j^{\varrho\prime}\right]\\ &+\frac{1}{\Delta t}F_i^{\epsilon\prime}\left(\varepsilon'_{ij}|_n\right)F_j^{\epsilon\prime} - F_i^{\varrho\prime}\left(E'_{ij}|_n\right)F_j^{\varrho\prime}\end{aligned} \tag{6.43}$$

where $v'_{i,j}$ is the velocity gradient in the PML basis; $F_i^{\epsilon\prime}$ is the i-th diagonal element of $\mathbf{F}^{\epsilon\prime}$, and similarly for $F_i^{\varrho\prime}$ and $F_i^{\iota\prime}$. The strain $\boldsymbol{\varepsilon}_{n+1}$ in the global coordinates may be obtained by transforming $\boldsymbol{\varepsilon}'_{n+1}$ back:

$$\boldsymbol{\varepsilon}_{n+1} = \mathbf{Q}\boldsymbol{\varepsilon}'_{n+1}\mathbf{Q}^T \tag{6.44}$$

The element algorithm for explicit integration is presented below in Box 6.3.

Box 6.3. Computing effective force for explicit integration for 3D elastic PML element.

Initial mass computation

Compute the diagonal element mass matrix $\mathbf{m}^e$ using Eq. (6.27a), with f_{M} defined in Eq. (4.30), and assemble into the global mass matrix.

Element force computation

Compute the internal element force $\boldsymbol{f}^e_{n+1}$ as follows:

1. Compute displacement and velocity gradients in the PML basis, using Eq. (6.42).
2. Compute the strain $\boldsymbol{\varepsilon}'_{n+1}$ in the PML basis using Eq. (6.43) and transform to global coordinates using Eq. (6.44).
3. Compute the stress $\hat{\boldsymbol{\sigma}}_{n+1}$ using Eq. (6.14) with Eq. (5.18b), and the stress time-integrals $\hat{\boldsymbol{\Sigma}}_{n+1}$ and $\hat{\hat{\boldsymbol{\Sigma}}}_{n+1}$ from Eq. (6.16) and (6.32), respectively.
4. Compute the internal force $\boldsymbol{f}^e_{n+1}$ using Eq. (6.33).

Compute the total internal force as follows:

1. Compute the diagonal matrices $\mathbf{c}^e$, $\mathbf{k}^e$, $\mathbf{K}^e$ using Eq. (6.37), with f_{C}, f_{K} and f_{H} given by Eq. (4.30). The matrix $\mathbf{K}^e$ is computed only in the corner regions of the PML model.
2. In the corner regions of the model, compute the time-integral of displacement $\mathcal{D}_{n+1}$ using Eq. (6.35).
3. Add the force term [Eq. (6.26)]

$$\mathbf{c}^e \dot{\boldsymbol{d}}_{n+1/2} + \mathbf{k}^e \boldsymbol{d}_{n+1} + \mathbf{K}^e \mathcal{D}_{n+1}$$

to $\boldsymbol{f}^e_{n+1}$ to get the total internal force. The last term in the above expression is non-zero only in the corner regions of the PML model.

6.3.4 Evaluation of explicit integration with PML

In order to successfully use an explicit integration scheme with the PML model, two key issues need to be evaluated: (a) the effect of PML on the critical time-step size, and (b) the effect of lumping of the PML matrices in Eq. (6.27a) on the accuracy of results. Additionally, we can also evaluate the effect of lumping on the critical time-step size. Because the complexity of the PML equations precludes an analytical evaluation in this paper, we resort to a numerical evaluation in the context of a bar of brick elements, which is analogous to the one-dimensional systems commonly used in the analytical evaluation of stability and accuracy.

Consider a semi-infinite elastic bar with a square cross-section of width b [Fig. 6.10(a)], with shear modulus μ, mass density ρ, and Poisson's ratio ν, subjected to a uniform force at the free end. The time-domain response of this system is studied by applying the force either longitudinally along the axis of the bar — thus simulating P-waves — or transverse to it, thus simulating S-waves, and recording the displacement of the tip in the corresponding direction. In the latter case, the

displacements of the bar along its axis are constrained in order to eliminate the beam bending modes, which are not supported by the PML model. The time variation of the force is given by the waveform in Eq. (A3).

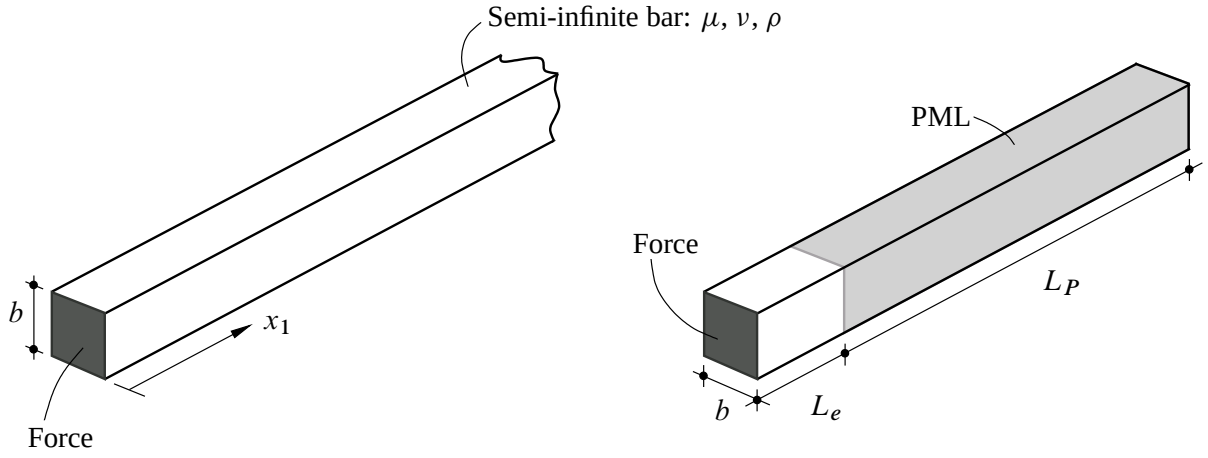

(a) (b)

Figure 6.10. (a) Semi-infinite elastic bar subjected to a uniform force at the free end; (b) a PML model, fixed at the outer boundary.

This bar is modelled using the PML model shown in Fig. 6.10(b), discretised using eight-noded bricks, with one element across the cross-section of the bar, and enough elements along the length of bar to adequately model the wave propagation, thus evoking a one-dimensional system. The attenuation functions within the PML [cf. Eq. (4.2)] are chosen as $f_1^{\mathrm{e}} = f_1^{\mathrm{p}} = f_1$, and $f_2^{\mathrm{e}} = f_2^{\mathrm{p}} = f_3^{\mathrm{e}} = f_3^{\mathrm{p}} \equiv 0$, with f_1 chosen as [79, 91]:

$$f_1(x_1) := f_0 \left(\frac{x_1 - L_e}{L_P} \right) \tag{6.45}$$

In a slight confusion of notation, the characteristic length b of the PML model used in e.g., Eq. (6.37) is taken to be the depth L_P of the PML, and is not the same as the width b of the bar. An extended-mesh model — fully elastic and extending upto $25b$ from the free end, with the same mesh density as the PML model — is used to provide benchmark results for assessing the accuracy of the results from the PML model.

The effect of the PML on the critical time-step size is considered first by comparing the critical time-step size of the PML model to that of a fully-elastic model of the same size, i.e., one where the PML elements have been replaced with elastic elements. The critical time-step size for either model is determined by carrying out the analysis with different time-step sizes and converging upon the maximum step size for which we get stable results. Three variants of the PML model are considered: (a) all inertial matrices lumped [Eq. (6.37)], (b) all inertial matrices consistent

[Eq. (6.27a)], and (c) an intermediate formulation where only the mass matrix is lumped and the other inertial matrices are consistent.

Table 6.4 shows the critical time-step sizes for both the elastic and the PML models, for both lumped and consistent matrices, as well as for the intermediate formulation for the PML. It is seen that for both the lumped and the consistent formulations, the critical time-step size required by the PML model is approximately equal to that of the elastic model. The critical time-step required for the intermediate formulation under transverse excitation is also similar to that required for the lumped formulation. However, for longitudinal excitation, the intermediate formulation exhibits a strong long-time instability in the free-vibration phase irrespective of the time-step size.

Model	Lumped		Consistent		Intermediate	
	Longitudinal	Transverse	Longitudinal	Transverse	Longitudinal	Transverse
Elastic	0.04865	0.05009	0.02582	0.02586	—	
PML	0.04871	0.04921	0.02606	0.02632	unstable	0.04958

Box 6.4. Comparison of critical time-step sizes for three choices of lumping of inertial matrices in the PML model of a semi-infinite bar; $b = 0.1$; $L_e = 0.2$, $L_P = 0.8$; $f_0 = 10$; $t_d = 10$, $\omega_f = 3.0$.

This demonstrates that PML elements with either fully-lumped or fully-consistent matrices do not have any significant effect on the critical time-step size for the corresponding elastic model. Furthermore, the PML elements exhibit behaviour well-known for elastic elements: consistent matrices yield smaller critical time-step sizes than do lumped matrices [65]. This observation allows the speculation that for the intermediate formulation under longitudinal excitation — where the bar is unconstrained except at one end — the specific combination of lumped and consistent matrices reduce the critical time-step size to an unreasonably small value. The longitudinal constraint imposed upon the bar for transverse excitation allows a stable solution for the intermediate formulation.

The effect of lumping on the accuracy of results is considered next. The error in the PML solution is computed relative to the benchmark extended-mesh solution as

$$\%\text{error} := \frac{\max_n \left| \boldsymbol{u}_{\mathrm{p}}(t_n) - \boldsymbol{u}_{\mathrm{e}}(t_n) \right|}{\max_n |\boldsymbol{u}_{\mathrm{e}}(t_n)|} \times 100 \tag{6.46}$$

where $\boldsymbol{u}_{\mathrm{e}}$ and $\boldsymbol{u}_{\mathrm{p}}$ are the tip displacements of the extended-mesh model and the PML model, respectively, at time steps t_n. Figure 6.11 compares the displacements from the consistent and the lumped formulations of the PML against those from the extended mesh, for both longitudinal and transverse excitations, and Table 6.5 shows the errors from the two formulations.

It is difficult to visually distinguish the results from the two PML models, and both follow the extended-mesh result closely. The computed errors from the lumped formulation are seen to be slightly larger than those from the consistent formulation, thus appearing to contradict analyses for elastic elements that posit that lumped masses are well-matched with explicit integration, and are

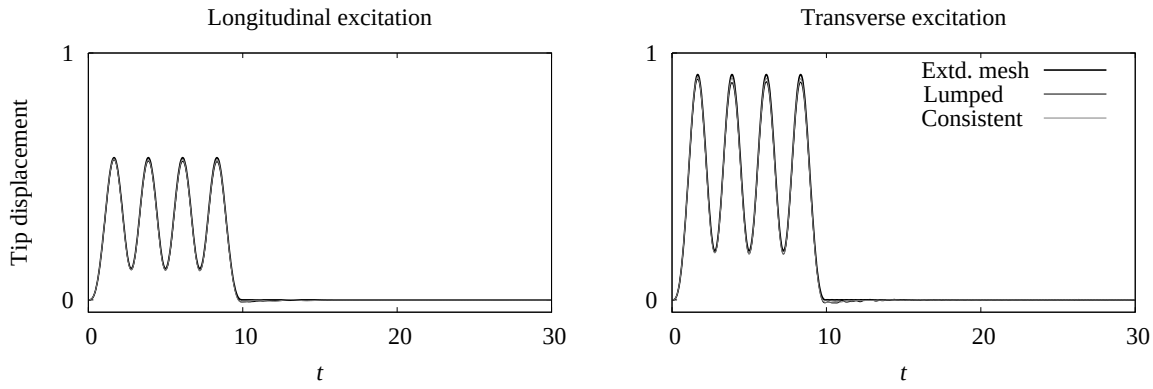

Figure 6.11. Tip displacements of a semi-infinite bar due to applied forces; longitudinal displacements due to longitudinal excitation, transverse displacements due to transverse excitation; $b = 0.1$; $L_e = 0.2$, $L_P = 0.8$; $f_0 = 10$; $t_d = 10$, $\omega_f = 3.0$.

	Longitudinal		Transverse	
	Lumped	Consistent	Lumped	Consistent
%error	2.89	1.73	3.71	2.24

Box 6.5. Comparison of relative error in tip displacement of PML model of semi-infinite bar from consistent and lumped formulations; $b = 0.1$; $L_e = 0.2$, $L_P = 0.8$; $f_0 = 10$; $t_d = 10$, $\omega_f = 3.0$.

likely to produce more accurate results than consistent masses [65,92]. It must be remarked that the error is characterised differently in the two cases: these classical studies of well-matched methods study the error in the natural frequency of the discrete system, whereas here the amplitude error is used to assess accuracy. However, because the difference in accuracy of the two formulations is negligible in practice, it is felt that this discrepancy with earlier analyses does not warrant further investigation.

6.3.5 Numerical results

Numerical results are presented for the classical soil-structure interaction problems of a square flexible footing on a (i) half-space, (ii) layer on a half-space, and (iii) layer on a rigid base.

Figure 6.12(a) shows a quarter-model of a homogeneous isotropic elastic half-space with shear modulus μ, mass density ρ and Poisson's ratio ν, subjected to an uniform force applied over a square area of half-width b. The time-domain response of this system is studied by applying the force either vertically or horizontally, and recording the displacements in the corresponding direction at the center and at the corner of the square; the time variation of the force is of the form in Eq. (A3).

This unbounded-domain system is modelled using the PML model shown in Fig. 6.12(b), discretised using an adequately dense regular mesh of eight-noded bricks. In a slight confusion of

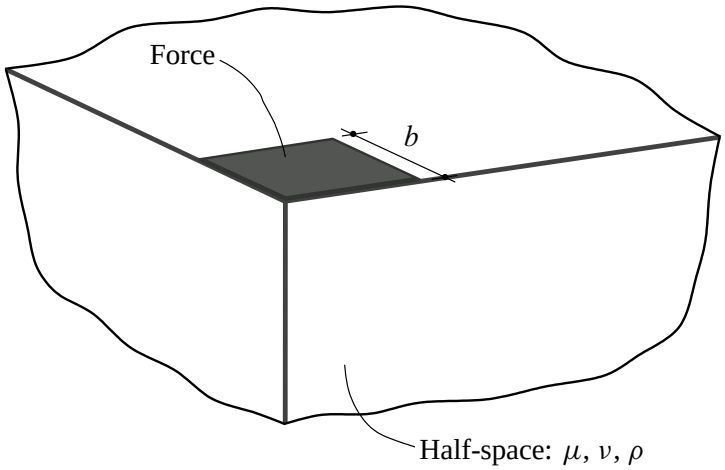

(a)

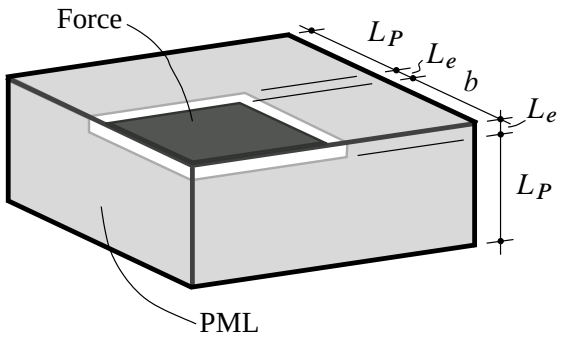

(b)

Figure 6.12. (a) Quarter-model of a half-space subjected to a uniform force applied over a square area of half-width b; (b) a PML model, fixed at the outer boundary.

notation, the characteristic length b of the PML model used in e.g., Eq. (6.37) is taken to be the depth L_P of the PML, and is not the same as the half-width b of the square area. For comparison, the half-space is also modelled using viscous dashpots [15], wherein the entire domain including the PML region is taken to be elastic and consistent dashpot elements replace the fixed outer boundary; thus the mesh used for the dashpot model is comparable to that used for the PML model. An extended-mesh model, composed entirely of elastic elements in the interior and with the same mesh density as the PML and the dashpot models, is used to provide benchmark results. This mesh extends to a distance of $25b$ downward from the center of the excitation, and laterally to a

distance of $20b$ for vertical excitation and $25b$ for horizontal excitation; the dimensions are chosen to ensure that waves reflected back from the outer boundary — modelled using viscous dashpots — do not affect the recorded displacements within the duration of the simulation.

The attenuation functions in the PML [cf. Eq. (4.2)] are chosen as $f_i^{\mathrm{e}} = f_i^{\mathrm{p}} = f_i$, with f_i now chosen to be a monomial:

$$f_i(x_i) := f_{0i} \left(\frac{x_i}{L_{Pi}} \right)^p \qquad \text{(no summation)} \tag{6.47}$$

where x_i is the distance into the PML, and L_{Pi} is the depth of the PML, in the i-th direction. A quadratic monomial ($p = 2$) is typically recommended because, in general, it expected to best ameliorate the error due to the finite-element discretisation [89, 93]; this is in contrast to a continuum PML, where a linear monomial is optimal [91].

An optimal value of the coefficient f_{0i} may be estimated from a wave-reflection analysis of a discretised one-dimensional time-harmonic PML [89], by minimising the expected reflection coefficient for a white-noise excitation. This work adopts an approach that is similar in spirit, but more directly applicable to three-dimensional problems: the optimal value of f_{0i} for a given PML depth — represented by the number of elements through the depth — for both $p = 1$ and $p = 2$, is found by minimising the expected error in the response of a canonical three-dimensional PML model over a range of values of f_{0i}. The canonical PML model is chosen to be the half-space model presented above, with shear modulus $\mu = 1$, Poisson ratio $\nu = 0.25$ and mass density $\rho = 1$, with the PML depth $L_{Pi} \equiv L_P$, and the monomial coefficient $f_{0i} \equiv f_0$ the same in all three directions, subjected to the excitation defined above, and its response characterised by the displacements at the center and at the corner of the excitation. The expected error is computed as the mean of the relative maximum error, given by Eq. (6.46) with $\boldsymbol{u}_{\mathrm{p}}$ and $\boldsymbol{u}_{\mathrm{e}}$ now representing the relevant displacement quantity of the PML and the extended-mesh model, respectively. The mean relative error is obtained by averaging the relative error in the center and corner displacements for both vertical and horizontal excitation over four different sets of excitation parameters: (a) $\omega_f = 1.5$, $t_d = 10$, (b) $\omega_f = 2.25$, $t_d = 15$, (c) $\omega_f = 3.0$, $t_d = 10$, and (d) $\omega_f = 3.75$, $t_d = 15$.

Figure 6.13 compares the minimum expected relative errors for $p = 1$ and $p = 2$ for various depths of the PML, characterised by n_P, the number of elements throught the depth of the PML. It is seen that for a PML more than 4 elements deep, there is little significant difference in accuracy between the results for the linear and quadratic attenuation function; $p = 2$ gives slightly more accurate results for depths of 4–7 elements, whereas the situation is reversed for depths of 8–12 elements. Based on these results, the numerical examples in this paper use PMLs that are 8 elements deep, with the corresponding minimizing coefficient value of $f_0 = 9.0$ and $p = 1$.

Figure 6.14 compares the displacements from the PML model and the dashpot model against those from the extended mesh, and Table 6.6 compares the relative error in the displacements computed from the two models. Note that the PML and the dashpot models are small: the PML starts at a distance of $0.2b$ from the excitation, and is only $0.8b$ deep. The results from the PML model are

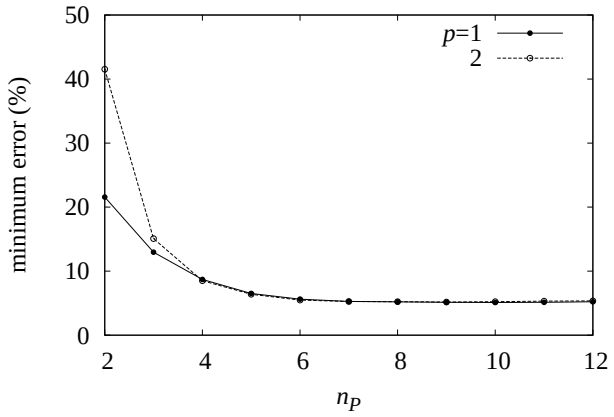

Figure 6.13. Minimum expected relative error in displacements for different numbers of elements n_P through the depth of the PML in the canonical half-space PML model, for linear and quadratic attenuation functions; $b = 1$; $L_e = 0.2b$, $L_P = 0.1bn_P$; $\mu = 1$, $\nu = 0.25$, $\rho = 1$.

visually indistinguishable from the extended mesh results, even though the domain is small enough for the dashpots to reflect waves back early in the simulation, as manifested in the higher response amplitudes and larger errors of the results from the dashpot model.

The effect of lumping of the PML matrices and the effect of PML on the critical time-step size was also studied. The time-step size required for stability of a corresponding fully-elastic model also served as a stable time-step for the PML model. Use of a consistent formulation led to a negligible decrease in the accuracy of results but a considerably reduced critical time-step size. Use of the intermediate lumped formulation resulted in a strong long-time instability in the free-vibration phase even for very small time-step sizes.

	Excitation	Center displacement		Corner displacement	
		PML	Dashpot	PML	Dashpot
%error	Vertical	4.98	45.67	6.07	85.31
	Horizontal	5.79	21.76	5.04	53.24

Box 6.6. Relative error in displacements on surface of half-space due to applied forces; $b = 1$; $L_e = 0.2b$, $L_P = 0.8b$; $\mu = 1$, $\nu = 0.25$, $\rho = 1$; $t_d = 10$, $\omega_f = 3.00$. The large errors due to the dashpot model highlight the small size of the domain.

The efficacy of the PML model may be gauged by comparing the computational costs of the three models, as presented in Table 6.7. Both the PML and the dashpot models have the same number of elements, which is significantly smaller than the number of elements in the extended mesh. However, the time-step size required for stability of the dashpot model is smaller than that of a fully-elastic model, because the dashpots introduce material damping into the system. Therefore the dashpot model required more time-steps to complete than the PML model. In order to obtain a realistic assessment of the computational cost, the dashpot model, as well as the elastic region

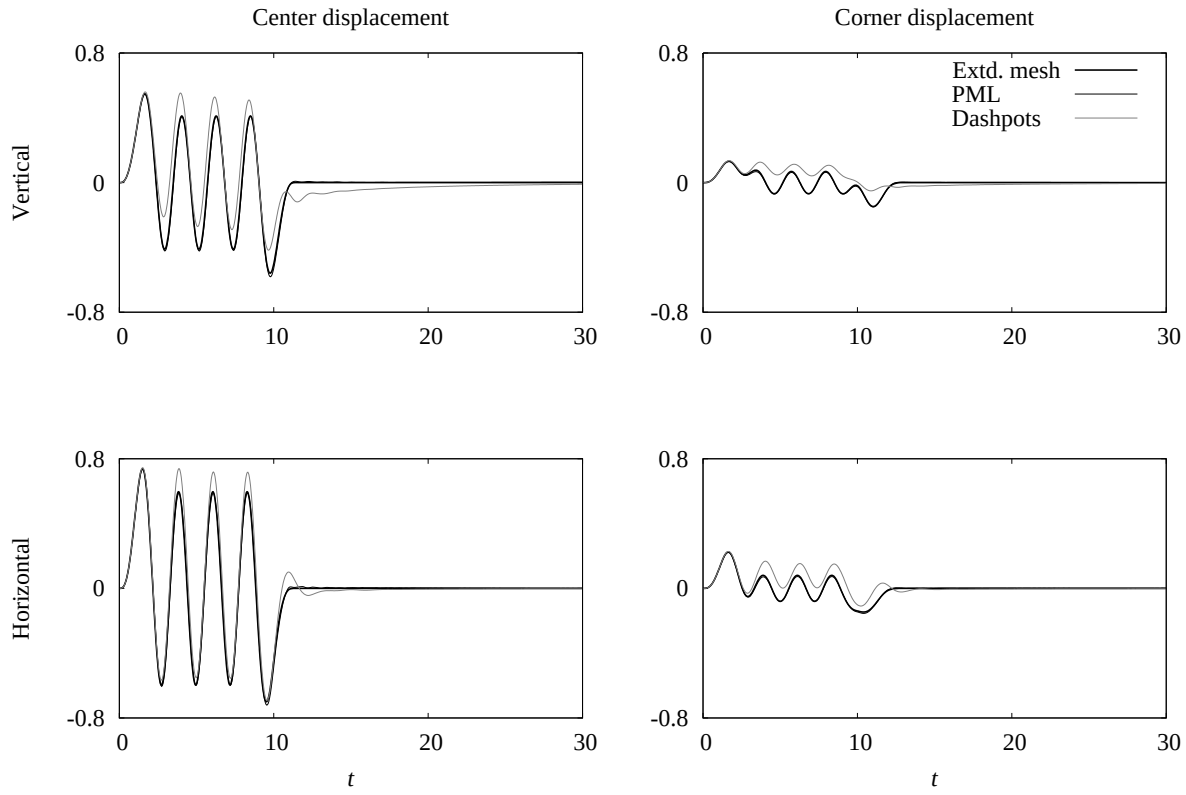

Figure 6.14. Displacements on surface of half-space due to applied forces; vertical displacements due to vertical excitation, horizontal displacements due to horizontal excitation; $b = 1$; $L_e = 0.2b$, $L_P = 0.8b$; $\mu = 1$, $\nu = 0.25$, $\rho = 1$; $t_d = 10$, $\omega_f = 3.00$. The large errors due to the dashpot model highlight the small size of the domain.

in the PML model, were discretised with under-integrated elements with hourglass control [64] as well as with fully-integrated elements; the results from the two formulations were of similar accuracy. The use of under-integrated elastic elements within the PML model did not result in any noticeable reduction of computational cost because the elastic region is much smaller than the PML region. Results for the PML and dashpot models were obtained using the explicit finite-element code LS-DYNA [94] on a desktop workstation with a 2.6GHz AMD Opteron processor, while the extended-mesh results were obtained using a specially optimised and parallelised in-house code running on 16 processors of a 32-processor node of 1.7GHz IBM Power4+ processors at the San Diego Supercomputer Center. While the differing systems make a direct comparison of the wall-clock times difficult, it is remarkable that the PML model achieves the accuracy of the extended-mesh model at a cost comparable in order to the dashpot model, several orders of magnitude smaller than the cost of the extended mesh.

Figure 6.15(a) shows a quarter-model of a layer on a half-space, with a layer of depth d with shear modulus μ_l, supported by a half-space of shear modulus μ_h, and with Poisson ratio ν and mass density ρ in both domains, and Fig. 6.15(b) shows a corresponding PML model. Note that the PML

Model	#elements	#time-steps	wall-clock time
PML	4,000	614	30.2 secs
Dashpots	4,000	876	14.4 secs (1-pt elas.) 20.6 secs (8-pt elas.)
Extd. mesh	10,140,000 (V) 15,812,500 (H)	878	35.1 proc-hrs (V) 59.3 proc-hrs (H)

Box 6.7. Comparison of computational costs of three models for a half-space. The dashpot model was discretised using both under-integrated (1-pt elas.) and fully-integrated (8-pt elas.) elastic elements. The mesh size for the extended mesh was different for vertical (V) and horizontal (H) excitations.

model must incorporate the interface between the layer and the half-space because it is a physical feature that generates wave reflections in the physical unbounded-domain model; the PML is meant to eliminate only spurious reflections from the outer boundary. The elastic moduli for the PMLs employed for the layer and the half-space are set to the moduli for the corresponding elastic media. A viscous-dashpot model is also employed for comparison, where the entire domain, including the PML region, is taken to be elastic, and consistent dashpots model the outer boundary. An extended-mesh elastic model with viscous dashpots at the outer boundary — extending laterally to a distance of $20b$ from the center of the excitation for vertical excitation and $25b$ for horizontal, and downward to $35b$ from the base of the layer — is used as a benchmark model.

Figure 6.16 shows the displacements computed from the three models, and Table 6.8 compares the errors due to the PML and the dashpot models. The results from the PML model are virtually indistinguishable from those from the extended mesh, even though the domain is small enough for the dashpot model to generate spurious reflections. The computational cost of the PML model, as shown in Table 6.9, is of the same order of magnitude as that of the dashpot model, but an insignificant fraction of the cost of the extended-mesh model. The critical time-step size for the elastic elements was adequate as a stable time-step size for the PML elements. Using the consistent formulation of the PML had little effect on the accuracy of results, but reduced the critical time-step size considerably. The intermediate lumped formulation showed a strong long-time instability in the free-vibration phase even for very small time-step sizes.

		Center displacement		Corner displacement	
	Excitation	PML	Dashpot	PML	Dashpot
%error	Vertical	6.79	27.88	8.29	51.84
	Horizontal	6.51	20.19	9.75	41.83

Box 6.8. Relative error in displacements on surface of layer on a half-space due to applied forces; $b = 1$, $d = b$; $L_e = 0.2b$, $L_P = 0.8b$; $\mu_l = 1$, $\mu_h = 2\mu_l$, $\nu = 0.25$, $\rho = 1$; $t_d = 15$, $\omega_f = 2.25$. The errors due to the dashpot model highlight the small size of the domain.

Figure 6.17(a) shows a quarter-model of a layer of depth d on a rigid base, with shear modulus μ, mass density ρ and Poisson's ratio ν, and Fig. 6.17(b) shows its PML model. The corre-

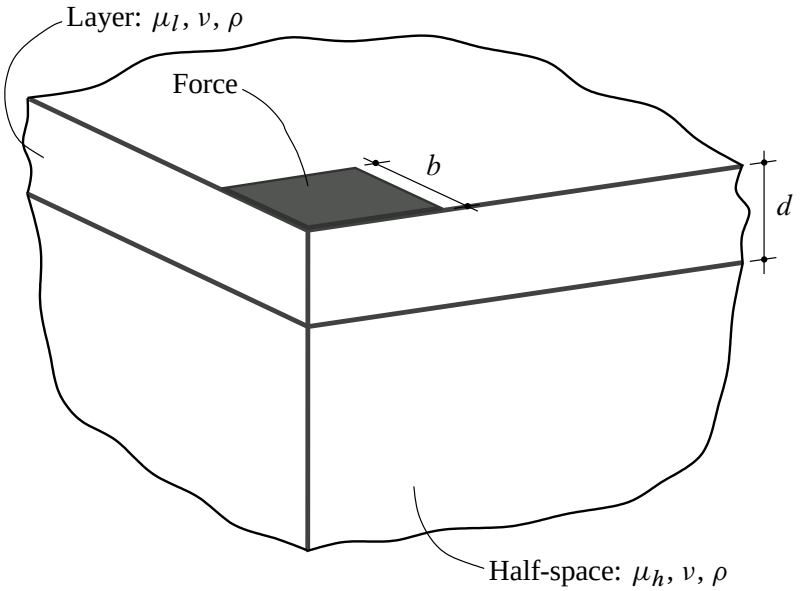

(a)

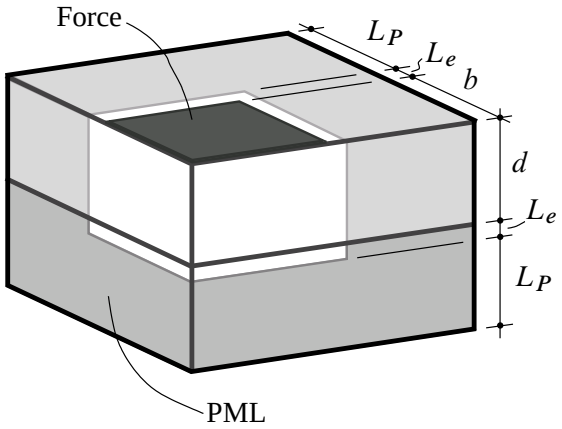

(b)

Figure 6.15. (a) Quarter-model of a layer on a half-space subjected to a uniform force applied over a square area of half-width b; (b) a PML model, fixed at the outer boundary.

sponding viscous-dashpot model is entirely elastic, with consistent dashpots replacing the fixed lateral boundaries. The benchmark extended-mesh model extends laterally to $22b$ from the center of the excitation for vertical excitation and $25b$ for horizontal. Figure 6.18 shows that the PML model produces accurate results even with a small bounded domain where the dashpot model generates spurious reflections. The PML model is able to follow the extended-mesh result in the

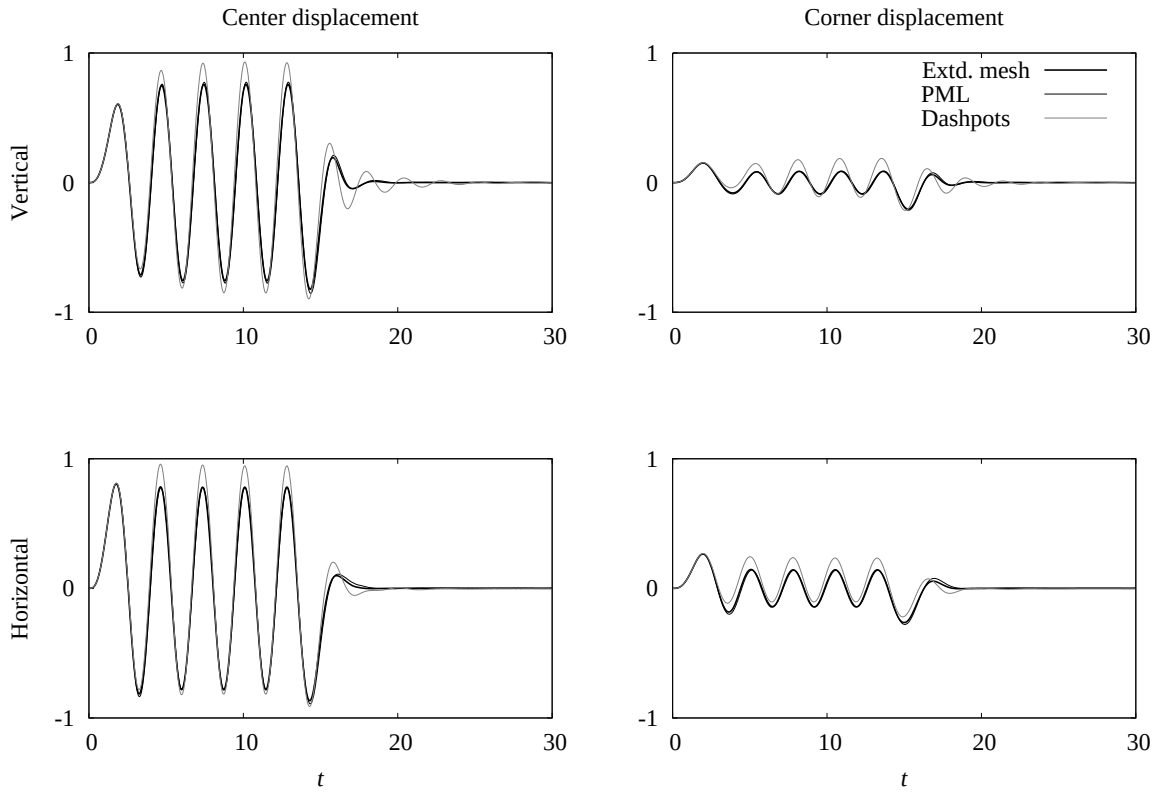

Figure 6.16. Displacements on surface of layer on a half-space due to applied forces; vertical displacements due to vertical excitation, horizontal displacements due to horizontal excitation; $b = 1$, $d = b$; $L_e = 0.2b$, $L_P = 0.8b$; $\mu_l = 1$, $\mu_h = 2\mu_l$, $\nu = 0.25$, $\rho = 1$; $t_d = 15$, $\omega_f = 2.25$. The errors due to the dashpot model highlight the small size of the domain.

Model	#elements	#time-steps	wall-clock time
PML	8,000	867	65.6 secs (1-pt elas.) 67.9 secs (8-pt elas.)
Dashpots	8,000	1,237	15.4 secs (1-pt elas.) 44.3 secs (8-pt elas.)
Extd. mesh	14,584,000 (V) 22,742,500 (H)	1,256	116.7 proc-hrs (V) 170.5 proc-hrs (H)

Box 6.9. Comparison of computational costs of three models for a layer on a half-space. The dashpot model, as well as the elastic region in the PML model, was discretised using both under-integrated (1-pt elas.) and fully-integrated (8-pt elas.) elastic elements. The mesh size for the extended mesh was different for vertical (V) and horizontal (H) excitations.

free-vibration phase of the displacements from horizontal excitation — in the direction of unboundedness of the domain — when the results from the dashpot model are entirely inadequate; this is reflected in the comparison in Table 6.10 of errors due to either model. The slight phase

difference between the PML and the extended-mesh results in the free-vibration phase may be due to evanescent waves not being entirely attenuated [79]. Table 6.11 shows that the PML model is able to achieve this accuracy at a cost that is of the same order of magnitude as that of the dashpot model, and at a small fraction of the cost of the extended-mesh model. The effect of lumping of the PML matrices and the effect of PML on the critical time-step size was similar to that observed for the half-space and layer-on-half-space models.

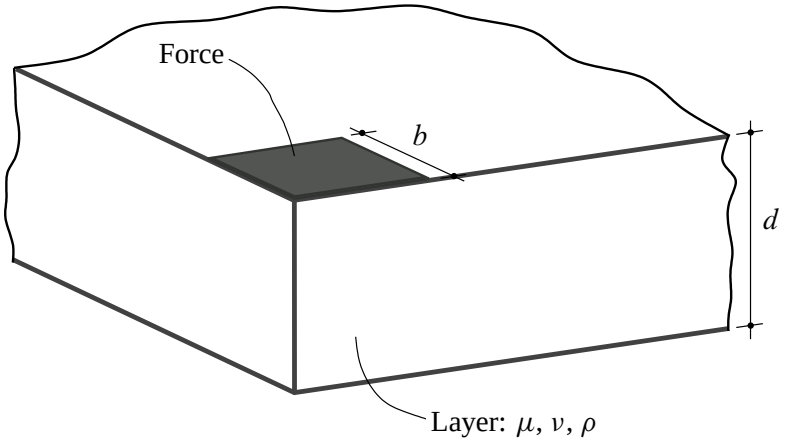

(a)

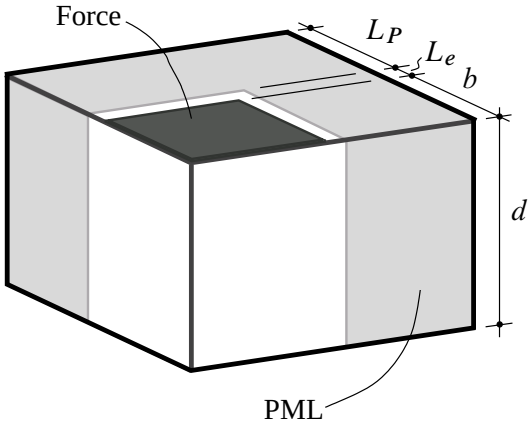

(b)

Figure 6.17. (a) Quarter-model of a layer on a rigid base subjected to a uniform force applied over a square area of half-width b; (b) a PML model, fixed at the outer boundary.

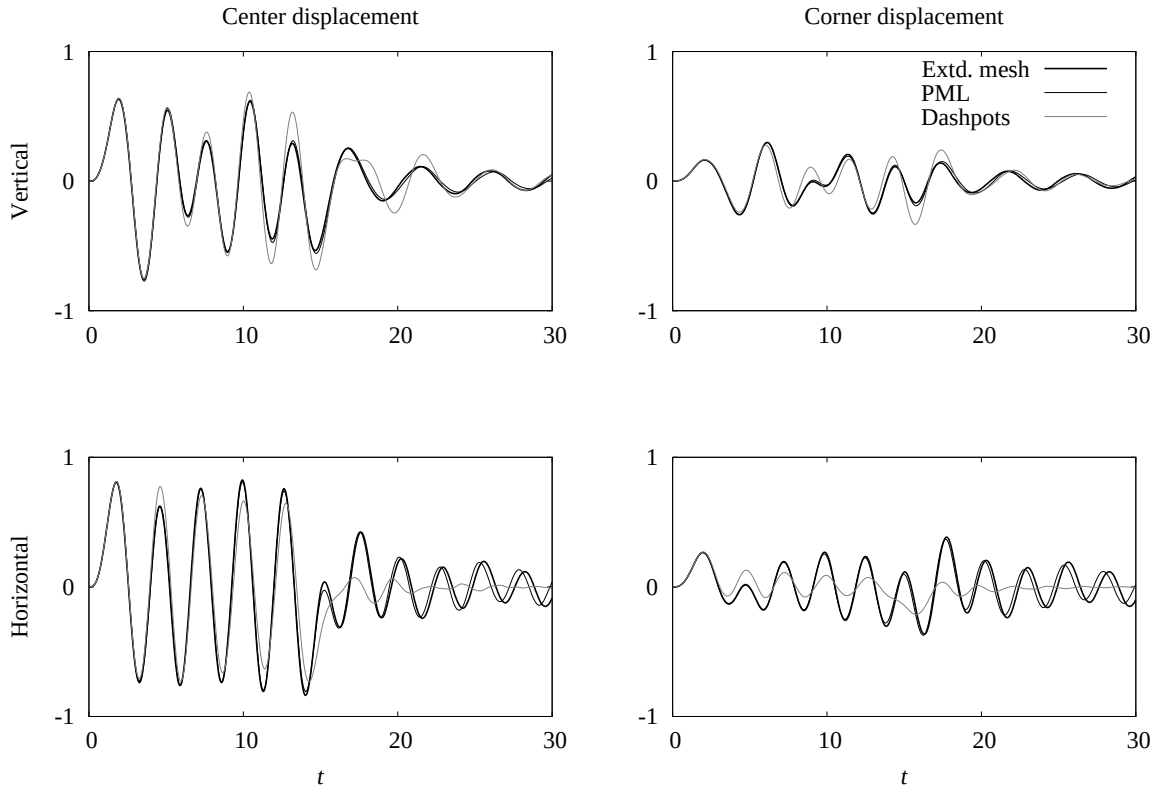

Figure 6.18. Displacements on surface of layer on rigid base due to applied forces; vertical displacements due to vertical excitation, horizontal displacements due to horizontal excitation; $b = 1$, $d = 2b$; $L_e = 0.2b$, $L_P = 0.8b$; $\mu = 1$, $\nu = 0.25$, $\rho = 1$; $t_d = 15$, $\omega_f = 2.25$. The large errors due to the dashpot model highlight the small size of the domain.

	Excitation	Center displacement		Corner displacement	
		PML	Dashpot	PML	Dashpot
%error	Vertical	6.67	31.81	11.25	56.62
	Horizontal	15.00	48.30	30.85	94.86

Box 6.10. Relative error in displacements on surface of layer on rigid base due to applied forces; $b = 1$, $d = 2b$; $L_e = 0.2b$, $L_P = 0.8b$; $\mu = 1$, $\nu = 0.25$, $\rho = 1$; $t_d = 15$, $\omega_f = 2.25$. The large errors due to the dashpot model highlight the small size of the domain.

Model	#elements	#time-steps	wall-clock time
PML	8,000	614	45.3 secs (1-pt elas.) 50.5 secs (8-pt elas.)
Dashpots	8,000	828	10.5 secs (1-pt elas.) 31.9 secs (8-pt elas.)
Extd. mesh	976,800 (V) 1,260,000 (H)	812	4.7 proc-hrs (V) 5.9 proc-hrs (H)

Box 6.11. Comparison of computational costs of three models for a layer on rigid base. The dashpot model, as well as the elastic region in the PML model, was discretised using both under-integrated (1-pt elas.) and fully-integrated (8-pt elas.) elastic elements. The mesh size for the extended mesh was different for vertical (V) and horizontal (H) excitations.

7 CONCLUSIONS

This report has developed the concept of a PML for elastic waves by utilising insights obtained in the context of electromagnetics. The concept has been developed through the presentation of PMLs for: (1) a rod on elastic foundation, (2) acoustic waves in two and three dimensions, and (3) elastic waves in two and three dimensions.

The PML concept is summarised as follows. A perfectly matched medium (PMM) is defined as one governed by a modification of the equations for the elastic medium, with the modification motivated by a continuous, complex-valued, uncoupled coordinate stretching. Solutions admitted by the PMM are of the form of those admitted by the elastic medium, but with the stretched coordinates replacing the real coordinates. PMMs exhibit the perfect matching property: if the stretching functions of two adjacent PMMs match at their interface, then the interface is invisible to all wave-type solutions in the PMMs and no reflected wave is generated when a wave travels from one PMM to the other. This property holds irrespective of the direction of propagation of the wave or its frequency. Furthermore, if choices of the stretching functions are appropriate, the solutions in the PMM take the form of the corresponding elastic medium solution, but with an imposed spatial attenuation. Realistic choices of the stretching function can impose attenuation on both propagating and evanescent waves. Notably, the imposed attenuation is directly spatial: it is not imposed through a temporal attenuation, or damping. The perfect matching and the attenuative properties of the PMM is employed to build an absorbing layer — the PML — around a bounded domain such that the layer absorbs and attenuates outward-propagating waves of all non-tangential angles-of- incidence and of all non-zero frequencies. Termination of the layer by a fixed boundary causes reflection of the waves back towards the bounded domain, with the amplitude of reflected waves controllable — independently of the size of the bounded domain — by the choice of the PML parameters: (a) the depth of the layer and (b) the attenuation profile in it. Thus, wave propagation in an unbounded domain can be modelled through a bounded domain that is restricted to the region of interest in the analysis, and a suitably-defined PML surrounding it.

Although the PML is fundamentally formulated in the frequency domain, corresponding time-domain formulations are obtained by selecting stretching functions in the PML that have a simple dependence on the factor $\mathrm{i}\omega$, which facilitates transformation of the time-harmonic equations into the time domain. In the interest of obtaining a realistic model of the unbounded domain, material damping is introduced into the PML equations in the form of a Voigt damping model in the constitutive relation for the PML, although a causal hysteretic model [95–97] can be used as well.

The PML formulations are implemented numerically by a straightforward finite element approach. In the frequency-domain, the FE matrices obtained are symmetric, but intrinsically complex-valued and frequency-dependent. Thus the system matrices for the entire bounded domain are complex, symmetric and banded, the PML contributions to which have to be computed anew for each fre-

quency. In the time-domain, although the tangent stiffness for the acoustic PML is symmetric, unfortunately the stiffness for the elastic PML turns out to be unsymmetric. While this is not overly demanding for two-dimensional problems, it becomes difficult to solve a large system of unsymmetric equations for three-dimensional elastic problems. Consequently, the three-dimensional elastic PML is made suitable for explicit time-integration, and an efficient method of computing the strain terms in the PML is developed to take advantage of the lack of overhead of solving equations.

The acoustic PML models have been numerically validated for the classical problem of an acoustic waveguide, which is representative of the reservoir behind the dam. The elastic PML models have been numerically validated for the classical soil-structure interaction problems of a footing on a (i) half-space, (ii) layer on a half-space, and (iii) layer on a rigid base. The PML models — typically 8–10 elements deep — gave highly accurate results, even though the domains were small enough that comparably-sized viscous-dashpot models generated spurious wave reflections early on in the duration of the simulation. The computational cost of the PML models was comparable in order to that of the dashpot models, but was an insignificant fraction of the cost of the corresponding extended-mesh models used as benchmarks for the time-domain problems. For the explicit PML, it was found that the time-step size for a PML element is similar to that for a corresponding elastic element, and that lumping the intertial matrices did not significantly affect the accuracy of results. Furthermore, it has been verified numerically that this PML model is stable not only in the long time in free vibration, but even if it is excited over a long duration.

These PML models thus provide an accurate and inexpensive absorbing boundary model for modelling the foundation rock and impounded water in the earthquake analysis of dams, and will hopefully lead to realistic and accurate evaluation of the earthquake safety of new or existing dams.

REFERENCES

1. Givoli D. *Numerical Methods for Problems in Infinite Domains*. Elsevier: Amsterdam, 1992.
2. Tsynkov SV. Numerical solution of problems on unbounded domains. A review. *Applied Numerical Mathematics* 1998; **27**(4):465–532.
3. Bao H, Bielak J, Ghattas O, Kallivokas LF, O'Hallaron DR, Shewchuck JR, Xu J. Large-scale simulation of elastic wave propagation in heterogeneous media on parallel computers. *Computer Methods in Applied Mechanics and Engineering* 1998; **152**(1–2):85–102.
4. Bielak J, Loukakis K, Hisada Y, Yoshimura C. Domain reduction method for three-dimensional earthquake modeling in localized regions, Part I: Theory. *Bulletin of the Seismological Society of America* 2003; **93**(2):817–824.
5. Wolf JP. *Dynamic Soil-Structure Interaction*. Prentice-Hall: Englewood Cliffs, NJ, 1985.
6. Wolf JP. *Soil-Structure-Interaction Analysis in Time Domain*. Prentice-Hall: Englewood Cliffs, NJ, 1988.
7. Chew WC. *Waves and Fields in Inhomogenous Media*. IEEE Press: Piscataway, NJ, 1995.
8. Park YH, Park KC. High-fidelity modeling of MEMS resonators — Part I: Anchor loss mechanisms through substrate. *Journal of Microelectromechanical Systems* 2004; **13**(2):238–247.
9. Alonso-Mallo I, Reguera N. Discrete absorbing boundary conditions for Schrödinger-type equations. Construction and error analysis. *SIAM Journal on Numerical Analysis* 2003; **41**(5):1824–1850.
10. Clough RW, Chopra AK, Dreher KJ, Fenves GL, Hall JF, Mau ST. Earthquake engineering for concrete dams: Design, performance, and research needs. National Research Council, Panel on Earthquake Engineering for Concrete Dams, National Academy Press, Washington D. C., 1990.
11. Manolis GD, Beskos DE. *Boundary Element Methods in Elastodynamics*. Unwin Hyman: London, 1988.
12. Givoli D, Keller JB. Non-reflecting boundary conditions for elastic waves. *Wave Motion* 1990; **12**(3):261–279.
13. Givoli D, Vigdergauz S. Artificial boundary conditions for 2D problems in geophysics. *Computer Methods in Applied Mechanics and Engineering* 1993; **110**(1–2):87–101.
14. Song C, Wolf JP. The scaled boundary finite-element method — alias consistent infinitesimal finite-element cell method — for elastodynamics. *Computer Methods in Applied Mechanics and Engineering* 1997; **147**(3–4):329–355.
15. Lysmer J, Kuhlemeyer RL. Finite dynamic model for infinite media. *Journal of the Engineering Mechanics Division, ASCE* 1969; **95**(EM4):859–877.
16. Clayton R, Engquist B. Absorbing boundary conditions for acoustic and elastic wave equations. *Bulletin of the Seismological Society of America* 1977; **67**(6):1529–1540.

17. Higdon RL. Absorbing boundary conditions for elastic waves. *Geophysics* 1991; **56**(2):231–241.
18. Israil ASM, Banerjee PK. Advanced time-domain formulation of BEM for two-dimensional transient elastodynamics. *International Journal for Numerical Methods in Engineering* 1990; **29**(7):1421–1440.
19. Grote MJ, Keller JB. Exact nonreflecting boundary condition for elastic waves. *SIAM Journal on Applied Mathematics* 2000; **60**(3):803–819.
20. Wolf JP, Song C. Consistent infinitesimal finite-element cell method: in-plane motion. *Computer Methods in Applied Mechanics and Engineering* 1995; **123**(1–4):355–370.
21. Liao ZP, Wong HL. A transmitting boundary for the numerical simulation of elastic wave propagation. *Soil Dynamics and Earthquake Engineering* 1984; **3**(4):174–183.
22. Guddati MN, Tassoulas JL. Continued-fraction absorbing boundary conditions for the wave equation. *Journal of Computational Acoustics* 2000; **8**(1):139–156.
23. Givoli D, Keller JB. Special finite elements for use with high-order boundary conditions. *Computer Methods in Applied Mechanics and Engineering* 1994; **119**(3–4):199–213.
24. Givoli D. High-order nonreflecting boundary conditions without high-order derivatives. *Journal of Computational Physics* 2001; **170**(2):849–870.
25. Givoli D. High-order local non-reflecting boundary conditions: a review. *Wave Motion* 2004; **39**(4):319–326.
26. Hagstrom T, Warburton T. A new auxiliary variable formulation of high-order local radiation boundary conditions: corner compatibility conditions and extensions to first-order systems. *Wave Motion* 2004; **39**(4):327–338.
27. Givoli D, Hagstrom T, Patlashenko I. Finite element formulation with high-order absorbing boundary conditions for time-dependent waves. *Computer Methods in Applied Mechanics and Engineering* 2006; **195**(29–32):3666–3690.
28. Israeli M, Orszag SA. Approximation of radiation boundary conditions. *Journal of Computational Physics* 1981; **41**(1):115–135.
29. Cerjan C, Kosloff D, Kosloff R, Reshef M. A nonreflecting boundary-condition for discrete acoustic and elastic wave-equations. *Geophysics* 1985; **50**(4):705–708.
30. Sochaki J, Kubichek R, George J, Fletcher WR, Smithson S. Absorbing boundary conditions and surface waves. *Geophysics* 1987; **52**(1):60–71.
31. Furumura T, Takenaka H. A wraparound elimination technique for the pseudospectral wave synthesis using an antiperiodic extension of the wavefield. *Geophysics* 1995; **60**(1):302–307.
32. Smith WD. A nonreflecting plane boundary for wave propagation problems. *Journal of Computational Physics* 1974; **15**(4):492–503.
33. Yerli HR, Temel B, Kiral E. Transient infinite elements for 2D soil-structure interaction anlysis. *Journal of Geotechnical and Geoenvironmental Engineering* 1998; **124**(10):976–988.
34. Kim DK, Yun CB. Time-domain soil-structure interaction analysis in two-dimensional medium based on analytical frequency-dependent infinite elements. *International Journal for Numerical Methods in Engineering* 2000; **47**(7):1241–1261.

35. Kawamoto JD. Solution of nonlinear dynamic structural systems by a hybrid frequency–time-domain approach. Research Report R 83-5, Department of Civil Engineering, Massachusetts Institute of Technology, Cambridge, MA, 1983.

36. Seed HB, Idriss IM. Influence of soil conditions on ground motions during earthquakes. *Journal of the Soil Mechanics and Foundations Division, ASCE* 1969; **94**(SM1):99–137.

37. Wolf JP. Consistent lumped-parameter models for unbounded soil: Physical representation. *Earthquake Engineering and Structural Dynamics* 1991; **20**(1):11–32.

38. Feltrin G. Absorbing bondaries for the time-domain analysis of dam-reservoir-foundation systems. IBK Bericht Nr. 232, Institute of Structural Engineering, Swiss Federal Institute of Technology Zürich, Birkhaüser Verlag, Basel, 1997.

39. Ruge P, Trinks C, Witte S. Time-domain analysis of unbounded media using mixed-variable fomrulations. *Earthquake Engineering and Structural Dynamics* 2001; **30**(6):899–925.

40. Bérenger JP. A perfectly matched layer for the absorption of electromagnetic waves. *Journal of Computational Physics* 1994; **114**(2):185–200.

41. Chew WC, Weedon WH. A 3D perfectly matched medium from modified Maxwell's equations with stretched coordinates. *Microwave and Optical Technology Letters* 1994; **7**(13):599–604.

42. Qi Q, Geers TL. Evaluation of the perfectly matched layer for computational acoustics. *Journal of Computational Physics* 1998; **139**(1):166–183.

43. Turkel E, Yefet A. Absorbing PML boundary layers for wave-like equations. *Applied Numerical Mathematics* 1998; **27**(4):533–557.

44. Harari I, Slavutin M, Turkel E. Analytical and numerical studies of a finite element PML for the Helmholtz equation. *Journal of Computational Acoustics* 2000; **8**(1):121–137.

45. Hu FQ. On absorbing boundary conditions for linearized Euler equations by a perfectly matched layer. *Journal of Computational Physics* 1996; **129**(1):201–219.

46. Zeng YQ, He JQ, Liu QH. The application of the perfectly matched layer in numerical modeling of wave propagation in poroelastic media. *Geophysics* 2001; **66**(4):1258–1266.

47. Chew WC, Liu QH. Perfectly matched layers for elastodynamics: A new absorbing boundary condition. *Journal of Computational Acoustics* 1996; **4**(4):341–359.

48. Hastings FD, Schneider JB, Broschat SL. Application of the perfectly matched layer (PML) absorbing boundary condition to elastic wave propagation. *Journal of the Acoustical Society of America* 1996; **100**(5):3061–3069.

49. Liu QH. Perfectly matched layers for elastic waves in cylindrical and spherical coordinates. *Journal of the Acoustical Society of America* 1999; **105**(4):2075–2084.

50. Zhang YG, Ballmann J. Two techniques for the absorption of elastic waves using an artificial transition layer. *Wave Motion* 1997; **25**(1):15–33.

51. Collino F, Tsogka C. Application of the perfectly matched absorbing layer model to the linear elastodynamic problem in anisotropic heterogeneous media. *Geophysics* 2001; **66**(1):294–307.

52. Bécache E, Joly P, Tsogka C. Fictitious domains, mixed finite elements and perfectly matched layers for 2-D elastic wave propagation. *Journal of Computational Acoustics* 2001; **9**(3):1175–1201.

53. Festa G, Nielsen S. PML absorbing boundaries. *Bulletin of the Seismological Society of America* 2003; **93**(2):891–903.

54. Komatitsch D, Tromp J. A perfectly matched layer absorbing boundary condition for the second-order seismic wave equation. *Geophysical Journal International* 2003; **154**(1):146–153.

55. Marcinkovich C, Olsen K. On the implementation of perfectly matched layers in a three-dimensional fourth-order velocity-stress finite difference scheme. *Journal of Geophysical Research* 2003; **108**(B5):2276.

56. Ma S, Liu P. Modeling of the perfectly matched layer absorbing boundaries and intrinsic attenuation in explicit finite-element methods. *Bulletin of the Seismological Society of America* 2006; **96**(5):1779–1794.

57. Wang T, Tang X. Finite-difference modeling of elastic wave propagation: A nonsplitting perfectly matched layer approach. *Geophysics* 2003; **68**(5):1749–1755.

58. Cohen G, Fauqueux S. Mixed spectral finite elements for the linear elasticity system in unbounded domains. *SIAM Journal on Scientific Computing* 2005; **26**(3):864–884.

59. Festa G, Vilotte JP. The Newmark scheme as velocity-stress time-staggering: an efficient PML implementation for spectral element simulations of elastodynamics. *Geophysical Journal International* 2005; **161**(3):789–812.

60. Harari I, Albocher U. Studies of FE/PML for exterior problems of time-harmonic elastic waves. *Computer Methods in Applied Mechanics and Engineering* 2006; **195**(29–32):3854–3879.

61. Appelö D, Kreiss G. A new absorbing layer for elastic waves. *Journal of Computational Physics* 2006; **215**(2):642–660.

62. Komatitsch D, Martin R. An unsplit convolutional perfectly matched layer improved at grazing incidence for the seismic wave equation. *Geophysics* 2007; **72**(5):SM155–SM167.

63. Zienkiewicz OC, Taylor RL, Zhu JZ. *The Finite Element Method: Its Basis and Fundamentals* (6th edn). Elsevier Butterworth-Heinemann, 2005.

64. Belytschko T, Liu WK, Moran B. *Nonlinear Finite Elements for Continua and Structures*. Wiley, 2000.

65. Hughes TJR. *The Finite Element Method: Linear Static and Dynamic Finite Element Analysis*. Dover: NY, 2000.

66. Chew WC, Jin JM, Michielssen E. Complex coordinate stretching as a generalized absorbing boundary condition. *Microwave and Optical Technology Letters* 1997; **15**(6):363–369.

67. Teixeira FL, Chew WC. Unified analysis of perfectly matched layers using differential forms. *Microwave and Optical Technology Letters* 1999; **20**(2):124–126.

68. Teixeira FL, Chew WC. A general approach to extend Bérenger's absorbing boundary condition to anisotropic and dispersive media. *IEEE Transactions on Antennas and Propagation* 1998; **46**(9):1386–1387.
69. Bland DR. *The Theory of Linear Viscoelasticity*. Pergamon Press, 1960.
70. Zhao L, Cangellaris AC. A general approach for the development of unsplit-field time-domain implementations of perfectly matched layers for FDTD grid truncation. *IEEE Microwave and Guided Wave Letters* 1996; **6**(5):209–211.
71. Zienkiewicz OC, Taylor RL. *The Finite Element Method* (5th edn). Butterworth-Heinemann: New York, 2000.
72. Newmark NM. A method of computation for structural dynamics. *Journal of the Engineering Mechanics Division, ASCE* 1959; **85**(EM3):67–94.
73. Chopra AK. *Dynamics of Structures: Theory and Applications to Earthquake Engineering* (2nd edn). Prentice-Hall: Englewood Cliffs, NJ, 2001.
74. Collino F, Monk PB. The perfectly matched layer in curvilinear coordinates. *SIAM Journal on Scientific Computing* 1998; **19**(6):2061–2090.
75. De Moerloose J, Stuchly MA. Behaviour of Bérenger's ABC for evanescent waves. *IEEE Microwave and Guided Wave Letters* 1995; **5**(10):344–346.
76. Bérenger JP. Application of the CFS PML to the absorption of evanescent waves in waveguides. *IEEE Microwave and Wireless Components Letters* 2002; **12**(6):218–220.
77. Fenves G, Chopra AK. Effects of reservoir bottom absorption on earthquake response of concrete gravity dams. *Earthquake Engineering and Structural Dynamics* 1983; **11**(6):809–829.
78. Hall JF, Chopra AK. Dynamic analysis of arch dams including hydrodynamic effects. *Journal of Engineering Mechanics* 1983; **109**(1):149–167.
79. Basu U, Chopra AK. Perfectly matched layers for transient elastodynamics of unbounded domains. *International Journal for Numerical Methods in Engineering* 2004; **59**(8):1039–1074. Erratum: Ibid. 2004; **61**(1):156–157.
80. Graff KF. *Wave Motion in Elastic Solids*. Dover: NY, 1975.
81. Luco JE, Westmann RA. Dynamic response of a rigid footing bonded to an elastic half space. *Journal of Applied Mechanics, ASME* 1972; **39**(2):527–534.
82. Gazetas G. Importance of soil anisotropy on foundation displacement functions. In *Advances in Geotechnical Earthquake Engineering*, vol. 3. University of Missouri, Rolla, 1981; 1039–1046.
83. Gazetas G, Roësset JM. Vertical vibration of machine foundations. *Journal of the Geotechnical Engineering Division, ASCE* 1979; **105**(12):1435–1454.
84. Gazetas G, Roësset JM. Forced vibrations of strip footings on layered soils. In *Methods of Structural Analysis*, vol. 1. ASCE, 1976; 115–131.
85. Luco JE, Westmann RA. Dynamic response of circular footings. *Journal of the Engineering Mechanics Division, ASCE* 1971; **97**(EM5):1381–1395.

86. Veletsos AS, Verbič B. Vibration of viscoelastic foundations. *Earthquake Engineering and Structural Dynamics* 1973; **2**:87–102.
87. Luco JE. Vibrations of rigid disc on a layered viscoelastic medium. *Nuclear Engineering and Design* 1976; **36**:325–340.
88. Kausel E, Roësset JM. Dynamic stiffness of circular foundations. *Journal of the Engineering Mechanics Division, ASCE* 1975; **101**(EM6):771–785.
89. Bindel DS, Govindjee S. Elastic PMLs for resonator anchor loss simulation. *International Journal for Numerical Methods in Engineering* 2005; **64**(6):789–818.
90. Makris N. Causal hysteretic element. *Journal of Engineering Mechanics, ASCE* 1997; **123**(11):1209–1214.
91. Basu U, Chopra AK. Perfectly matched layers for time-harmonic elastodynamics of unbounded domains: theory and finite-element implementation. *Computer Methods in Applied Mechanics and Engineering* 2003; **192**(11–12):1337–1375.
92. Krieg RD, Key SW. Transient shell response by numerical time integration. *International Journal for Numerical Methods in Engineering* 1973; **7**(3):242–411.
93. Collino F, Monk PB. Optimizing the perfectly matched layer. *Computer Methods in Applied Mechanics and Engineering* 1998; **164**(1):157–171.
94. Hallquist JO. *LS-DYNA Keyword User's Manual, Version 971*. Livermore Software Technology Corporation, Livermore, CA, 2007.
95. Spanos PD, Tsavachidis S. Deterministic and stochastic analyses of a nonlinear system with a biot visco-elastic element. *Earthquake Engineering and Structural Dynamics* 2001; **30**(4):595–512.
96. Makris N, Zhang J. Time-domain viscoelastic analysis of earth structures. *Earthquake Engineering and Structural Dynamics* 2000; **29**(6):745–768.
97. Muscolini G, Palmeri A, Ricciardelli F. Time-domain response of linear hysteretic systems to deterministic and random excitations. *Earthquake Engineering and Structural Dynamics* 2005; **34**(9):1129–1147.

NOTATION

Roman symbols

a_0	non-dimensional frequency
$\boldsymbol{a}$	nodal accelerations
A	cross-sectional area of elastic rod
b	half-width of footing
$\mathbf{B}$, $\tilde{\mathbf{B}}$, $\tilde{\mathbf{B}}^{\mathrm{e}}$, $\tilde{\mathbf{B}}^{\mathrm{p}}$, $\mathbf{B}^{\epsilon}$, $\mathbf{B}^{\varrho}$, $\tilde{\mathbf{B}}^{\mathrm{ee}}$, $\tilde{\mathbf{B}}^{\mathrm{ep}}$, $\tilde{\mathbf{B}}^{\mathrm{pp}}$	compatibility matrices
c	damping coefficient of $\bar{S}$, $\bar{S}^{\infty}$
c_l	wave speed in elastic rod
c_p	P-wave speed
c_s	S- or shear-wave speed
c_v	Love wave speed
$\mathbf{c}^e$, $\check{\mathbf{c}}^e$, $\mathbf{c}$, $\check{\mathbf{c}}$	element-level and global damping matrices
$\mathbf{C}$, C_{ijkl}	material stiffness tensor
d	depth of layer
$\boldsymbol{d}$	nodal displacements
$\mathbf{D}$	material moduli matrix
$\mathfrak{D}$	time-integral of $\boldsymbol{d}$
$\{\boldsymbol{e}_i\}$	standard orthonormal basis
E, E^*	Young's modulus
$\mathbf{E}$, $\hat{\mathbf{E}}$	time integral of $\boldsymbol{\varepsilon}$, $\hat{\boldsymbol{\varepsilon}}$
f, $\bar{f}$, f_i, f^{e}, f^{p}, f_i^{e}, f_i^{p}	attenuation function(s)
f_0	coefficient of monomial in f_i^{e}, f_i^{p}
f_{m}, f_{c}, f_{k}	see Eq. (4.8)
$\boldsymbol{f}^e$	element-level internal force term
$\boldsymbol{f}_{\mathrm{int}}^e$, $\boldsymbol{f}_{\mathrm{int}}$, $\boldsymbol{f}_{\mathrm{ext}}$	internal and external force terms
F	force on acoustic waveguide
F, $\bar{F}$, F_i, $\bar{F}^{\mathrm{e}}$, $\bar{F}^{\mathrm{p}}$	integrals of f, $\bar{f}$, f_i, f^{e}, f^{p}
F_{ij}	flexibility coefficient of rigid strip-footing, with $i, j \in \{V, H, R\}$
$\mathbf{F}^{\mathrm{e}}$, $\mathbf{F}^{\mathrm{p}}$, $\tilde{\mathbf{F}}^{\mathrm{e}}$, $\tilde{\mathbf{F}}^{\mathrm{p}}$, $\tilde{\mathbf{F}}^{\mathrm{ee}}$, $\tilde{\mathbf{F}}^{\mathrm{ep}}$, $\tilde{\mathbf{F}}^{\mathrm{pp}}$	attenuation tensors; Eq. (4.4), (4.25)
$\mathbf{F}^{\infty}$	dynamic flexibility matrix of rigid strip-footing
H	(in subscript) horizontal DOF of rigid strip-footing
$\mathrm{i} = \sqrt{-1}$	unit imaginary number

Im	imaginary part of a complex number
$\mathbf{I}$	identity matrix
$\mathcal{J}$	Jacobian determinant of coordinate stretch
k	stiffness coefficient of $\bar{S}$, $\bar{S}^{\infty}$
k_g, k_g^*	static stiffness per unit length of (visco-)elastic foundation of rod
k_p, k_s, k_s^*, k_v	wavenumbers for P, S, and Love waves
$\mathbf{k}_{IJ}^e$	nodal submatrix of element stiffness matrix
$\mathbf{k}^e$, $\check{\mathbf{k}}^e$, $\mathbf{k}$	element-level and global stiffness matrices
$\mathbf{K}^e$, $\mathbf{K}$	element-level and global coefficient matrices of $\mathfrak{D}$
L	length of bounded medium
L_e	depth of elastic medium
L_P, L_{Pi}	depth of PML
$\mathbf{m}_{IJ}^e$	nodal submatrix of element mass matrix
$\mathbf{m}^e$, $\mathbf{m}$	element-level and global mass matrices
n_c	number of full cycles in imposed displacement
$\boldsymbol{n}$	unit normal to a surface
$\boldsymbol{N}$, N_I, $\mathbf{N}_d$	nodal shape functions
$\boldsymbol{q}$	direction of particle motion
$\mathbf{Q}$, Q_{ij}	rotation-of-basis matrix
r_0	characteristic length quantity for the rod on elastic foundation
$\boldsymbol{r}$, r_i	direction of wave propagtion
R	(in subscript) rocking DOF of rigid strip-footing
$\lvert R\rvert$, $\lvert R_{pp}\rvert$, $\lvert R_{sp}\rvert$	amplitude(s) of wave(s) reflected from the PML
Re	real part of a complex number
$\bar{S}$	non-dimensional dynamic stiffness of bounded rod
$\bar{S}^{\infty}$	non-dimensional dynamic stiffness of unbounded rod
S_{ij}	component of dynamic stiffness matrix of layer on rigid base
$\mathbf{S}^{\infty}$	dynamic stiffness matrix of layer on rigid base
t_d	duration of applied force
u, u_i, $\boldsymbol{u}$	displacement(s)
$\boldsymbol{U}$	time-integral of $\boldsymbol{u}$
V	(in subscript) vertical DOF of rigid strip-footing
w, w_i, $\boldsymbol{w}$	arbitrary weighting function in weak form
x, x_i, $\boldsymbol{x}$	real coordinate(s)
$\tilde{x}$, $\tilde{x}_i$, $\tilde{\boldsymbol{x}}$	complex stretched coordinate(s)

Greek symbols

γ,$\boldsymbol{\gamma}$	internal variable in acoustic formulation
δ_{ij}	Kronecker delta
Δ	differential operator

Δt	time-step size
ε, ε_{ij}, $\boldsymbol{\varepsilon}$, $\hat{\boldsymbol{\varepsilon}}$	strain quantities
ε'_{ij}, $\boldsymbol{\varepsilon}'$	strain quantities in PML basis
ζ	hysteretic damping ratio for visco-elastic medium
θ	angle of incidence of outgoing wave on PML
κ, κ^*	bulk modulus
λ, λ_i	complex coordinate stretching function(s)
$\boldsymbol{\Lambda}$, Λ_{ij}	stretch tensor
μ, μ^*	shear modulus
ν	Poisson's ratio
ρ	mass density
σ, σ_{ij}, $\boldsymbol{\sigma}$, $\hat{\boldsymbol{\sigma}}$, $\tilde{\boldsymbol{\sigma}}$	stress quantities
$\boldsymbol{\Sigma}$, $\hat{\boldsymbol{\Sigma}}$	time-integral of $\boldsymbol{\sigma}$, $\hat{\boldsymbol{\sigma}}$
$\tilde{\boldsymbol{\Sigma}}$, $\hat{\tilde{\boldsymbol{\Sigma}}}$	time-integral of $\boldsymbol{\Sigma}$, $\hat{\boldsymbol{\Sigma}}$
φ, $\boldsymbol{\varphi}$	internal variable in acoustic formulation
ω	excitation frequency
ω_f	dominant forcing frequency of imposed displacement
Ω	entire bounded domain used for computation
Ω^e	element domain
Ω_{BD}	elastic domain
Ω_{PM}	perfectly matched layer (PML)
$\Omega_{\mathrm{PM}}^{\infty}$	unbounded perfectly matched medium (PMM)

APPENDIX A: IMPOSED DISPLACEMENT FOR TRANSIENT ANALYSIS

Described here is the waveform employed as the imposed displacement in the numerical examples in this report. The waveform is in the form of a time-limited cosine wave, bookended by cosine half-cycles so that the initial displacement and velocity as well as the final displacement and velocity are zero. It is characterised by two parameters: the duration t_d and the dominant forcing frequency ω_f; the dominant forcing period is then

$$T_f = \frac{2\pi}{\omega_f}$$

and the number of full cycles, n_c, in the excitation is calculated as

$$n_c = \left[\frac{t_d}{T_f} - \frac{1}{2}\right] \tag{A1}$$

where the $1/2$ accounts for the cosine half-cycle used to end the excitation. For consistency, the forcing period is adjusted to

$$T_f := \frac{t_d}{n_c + 1/2} \tag{A2}$$

The excitation is then defined as

$$\begin{aligned} u_0(t) &= \frac{1}{2}\left[1 - \cos\left(2\pi\frac{t}{T_f}\right)\right] && t \in [0, T_f/2) \\ &= \cos\left(2\pi\frac{t - T_f/2}{T_f}\right) && t \in [T_f/2, n_c T_f) \\ &= \frac{1}{2}\left[1 - \cos\left(2\pi\frac{t - n_c T_f}{T_f}\right)\right] - 1 && t \in [n_c T_f, t_d] \\ &= 0 && t \in (t_d, \infty) \end{aligned} \tag{A3}$$

A typical waveform and its Fourier transform are shown in Fig. 2.7. The Fourier transform shows a dominant frequency, as expected; the bandwidth of the peak at this frequency varies inversely with t_d, but is largely independent of ω_f.

APPENDIX B: SPECIAL MATRICES FOR TWO-DIMENSIONAL ELASTIC PML

The matrices $\mathbf{B}^{\epsilon}$, $\mathbf{B}^{\varrho}$, $\hat{\mathbf{F}}^{\epsilon}$ and $\hat{\mathbf{F}}^{\varrho}$ used in Eq. (6.12) in Sec. 6.2.2 are defined as follows. Define

$$\mathbf{F}^{\imath} := \left[\frac{\mathbf{F}^{\mathrm{e}}}{\Delta t} + \mathbf{F}^{\mathrm{p}}\right]^{-1}, \quad \mathbf{F}^{\epsilon} := \mathbf{F}^{\mathrm{e}}\mathbf{F}^{\imath}, \quad \mathbf{F}^{\varrho} := \mathbf{F}^{\mathrm{p}}\mathbf{F}^{\imath} \tag{B1}$$

with $\mathbf{F}^{\mathrm{e}}$ and $\mathbf{F}^{\mathrm{p}}$ defined for two-dimensional problems as in Eq. (4.5b), but with c_s replacing C. Then $\mathbf{B}^{\epsilon}$ is defined in terms of nodal submatrices as

$$\mathbf{B}^{\epsilon}_I := \begin{bmatrix} F^{\epsilon}_{11}N^{\imath}_{I1} & F^{\epsilon}_{21}N^{\imath}_{I1} \\ F^{\epsilon}_{12}N^{\imath}_{I2} & F^{\epsilon}_{22}N^{\imath}_{I2} \\ F^{\epsilon}_{11}N^{\imath}_{I2} + F^{\epsilon}_{12}N^{\imath}_{I1} & F^{\epsilon}_{21}N^{\imath}_{I2} + F^{\epsilon}_{22}N^{\imath}_{I1} \end{bmatrix} \tag{B2}$$

where

$$N^{\imath}_{Ii} := F^{\imath}_{ij}N_{I,j} \tag{B3}$$

The matrix $\mathbf{B}^{\varrho}$ is defined similarly, with $\mathbf{F}^{\varrho}$ replacing $\mathbf{F}^{\epsilon}$ throughout. Furthermore,

$$\hat{\mathbf{F}}^{\epsilon} := \begin{bmatrix} \left(F^{\epsilon}_{11}\right)^2 & \left(F^{\epsilon}_{21}\right)^2 & F^{\epsilon}_{11}F^{\epsilon}_{21} \\ \left(F^{\epsilon}_{12}\right)^2 & \left(F^{\epsilon}_{22}\right)^2 & F^{\epsilon}_{12}F^{\epsilon}_{22} \\ 2F^{\epsilon}_{11}F^{\epsilon}_{12} & 2F^{\epsilon}_{21}F^{\epsilon}_{22} & F^{\epsilon}_{11}F^{\epsilon}_{22} + F^{\epsilon}_{12}F^{\epsilon}_{21} \end{bmatrix} \tag{B4}$$

and $\hat{\mathbf{F}}^{\varrho}$ is defined similarly, with $\mathbf{F}^{\varrho}$ replacing $\mathbf{F}^{\epsilon}$ throughout.

APPENDIX C: SPECIAL MATRICES FOR THREE-DIMENSIONAL ELASTIC PML

The matrices $\mathbf{B}^{\epsilon}$, $\mathbf{B}^{\varrho}$, $\hat{\mathbf{F}}^{\epsilon}$ and $\hat{\mathbf{F}}^{\varrho}$ for three-dimensional problems as used in Eq. (6.12) in Sec. 6.2.2 are defined as follows. Consider the matrices $\mathbf{F}^{\imath}$, $\mathbf{F}^{\epsilon}$, $\mathbf{F}^{\varrho}$ as defined in Eq. (B1), but with $\mathbf{F}^{\mathrm{e}}$ and $\mathbf{F}^{\mathrm{p}}$ defined for three-dimensional problems as in Eq. (4.23) with c_s replacing C throughout. Then $\mathbf{B}^{\epsilon}$ is defined in terms of nodal submatrices as

$$\mathbf{B}_I^{\epsilon} := \begin{bmatrix} F_{11}^{\epsilon} N_{I1}^{\imath} & F_{21}^{\epsilon} N_{I1}^{\imath} & F_{31}^{\epsilon} N_{I1}^{\imath} \\ F_{12}^{\epsilon} N_{I2}^{\imath} & F_{22}^{\epsilon} N_{I2}^{\imath} & F_{32}^{\epsilon} N_{I2}^{\imath} \\ F_{13}^{\epsilon} N_{I3}^{\imath} & F_{23}^{\epsilon} N_{I3}^{\imath} & F_{33}^{\epsilon} N_{I3}^{\imath} \\ F_{11}^{\epsilon} N_{I2}^{\imath} + F_{12}^{\epsilon} N_{I1}^{\imath} & F_{21}^{\epsilon} N_{I2}^{\imath} + F_{22}^{\epsilon} N_{I1}^{\imath} & F_{31}^{\epsilon} N_{I2}^{\imath} + F_{32}^{\epsilon} N_{I1}^{\imath} \\ F_{11}^{\epsilon} N_{I3}^{\imath} + F_{13}^{\epsilon} N_{I1}^{\imath} & F_{21}^{\epsilon} N_{I3}^{\imath} + F_{23}^{\epsilon} N_{I1}^{\imath} & F_{31}^{\epsilon} N_{I3}^{\imath} + F_{33}^{\epsilon} N_{I1}^{\imath} \\ F_{12}^{\epsilon} N_{I3}^{\imath} + F_{13}^{\epsilon} N_{I2}^{\imath} & F_{22}^{\epsilon} N_{I3}^{\imath} + F_{23}^{\epsilon} N_{I2}^{\imath} & F_{32}^{\epsilon} N_{I3}^{\imath} + F_{33}^{\epsilon} N_{I2}^{\imath} \end{bmatrix} \tag{C1}$$

where $N_{Ii}^{\imath}$ is given by Eq. (B3). The matrix $\mathbf{B}^{\varrho}$ is defined similarly, with $\mathbf{F}^{\varrho}$ replacing $\mathbf{F}^{\epsilon}$ throughout. Furthermore,

$$\hat{\mathbf{F}}^{\epsilon} := \begin{bmatrix} \left(F_{11}^{\epsilon}\right)^2 & \left(F_{21}^{\epsilon}\right)^2 & \left(F_{31}^{\epsilon}\right)^2 & F_{11}^{\epsilon} F_{21}^{\epsilon} & F_{11}^{\epsilon} F_{31}^{\epsilon} & F_{21}^{\epsilon} F_{31}^{\epsilon} \\ \left(F_{12}^{\epsilon}\right)^2 & \left(F_{22}^{\epsilon}\right)^2 & \left(F_{32}^{\epsilon}\right)^2 & F_{12}^{\epsilon} F_{22}^{\epsilon} & F_{12}^{\epsilon} F_{32}^{\epsilon} & F_{22}^{\epsilon} F_{32}^{\epsilon} \\ \left(F_{13}^{\epsilon}\right)^2 & \left(F_{23}^{\epsilon}\right)^2 & \left(F_{33}^{\epsilon}\right)^2 & F_{13}^{\epsilon} F_{23}^{\epsilon} & F_{13}^{\epsilon} F_{33}^{\epsilon} & F_{23}^{\epsilon} F_{33}^{\epsilon} \\ 2F_{11}^{\epsilon} F_{12}^{\epsilon} & 2F_{21}^{\epsilon} F_{22}^{\epsilon} & 2F_{31}^{\epsilon} F_{32}^{\epsilon} & F_{11}^{\epsilon} F_{22}^{\epsilon} + F_{21}^{\epsilon} F_{12}^{\epsilon} & F_{11}^{\epsilon} F_{32}^{\epsilon} + F_{31}^{\epsilon} F_{12}^{\epsilon} & F_{21}^{\epsilon} F_{32}^{\epsilon} + F_{31}^{\epsilon} F_{22}^{\epsilon} \\ 2F_{11}^{\epsilon} F_{13}^{\epsilon} & 2F_{21}^{\epsilon} F_{23}^{\epsilon} & 2F_{31}^{\epsilon} F_{33}^{\epsilon} & F_{11}^{\epsilon} F_{23}^{\epsilon} + F_{21}^{\epsilon} F_{13}^{\epsilon} & F_{11}^{\epsilon} F_{33}^{\epsilon} + F_{31}^{\epsilon} F_{13}^{\epsilon} & F_{21}^{\epsilon} F_{33}^{\epsilon} + F_{31}^{\epsilon} F_{23}^{\epsilon} \\ 2F_{12}^{\epsilon} F_{13}^{\epsilon} & 2F_{22}^{\epsilon} F_{23}^{\epsilon} & 2F_{32}^{\epsilon} F_{33}^{\epsilon} & F_{12}^{\epsilon} F_{23}^{\epsilon} + F_{22}^{\epsilon} F_{13}^{\epsilon} & F_{12}^{\epsilon} F_{33}^{\epsilon} + F_{32}^{\epsilon} F_{13}^{\epsilon} & F_{22}^{\epsilon} F_{33}^{\epsilon} + F_{32}^{\epsilon} F_{23}^{\epsilon} \end{bmatrix} \tag{C2}$$

and $\hat{\mathbf{F}}^{\varrho}$ is defined similarly, with $\mathbf{F}^{\varrho}$ replacing $\mathbf{F}^{\epsilon}$ throughout.